Materials Today Chemistry 26 (2022) 101220

Contents lists available at ScienceDirect

Materials Today Chemistry

journal homepage: www.journals.elsevier.com/materials-today-chemistry/

Multicomponent magnetic nanoparticle engineering: the role of structure-property relationship in advanced applications

A.G. Díez [a], M. Rincón-Iglesias [a], S. Lanceros-Méndez [a, b], J. Reguera [a, **], E. Lizundia [a, c, *]

[a] BCMaterials, Basque Center for Materials, Applications and Nanostructures, UPV/EHU Science Park, 48940 Leioa, Spain
[b] IKERBASQUE, Basque Foundation for Science, 48013 Bilbao, Spain
[c] Life Cycle Thinking Group, Department of Graphic Design and Engineering Projects, University of the Basque Country (UPV/EHU), Plaza Ingeniero Torres Quevedo 1, 48013 Bilbao, Biscay, Spain

ARTICLE INFO

Article history:
Received 13 May 2022
Received in revised form
20 September 2022
Accepted 22 September 2022
Available online 22 October 2022

Keywords:
Multicomponent magnetic nanoparticles
Multifunctional materials
Nanomedicine
Sensing
Catalysis
Life cycle assessment

ABSTRACT

Combining magnetic nanomaterials with materials of other classes can produce multicomponent nanoparticles with an entire ensemble of new structures and unique, enhanced, synergetic, and/or complementary functionalities. Here we discuss the most recent developments in the synthesis of multicomponent magnetic nanoparticles, describe the resulting structures and their novel properties, and explore their application in a variety of fields, including multimodal imaging, nanomedicine, sensing, surface-enhanced Raman scattering, and heterogeneous catalysis. The current synthetic methods (usually bottom-up approaches) of multicomponent nanoparticles can produce a number of tailored morphologies (core@shell, yolk-shell, core-satellite, Janus, nanochains, anisotropic, etc.), making them invaluable for applications in biology, medicine, chemistry, physics, and engineering. But like any new technology, their synthesis methods need to be optimized to be simple, scalable, and as environmentally friendly as possible before they can be widely adopted. In particular, the use of life cycle assessment (LCA) to guide future works toward environmental sustainability is highlighted. Overall, this review not only presents a critical and timely summary of the state-of-the-art of this burgeoning field in both fundamental and applied nanotechnology, but also addresses the challenges associated with understanding the particular structure-property relationships of multicomponent magnetic nanoparticles.

1. Introduction

In the past years, we have witnessed a burst in the development of novel nanomaterials with unique properties and the generation of unprecedented progress in material science. Magnetic nanoparticles (MNPs), among the different nanomaterials, are the ones that have more rapidly spread to technological and biological areas becoming the main enablers in different technologies. Their nanometric size, biocompatibility, and response to magnetic fields and field gradients have substantially contributed to the development of areas such as magnetic data storage, catalysis, sensing, environmental remediation, medical imaging, or pharmacology among others. Together with this development, the second generation of MNPs, which incorporate the combination of several materials in a single nanoparticle (NP), has appeared. The inclusion of properties coming from those materials, such as fluorescence, plasmonic response, or catalytic activities, has facilitated their applicability and opened new opportunities for more fundamental research as well as the appearance of novel applications.

Because of the nanometric size, NP properties are altered from their bulk material and become size-dependent. In particular, the behavior of MNPs can strongly vary by tuning their sizes in this relatively small range. For example, below ~30 nm ferromagnetic and ferrimagnetic NPs can become single-magnetic-domain to exhibit a superparamagnetic behavior at temperatures above their blocking temperature. Superparamagnetic behavior facilitates the colloidal dispersion and handling of the NPs since they do not magnetically interact with each other, but respond to an applied magnetic field, and when the external field ceases can be easily dispersed again [1,2]. Furthermore, the effect of size on magnetic properties such as coercivity and saturation magnetization has also been reported [3]. An increase in saturation magnetization and

* Corresponding author.
** Corresponding author.
E-mail addresses: javier.reguera@bcmaterials.net (J. Reguera), erlantz.liizundia@ehu.eus (E. Lizundia).

https://doi.org/10.1016/j.mtchem.2022.101220

coercivity with an increase in particle size has been observed for small NPs up to a threshold size, depending on the material, where they become size-independent [4].

Apart from the nature of the material and size, the shape anisotropy of the NP also affects these parameters, which have a direct impact on their performance. Thus, exploring different morphologies of nanomaterials is necessary to fully understand the possible advantages and disadvantages that each one of them possesses with respect to specific applications. The morphological structure-properties relationship, as well as the selection of synthetic methods in terms of simplicity, uniformity, scalability, and surface chemical properties, will provide the bases for the synthesis of more complex multicomponent magnetic nanoparticles (MMNPs) [5].

Chemically, the materials that provide the magnetic properties to the NPs are iron, cobalt, or nickel, their oxides, and some other elements combining several metals, such as materials based on copper, zinc, manganese, strontium, and barium. Among these elements, in the last decade, superparamagnetic iron oxide NPs (SPIONs), and in particular, magnetite (Fe_3O_4), maghemite (γ-Fe_2O_3), and metallic substituted ferrites (MFe_2O_4 (M = Co, Cu, Ni, Mn, Mg, etc.) have attracted almost completely the attention due to their biocompatibility, chemical stability, low cost, and unique magnetic properties [6]. Among all morphologies, spherical NPs have been the most extensively explored and the most common applications of MNPs (magnetic resonance imaging [MRI], hyperthermia, or tissue regeneration) have traditionally relied on that geometry [7–9]. Moreover, in MMNP systems, the magnetic properties of the NPs can be tuned by their composition, affecting the saturation magnetization and the coercivity of the resulting multicomponent systems [5]. Different models of nucleation and growth are beyond the scope of this review but can be explored elsewhere [10].

As the properties of MMNPs are strongly dependent on their dimension, composition, size, and structures, extensive efforts have been made to achieve fine control over these parameters. Methods such as co-precipitation, microemulsion, sol-gel, and hydrothermal/solvothermal methods have all been employed to synthesize NPs with magnetic properties. Overall, organic phase synthesis of MNPs possesses several advantages over conventional hydrolytic processes and gives a much tighter control over the NPs uniformity and structure [11]. Also, due to the large surface area, surface energy, and magnetic dipolar interactions, magnetic nanomaterials may tend to agglomerate and should be stabilized by a layer of organic or inorganic material. Further, the presence of that stabilizing layer can also aid in providing multifunctionality to the NPs. Hence, MNPs have been coated with, for example, biological molecules (for biomedicine-related applications) such as gluconic acid, lactobionic acid, folic acid, glycans, or specific antibodies, allowing the particles to bind to certain molecules, surfaces, or biological entities. Polymers, either natural or synthetic, are also commonly used to coat the NPs and can be achieved during the synthesis process of the NPs or after it. Dextran, chitosan, alginate, polyethylene glycol (PEG), polyacrylic acid (PAA), polyvinyl alcohol (PVA), or polyamidoamine, among others, have been used to produce that surface modification [12]. Not only organic components but also inorganic ones (such as silica and gold), have been used to coat the magnetic core, often further functionalized with organic molecules, and often providing biocompatibility, protection from corrosion, and other interesting characteristics (like surface plasmon resonance (SPR) in gold, for example).

Closely related to the coating process, the formation of multicomponent nanomaterials is a key factor in order to achieve the desired multifunctionality. In this review, multiple morphologies (core@shell, yolk-shell, core-satellite, Janus, or anisotropic) and their applications will be presented. In the area of imaging, for instance, gold and iron oxides are often used together for multimodal imaging techniques [13]. Other morphologies, like yolk-shell for example, can add multifunctionality to conventional drug delivery systems since the void space between yolk and shell can be loaded with the desired drug and delivered to the target area by means of magnetic fields [14]. In sum, the morphology does not only affect the properties of the nanostructures but is also a key factor in the specific multifunctional response to be achieved.

Understanding the inter-dependent relationship existing among synthesis, structure, properties, and performance/application is one of the essential goals in materials science [15–17]. Structure-property relationships have been applied to select materials for specific applications. Accordingly, in this review, we provide robust examples of the existing structure-property relationships in MMNPs to support proper selection and design for subsequent biomedical, sensing, or catalytic applications. For example, an adequate understanding of the structure-properties relationship in MMNPs can provide routes for improving their catalytic activity by tuning the electronic and morphological configuration [18]. We first focus on the representative synthetic strategies that allow controlling the chemistry and morphology of MNPs as a crucial step in the design and synthesis of more complex MMNPs. Then, the possible coating strategies as well as the different achievable morphologies of MMNPs are shown together with the description of some of the properties associated with those structures. The fourth part is devoted to applications where MMNPs have shown outstanding potential. After that, considerations regarding the environmental impact and circular economy implications are presented, as these are becoming a cause of increasing concern. Finally, future trends in MMNPs engineering and applications are briefly addressed.

2. Nanoparticle chemistry and morphology

Chemical, physical, and biological methods have been reported for synthesizing MNPs. Among them, chemical methods (also called wet-chemical or bottom-up methods) are the most employed due to their simplicity, tractability, scalability, and efficiency. Besides, the size, shape, and composition of NPs can be well controlled, obtaining high yields with inexpensive materials. On the contrary, physical methods do not allow easy control of the uniformity and use expensive equipment such as deposition of gas-phase or electron beam lithography, as an advantage, it does not require the use of hazardous chemicals. Finally, biological methods rely on magnetotactic bacteria for their synthesis. They provide, in general, highly reproducible NPs, but their synthesis is laborious and time-consuming [19]. Accordingly, chemically synthesized MNPs are much more widespread, especially those based on iron oxides, and multicomponent NPs are mainly based on them.

The synthesis of MMNPs involves, in general, many steps that depend on the type of used materials. The synthesis of noble metal NPs (Au, Ag, Cu), for instance, is produced by the reduction of salts and is generally well documented. In silica NPs, the Stöber method is the preferential synthesis route, while the synthesis of semiconductor metal oxide NPs follows similar methods to MNPs. Although some examples are given in Section 3, the full description of all synthesis methods is beyond the scope of the current review. Here, the most used wet-chemical methods for synthesizing MNPs based on iron oxides are described as the bases of the MMNPs. A summary of those methods is shown in Table 1.

2.1. Co-precipitation

Co-precipitation is the most common method, along with thermal decomposition, for the synthesis of MNPs, and it is used

Table 1
Summary of synthetic methods of magnetic nanoparticles.

	Synthetic method				
	Co-precipitation	Microemulsion	Thermal decomposition	Sol-gel	Solvothermal/Hydrothermal
Synthetic conditions	Easy to prepare in alkaline solutions, inert atmosphere	Co-precipitation inside a reverse micelle	High temperature in organic media	Easy to prepare, starts in ambient conditions, but an annealing is needed	Easy to prepare, starts in ambient conditions, but an annealing is needed
Reaction T (°C)	25 to 90	25	100 to 320	>1000	130 to 250
Solvent	Water	Water in oil	Organic solvents	Organic solvents in presence of capping agents	Organic/water
Main reagents	Inorganic salts of Fe^{+3} and M^{+2} (M = Fe, Mn, Co, Ni, Zn)	Inorganic salts of Fe^{+3} and M^{+2} (M= Fe, Mn, Co, Ni, Zn) and surfactants	Organometallic compounds ($Fe(CO)_5$, $Fe(acac)_3$, etc.)	Metal alkoxides (RO^-) (where R = CH_3, C_2H_5, C_3H_7) or hydrated inorganic salts	Organometallic compounds/ inorganic salts
Uniformity and shape control	Low uniformity. Nanorods, nanowhiskers, nanowires (using shaping ligands)	Narrow size distribution. Few 1D MNPs (rods, wires, tubes)	Very narrow size distribution. Nanocubes, nanooctopods.	Narrow size distribution. Nanowires, nanotubes	Very narrow size distribution Nanorods, nanotubes, nanoflowers, nanocubes
Scalabilty	Easy	Difficult	Easy	Difficult	Affordable
Reference	[36,38,39]	[44,45]	[52,55]	[56,62,68,69]	[70,78]

both at industrial and laboratory scales. This method consists of precipitating aqueous solutions of Fe^{2+} and Fe^{3+} ions with alkaline solutions in an inert atmosphere at room or higher temperatures. NaOH, $N(CH_3)_4OH$, and NH_4OH are the typical bases used during co-precipitation [2]. Usually, surfactants, polymers, or other organic species are added, which act as capping ligands to achieve the desired size and enhance the dispersion of particles due to steric impediments between them. Magnetite and substituted ferrites reaction steps are shown in Eq. (1) [20,21], where M = Fe, Mn, Co, Ni, Zn, etc., while maghemite is a product of the oxidation of magnetite [22]. During the synthesis process of magnetite, the ratio of 1:2 in Fe^{2+}:Fe^{3+} is kept to avoid the formation of other magnetic structures such as goethite or maghemite. Thus, the reaction temperature, the concentration of precursors, types of used salts, ionic strength of the media, and pH values are the key parameters that need to be optimized to control the size and shape of the formed MNPs [21,22]:

$$M^{2+} + 2Fe^{3+} + 8OH^- \rightarrow M(OH)_2 + 2Fe(OH)_3(s) \rightarrow MFe_2O_4(s) + 4H_2O \quad (1)$$

For the sake of comprehension, the reaction is explained using magnetite (M = Fe) as a model. First, the precipitation of ferric and ferrous hydroxides takes place. In a slower reaction, ferric hydroxide decomposes to intermediate specie, FeOOH. Finally, a ferrous hydroxide and FeOOH complex is formed, where a condensation reaction results in Fe_3O_4. The whole reaction takes place in 10–30 min, depending on the parameters selected for the reaction, which can be carried on at room temperature (25 °C). The most used precursors for magnetite NPs are $FeCl_2$ and $FeCl_3$; however, other anions, such as sulfates, nitrates, or perchlorates, are also used and directly influence the size of the particles. Overall, NP size decreases with the ionic strength of the solution. Further, an increase in anion size leads to higher diffusion resistance, slowing down the growth of the NPs [23], while smaller cations from the added basis: Na^+, NH_4^+, $N(CH_3)_4^+$, perform a better screening effect, leading to smaller size NPs [24].

Typically, the formation of MMNPs requires non-aggregated monodisperse particles to favor their subsequent surface modification. In this sense, the co-precipitation method is not the best approach as it is challenging to control the size and size distributions of MNPs, principally for particles below 20 nm. However, obtaining NPs with these characteristics is possible by carefully adjusting the pH of the solutions or adding capping agents [25]. Regarding the effect of the pH, the synthesis mainly occurs under alkali conditions. At stable high pH values (from 9 to 12), the negative charge of MNPs increases, and thus the strong attraction of cations yields smaller NP sizes in the range of 10–20 nm [20,26]. However, traditional synthesis processes start in acidic pH, and a base is added during the reaction. Gnanaprakash et al. studied the effect of the initial pH before alkali addition. When the starting pH was below 5, the obtained product was 100% magnetite, where the size increased with the initial pH values from 6.47 to 9.94 nm. However, above pH = 5, magnetite showed goethite impurities [27].

During the synthesis of spinel structures (magnetite and substituted ferrites), a reaction temperature of 95 °C, instead of room temperature, results in increased mean size, crystal size, and homogeneity of the crystals as a result of the acceleration of the chemical reactions. It is not clear in the literature if higher temperatures enhance the formation of other crystalline structures, such as goethite, hematite, or maghemite. Nevertheless, it is established that at a temperature above 60-70 °C, the particles' coercive field (H_c) and remanent magnetization (M_r) increase. This effect can be attributed to random pinning of the magnetic domains at the interface. Meanwhile, saturation magnetization (M_s) decreases due to the substitution of M^{2+} ions to Fe^{3+} in the octahedral sites, where the magnetic moment of Fe^{2+} is smaller [28–30].

The use of surfactants, such as sodium dodecyl sulfate (SDS), is a general strategy used in numerous synthesis methods to prevent the agglomeration of NPs, delivering lower hydrodynamic diameters [31]. Furthermore, soluble acids in aqueous media (citric, oxalic, lauric, and stearic acids) that can be chelating agents have also been used as capping agents, serving as an electrostatic stabilization of magnetite in water and narrowing the size distribution, which is a common handicap of this method [32,33]. Similarly, the coating of MNPs with polymers such as PVA can also be used to obtain good stabilization [34]. These kinds of organic molecules/polymers have been used, acting as shape-directing ligands or templates, for the synthesis of elongated NPs, such as nanorods (NRs), nanotubes, and nanowhiskers [35]. They can enhance the anisotropic growth of MNPs by modifying the surface energy by chelation with surface metal ions of specific planes and thus change the reactivity of these planes [36]. These effects can lead to the formation of rod-shaped MNPs of tunable aspect ratio by varying the reaction time [36,37]. Moreover, the application of an external

magnetic field during the reaction has been used to produce more crystalline rod-shaped magnetite NPs, with larger lengths under higher magnetic fields, while keeping the width intact [38]. However, similar experiments set at 90 °C produced sphere chain-like structures, which exhibit uniaxial magnetic shape anisotropy like NRs [39].

This method constitutes a simple route to synthesize SPIONs and substituted ferrites, being the main drawback that irregular-shaped and aggregated particles are usually obtained. This effect, together with their higher degree of aggregation, makes the combination of individual components in a single multicomponent NP a more challenging process. In this sense, the NPs obtained by co-precipitation, with the use of an external layer, organic, or inorganic, is the best method to form MMNPs.

2.2. Microemulsion method

A microemulsion is a thermodynamically stable isotropic dispersion of two immiscible water and oil phases in the presence of a surfactant that helps the formation of micelles with nanosized domains of one liquid in the other. The synthesis method of NPs is a co-precipitation inside a reverse micelle, *i.e.* water in oil, where the surfactant molecules form a monolayer at the interface providing a confinement effect that limits particle nucleation, growth, and agglomeration [40]. The preparation procedure of iron oxide NPs (IONPs) in microemulsion consists of mixing a microemulsion carrying iron salts with another emulsion of precipitating agents. The reactant exchange is achieved through diffusion when micro-droplets collide. The microemulsion method has several advantages, including thermodynamic stability and ease of preparation. Furthermore, compared with the traditional co-precipitation method, it allows the control of particle size, even at diameters lower than 20 nm, and morphology with narrow size distribution and good dispersion [41]. However, large-scale production of MNPs is limited as a consequence of the low temperatures and large quantity of oil necessary for a satisfactory synthesis [42,43].

Surfactants such as SDS, cetyltrimethylammonium bromide (CTAB), or dodecyltrimethylammonium bromide (DTAB) are the most used in this method. Lu et al. studied the effect of different surfactants obtaining nearly spherical Fe_3O_4 NPs of 10–20 nm average size for all the surfactants employed. The lattice perfection of Fe_3O_4 NPs synthesized decreased from cationic surfactant (DTAB) to non-ionic surfactant (polyoxyethylene(4)lauryl ether, named as Brij30) to anionic surfactant (SDS). SDS microemulsion showed better dispersion than other surfactants. In addition, it was established that the longer the hydrophobic tail, the longer the micellar lifetime that affects the process of reverse micelles motion-collision exchange and thus the growth rate of the NPs, decreasing the crystal defects [44].

This method has not been used extensively for anisotropic MNP fabrication due to its complexity during the control of the micelles' shape. However, by increasing the surfactant concentration, micelles can grow to less flexible rod-like micelles. Spontaneously, surfactant molecules assemble to form highly flexible locally cylindrical aggregates, making them ideal templates for synthesizing 1D NPs (rod, wires, tubes) due to the differences in the growth rates of different faces. For instance, Wang et al. obtained large aspect ratio (25:1) NRs of γ-Fe_2O_3 by injecting large concentrations of SDS and 4 h of reaction [45].

2.3. Thermal decomposition method

In this method, organometallic compounds such as M(acac) (acac = acetylacetonate), M(oleate), M(cup) (cup = N-nitrosophenylhydroxylamine), or M(carbonyl), where M is a metal element (usually transition metals), are thermally decomposed at high temperatures in the presence of surfactants and organic solvents, such as fatty acids, oleic acid (OA), oleylamine (OAm), and hexadecylamine (HDA). Unlike the co-precipitation method, thermal decomposition allows accurate control of the size, size distribution, and shape. However, the use of toxic and expensive precursors and organic solvents at high temperatures (a higher energy amount is required) makes this process less environmentally friendly [22]. The key factor of this method is the possibility of obtaining a higher separation of the nucleation and growth steps, following LaMer's theory of nucleation-growth [46]. In addition, two different routes to get monodispersed NPs are available: 'heating-up' and 'hot injection'. During heating-up, the solution with all the reagents premixed is progressively heated to a given temperature. In hot injection, the reagents are added into an already hot surfactant solution, leading to homogeneous fast nucleation. However, both processes follow the same formation mechanism, where intermediate species originated from precursors act as monomers for the iron oxide nanocrystals [47]. Thermal decomposition of zero-valent organometallic precursors, such as $Fe(CO)_5$, generate metal NPs that are subsequently oxidized by the media solvents or solvents derivatives produced when exposed to oxygen. In contrast, the decomposition of cationic metal centers, such as $Fe(acac)_3$, leads directly to metal oxides NPs, where the solvents' reductive effect, such as an excess of OAm, promotes the transformation of Fe^{3+} to Fe^{2+} [22,48,49].

Belaïd et al. studied the influence of temperature, reaction time, and surfactant amount during the synthesis of iron oxide nanocrystals via hot injection, employing $Fe(acac)_3$ as the precursor. They observed an increase in the size of NPs (from 4.3 to 8.0 nm, at 200 °C and 300 °C), crystallinity, and anisotropy energy with increasing temperature and time of reaction. Apart from avoiding the aggregation of NPs, the effect of the surfactants on the size and properties of the MNPs is not clear in the literature. While in medical applications, the use of surfactants and fatty acids is a drawback due to their hydrophobicity, they present a clear advantage during synthesis due to their versatility in modification with functional groups [50]. The main anisotropic NPs obtained with the thermal decomposition method are nanocubes and octopods. Different anisotropies were achieved by controlling the ligands' structure, the reaction's humidity, and the temperature rates. Nanocubes are obtained using various combinations of ligands (sodium oleate (NaOl)/OA) [51], OA/Oleylamine [52], OA/4-bisphenyl carboxylic acid [53], where the combination of ligands is what triggers the anisotropy [54]. Curiously, nano-octopods can be obtained by non-hydrolytic thermal decomposition $Fe(acac)_3$, submitting the mixture to reflux after the nucleation phase [55].

Although this method requires relatively high-temperature conditions, the reaction generally takes less than 2 h. The NPs formed by thermal decomposition have an excellent potential for developing MMNPs with tailored component sizes and shapes and narrow size distribution. In addition, the final synthesized NPs usually present an organic coating, making them colloidally stable in many organic solvents and reducing the oxidation and aggregation.

2.4. Sol-gel method

This process is based on the hydroxylation and condensation of molecular precursors in solution, creating a 'sol' of nanometric particles. Additional condensation and inorganic polymerization produce a three-dimensional metal oxide network denominated as a wet gel. The reaction is carried out at room temperature, and additional heat treatments are necessary to achieve the final crystalline state [22,56]. Typically, the process entails various steps. The

first steps are forming a stable solution of the precursors, called the sol, followed by gelation by a polycondensation or polyesterification (Pechini method) reaction forming an oxide- or alcohol-bridged network (the gel). Then, the aging of the gel is produced by further polycondensation reactions, and the gel is transformed into a solid mass. The gel network contracts and expulse the solvent from gel pores until the gel is dried, sometimes forming an aerogel (supercritical drying) or a xerogel (thermal evaporation of the solvent). Finally, dehydration of M−OH groups of the surface usually is achieved by calcination at temperatures up to 800 °C. This final annealing step leads to the aggregation of NPs [57].

Traditional precursors used in the sol-gel method are metal alkoxides (RO^-) that can be directly formed from a salt containing a metal and an alcohol (ROH) where R=CH_3, C_2H_5, or C_3H_7. However, in recent years, the most used precursors are hydrated inorganic salts, especially nitrates, for the development of substituted ferrites [58]. Moreover, the sol-gel method using citrate as stabilizer has been used to synthesize substituted ferrites. In their research, Ben Ali et al. utilized hydrated nitrate salts as precursors in the presence of citric acid to obtain spherical MNPs of cobalt and zinc substituted ferrites ($Co_{1-x}ZnxFe_2O_4$) of 11−28 nm in diameter. An increase in the saturation magnetization and a considerable decrease of the coercivity with higher amounts of zinc in the nanostructure was found [59].

In the same way, other natural substances, such as tragacanth gum [60] or Aloe vera, were used in more eco-friendly systems as stabilizers in the synthesis of substituted ferrites [61]. Accordingly, a combined method of chemical sol-gel and combustion methods (sol-gel auto-combustion) has been explored in the last years. It is based on the formation, of gels and subsequent combustion of an aqueous solution containing salts of the desired metals and reductant. Again, this route enables the use of natural organic substances, such as glucose, maltose, starch [62], honey (glucose and fructose mix) [63], urea [64], citric acid [65], cherry juice [66], as gelling, stabilizing, reducing, and capping agents. The use of non-natural surfactants is therefore avoided. In addition, this sol-gel auto-combustion synthesis path has been assisted by microwave, obtaining larger NPs with higher saturation magnetization than those obtained by conventional heating, in the case of $CoFe_2O_4$. However, the instantaneous high reaction temperature in microwave heating leads to the aggregation of NPs [67].

Nanotubes and nanowires have recently been synthesized by the templated sol-gel method. Ebrahimi et al. developed strontium hexaferrite ($SrFe_{12}O_{19}$) nanowires and nanotubes, introducing the sols in porous anodic aluminum oxide templates by employing spin coating, vacuum suction, and dip coating. Uniform nanowires and nanotubes of 60 nm diameter and lengths of several microns were successfully synthesized by the dip coating sol-gel process at 2000 rpm and calcination temperature of 650 °C [68]. Similarly, $CoFe_2O_4$ nanowires were synthesized by a sol-gel Pechini method in a porous silicon template, introducing the Si template in the sol solution, where the penetration of the sol in the template was assisted by ultrasound and then was sintered at 800 °C for 1 h [69].

2.5. Solvothermal/hydrothermal method

The solvothermal method, usually called hydrothermal method when water is used as the solvent, is one of the oldest 'Green chemistry' methods for the successful growth of crystals of many different materials. The synthesis at relatively low temperatures (130−250 °C) [22], lack of further annealing steps, closed system conditions (so no toxic gases are expulsed), recyclability of unused components, and the availability of using water as solvent make this efficient method a green process. In addition, the products are large amounts of high crystalline nanocrystals with well-controlled dimensions, which can be obtained at a low cost [70]. The use of microwaves as the heating system has drastically improved the usability of this synthesis method. The main advantages are the rapid and uniform heating rates (the whole process can take 30 min instead of several hours) and less risk of contamination of the NPs by heating elements and walls of the reactor. Furthermore, the precise control of reaction time makes the method more affordable for industrial-scale production [71].

The process can be briefly described as a heterogeneous chemical reaction in supercritical or near supercritical conditions, in the presence of a solvent above room temperature and high pressure [72]. The reactants and solvents used for hydro/solvothermal synthesis are iron-complex precursors in high-boiling point organic solvents and fatty acids or amines as stabilizing agents. Mainly, inorganic salts are used in aqueous media and organometallic compounds in organic solvents.

The control of the reaction time, temperature, surfactants, initial concentration of reagents, and solvents used are the key parameters to obtain the desired crystal structures and size of MNPs. In terms of NPs' sizes and shapes, this method is very versatile, allowing the fine-tuning of the particle dimensions in a wide range. In general, larger reaction times can lead to bigger NPs. Besides, at a certain point, the excess of time leads to inhomogeneous NP distributions and the formation of agglomerates. Similar behavior is observed with metal reactants, neither excessively low nor high concentration is favorable for the formation of uniform nanospheres [73]. Besides, higher concentrations of surfactants protect the particles more thoroughly immediately after their formation, generally leading to smaller sizes [74,75].

This method has been used to synthesize non-spherical NPs such as NRs, nanocubes, or nanoflowers. Sun et al. synthesized uniform magnetite NRs of 63 nm long and 6.5 nm in diameter by using $Fe(CO)_5$, OA, and HDA as raw materials and n-octanol as solvent at a 6 h reaction. During the solvothermal process, the decomposition of $Fe(CO)_5$ and the hydrolysis of iron oleate should coexist, where the hydrolysis of iron oleate and controlled releasing water promotes the formation of iron oxide NRs. The length of the NRs was tuned by changing the reaction time and the HDA amounts. Interestingly, FeO nanocubes were obtained for reaction times shorter than 80 min [76]. Recently, a green, simple, and efficient method has been reported for the development of pure Fe_3O_4 iron oxide nanocubes of 26 nm by solvothermal method assisted with β-amyrin (olean-12-en-3beta-ol, $C_{30}H_{50}O$), a pentacyclic triterpene commonly extracted from plants of the *Burseraceae* family. In the absence of this compound, the same size spherical NPs of magnetite were obtained [77]. Saeed et al. developed a series of PEG-coated Fe_3O_4 nanoflowers (Fe-NFs) in a diameter range of 70−250 nm. They used $FeCl_3 \cdot 6H_2O$, sodium acetate trihydrate ($NaAc \cdot 3H_2O$), and PEG dissolved in EG. The largest NPs were obtained with the lowest performed ratios between $FeCl_3 \cdot 6H_2O$ (40 mM) and $NaAc \cdot 3H_2O$ (330 mM). The growth of Fe_3O_4 spherical nuclei develops the flowerlike structure due to Ostwald ripening [78].

3. Multicomponent magnetic NPs: synthesis and structure-properties relationship

A step forward from synthesizing different morphologies in homocomponent NPs, the possibility of combining multiple materials into the same system allows functional combinations to be achieved [79]. Several heterostructures have been generated in order to take advantage of the benefits that each component possesses. For instance, porous NPs are very promising in the field of drug delivery since they allow the loading and controlled release of therapeutic agents (Fig. 1a) [80,81]. On the other hand, metal NPs may provide plasmonic or catalytic properties [82,83], which are

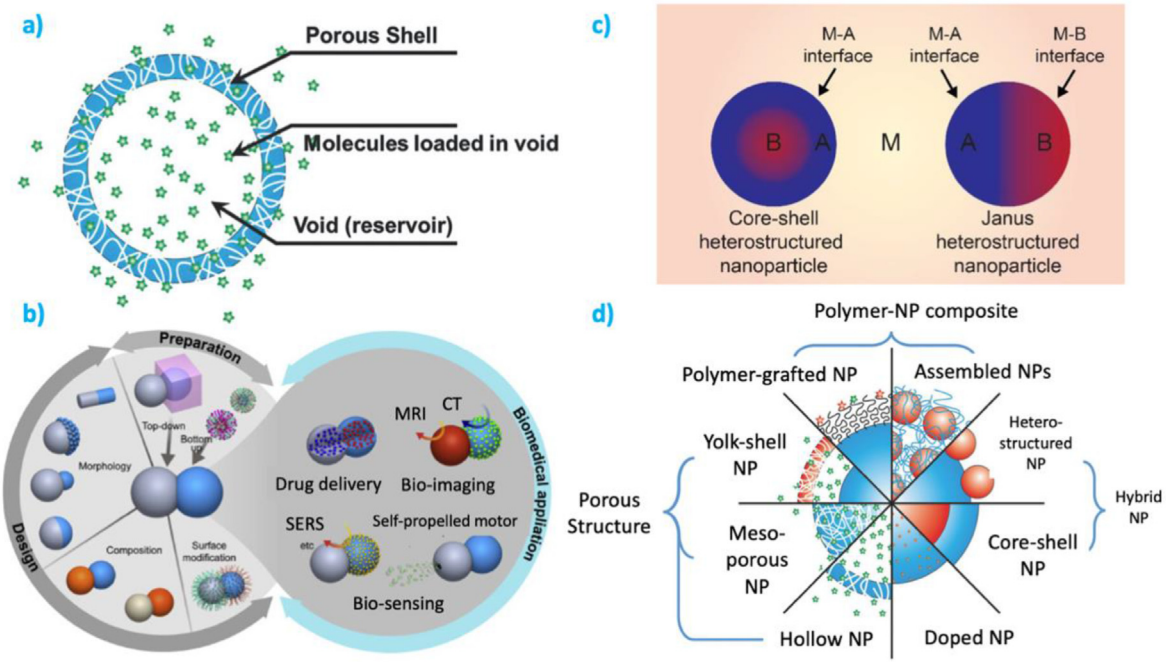

Fig. 1. (**a**) Schematic illustration of hollow NPs. Reproduced with permission of Wiley-Vch from the study by Kim et al. [79]. (**b**) Illustration of the design, preparation, and biomedical application of Janus NPs. Reproduced with permission of Elsevier from the study by Su et al. [89]. (**c**) Difference between core@shell and Janus NPs. Reproduced with permission of the American Chemical Society from the study by Ha et al. [90]. Copyright 2019 American Chemical Society. (**d**) Structural classes of multifunctional NPs. Reproduced with permission of Wiley-Vch from the study by Kim et al. [79]. NP, nanoparticle.

useful in the detection of diseases such as SARS-CoV-2 [84,85]. Together with the choice of material, the type of heterostructure morphology plays a crucial role in how those functions are expressed, *i.e.* in the structure-properties relationship, generating additional synergistic effects when the correct morphology is selected. For instance, Janus NPs (JNPs) (Fig. 1b) combine two different functional materials in single NP units [86]. They differ from core@shell NPs in the sense that both active surfaces are exposed to the surrounding medium at the same time exhibiting separated surface physico-chemical properties, but on the other hand, they lack the protecting layer of the core@shell structure (as seen in Fig. 1c) [87–89]. In Fig. 1d, a summary of some possible multicomponent nanostructures that give rise to multifunctionality is presented.

Heterostructured NPs encompass all morphologies in which different components are combined into a single NP. They are often categorized as either hetero-dimers, -trimers, or -oligomers. The number of morphologies is very high, and in many cases, there is a lack of consensus in the terminology describing them, leading to the use of very imaginative names. For instance, names, such as urchin-like [91], multipode [92], nanoflower [93], or nanostars [94], are often used for the description of the same type of morphologies [79]. In this part of the review, the structures are classified into a reduced number of categories. We will focus on the main configurations that have been employed to provide multifunctionality to the MNPs of different shapes, for which the synthesis methods have been explained in the previous section. The aim is to present a general overview of these structural classes, describing the methods and materials that can be used, which can include organic, inorganic, and biological coatings, and the properties associated with such structures.

3.1. Core@shell NPs

The core@shell structure can be defined as the class of nanomaterials that have distinct boundary materials completely covering the inner component, in a way that they can be separately identified [95]. This structure is one of the most widely used and synthesized structures and has found applicability in catalysis [96], imaging [13], or optical sensing [97]. The formation of the shell around the core can be achieved through different procedures. For instance, when the coating material is inorganic, the process can be carried out *via* adsorption of the coating elements from a precursor [98]. If the coating material is polymeric, then the covalent attachment of polymer shells to the surface of the cores can be achieved either by a 'grafting to' or 'grafting from' methods. The former involves the reaction of end-functionalized polymer molecules with complementary functional groups on the surface of the NPs, while the latter is a surface-initiated polymerization, with the functional initiators linked onto the NP surface to initiate the polymerization directly [99]. Moreover, particles with more than one shell can also be synthesized with consecutive graftings [100]. Several properties can arise from this type of structure. One of the main benefits is that the shell can protect the core structure from degradation and prevent aggregation. For example, magnetite (Fe_3O_4) is particularly sensitive to oxidation, and transforms to maghemite (γ-Fe_2O_3) in the presence of oxygen [101], causing loss of magnetism and dispersity. Thus, strategies for coating or protecting the magnetic component (such as the formation of shells) are quite important [102]. The use of core-shell structure also allows the enhancement of the magnetic properties by modifying the surface anisotropy [103] (see Section 4.1.2), the improvement of the microwave absorbance [93,104], or the tuning of the plasmonic

properties of metal nanoshells by varying the shell thickness (see Section 4.2.2).

Among others, gold is widely used as a coating material due to its plasmonic properties, its electrical conductivity, stability, and ease of modification with organic molecules (*via* thiol groups and amines). Core@shell MNPs have been coated with gold for applications in magnetic-field-enhanced photothermal therapy (PTT) [98]. In this case, spherical Fe_3O_4 NPs were synthesized via a high-temperature hydrolysis process and directly coated with gold by a single hydrothermal method. First, a Fe_3O_4 solution (8.6 mg/mL) was injected into 0.1 mol/L of $HAuCl_4.4H_2O$ solution and stirred for 3 h. After that, 0.8 mL of ammonium hydroxide was added to the system. Finally, the mixture was heated to 40 °C for 1 h. The transmission electron microscopy (TEM) images (Fig. 2a) showed uniform morphology and good dispersity, with the magnetic core surrounded by a layer of gold with a thickness of approximately 20 nm. Dynamic light scattering analysis gave a mean diameter of 100 nm and hysteresis curves showed a saturation magnetization of around 30 emu/g.

Another strategy that has been extensively utilized to grow nanoshells [105] combines the techniques of molecular self-assembly with the reduction chemistry of metal colloids. This method is based on functionalizing the surface of the core part with silanes, such as 3-Aminopropyltriethoxysilane (APTES) or 3-aminopropyltrimethoxysilane so that the amine groups extend outward of the surface of the core. When the coated structure is added to a solution containing gold NPs, they can covalently bond to the amine group of the organosilane. The next step is to form a nanoshell, using these coated particles as nucleation points. To achieve this, the chloroauric acid in a potassium carbonate solution is reduced by sodium borohydride or formaldehyde [106]. The thickness of the gold shell is related to the amount of precursor solution as well as the concentration of Au^{3+} ions in it. This method has also been used on Fe_2P NRs or cubes [106,107].

As mentioned above, polymers have been employed in order to produce coatings and stabilize the magnetic cores. A novel method to produce a polymeric coating around inorganic semiconductor nanoparticles, including ZnO, TiO_2, and Fe_3O_4 was reported. The method consists of continuous aerosol-photopolymerization, which allows the condensation of monomer vapor around the surface of the particles that is polymerized 'in-flight' using ultraviolet (UV) light radiation [99]. Fe_3O_4 NPs and butyl acrylate (BuA) were used. A bubbler at 50 °C was used to generate vapor of BuA, in a carrier gas at a flow rate of 0.5 L/min. The cooling to room temperature produced supersaturation, which in turn allowed the vapor to condense around the NPs. Then, the mixture of condensed vapor and NPs passed through a chamber irradiated with UV light. A summary of the process is shown in Fig. 2b. TEM investigations conclude that most NPs were appropriately coated, and no isolated particle was observed. Hence, this method demonstrated promising characteristics since it is fast and low-cost. Furthermore, it does not require surfactants, co-initiation, or surface modification of the NPs, which is a common feature among many grafting methods.

One issue that appears when implementing core@shell NPs in the biomedical context is that biocompatibility must be assured while also maintaining stability. A typical material that achieves good results in terms of improving the colloidal stability of the particles is silica, although the capping agents commonly employed with it present biocompatibility issues [109]. To palliate this, one possibility is to employ proteins such as capping agents since they are highly compatible biological materials [110]. For instance, Maboudi et al. reported the synthesis of multi-layered MNPs, coating iron oxide MNPs clusters with a thin silica shell (MS particles) and subsequently surrounding them with bovine serum albumin (BSA) [108]. The OA-coated magnetite NPs are synthesized by the co-precipitation method, starting from $FeCl_3 \bullet 6H_2O$ and $FeCl_2 \bullet 4H_2O$. Then, the IONP clusters/silica core/shell

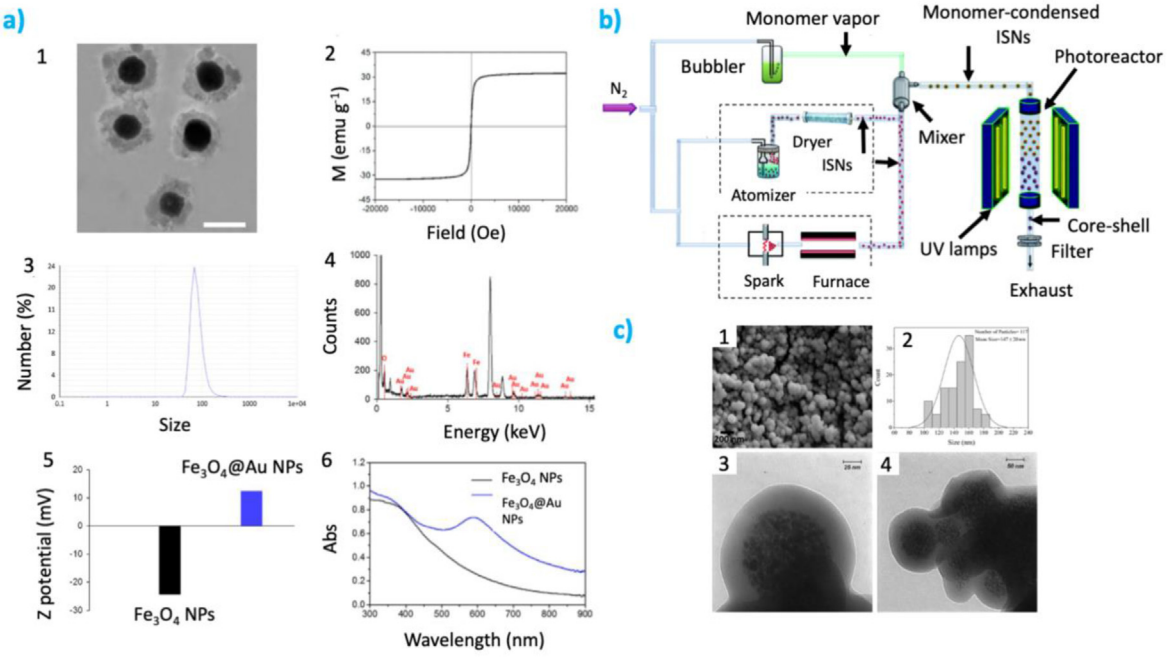

Fig. 2. (**a**) (1) TEM images (left, scale bar 100 nm), (2) magnetization curve, (3) DLS analysis, (4) energy dispersive X-Ray spectrum, (5) Z potential and 6) UV–Vis NIR extinction spectrum of Fe_3O_4@Au NPs. Reproduced with permission from MDPI from the study by Hu et al. [98]. (**b**) Schematic diagram of the continuous experimental setup for aerosol-based fabrication of core@shell materials. Reproduced with permission from The Royal Society of Chemistry from [99]. (**c**) (1) SEM image of MS particles, (2) their size distribution, (3) and (4) TEM images of magnetite and silica (MS particles). Reproduced with permission of Elsevier from the study by Maboudi et al. [108]. DLS, dynamic light scattering; NIR, near-infrared; SEM, scanning electron microscopy; TEM, transmission electron microscopy; UV, ultraviolet.

nanocomposites were produced *via* the hydrolysis-condensation of tetraethyl orthosilicate and finally surface-treated with aminosilane and coated with a BSA shell. SEM images (Fig. 2c) showed MS NPs with an average size of 147 ± 20 nm. With regard to the magnetic properties, the normalized saturation magnetization was 72.6 emu/g for the NPs, 82.4 emu/g for the MS particles, and 81.8 emu/g for the final particles with the BSA shell. The effect of clustering the NPs increases the magnetization, which in turn is slightly decreased due to the diamagnetic nature of the Si and BSA shells. Furthermore, cytoviability measurements confirmed that the addition of the BSA layer improved the cytotoxicity compared with the MS NPs alone.

3.2. Yolk-shell NPs

In contrast with the core@shell structure, yolk-shell nanoparticles (YSNPs) consist of a movable core inside the hollow shell of the same or different materials [111]. Much in the same way as core@shell NPs, YSNPs retain the functionalities of both the core and the shell components. However, since the core NP is located in a hollow cavity enclosed within an outer shell, it modifies the structure-properties relationship with respect to core-shell structures. In this case, the properties of the two materials tend to be more independent of the other components and behaving like the same homo-component substructures when they are alone. Therefore, properties such as magnetic or plasmonic can be better predicted in the formation of yolk-shell structures. Finally, the void space between the two components adds an additional property providing the capacity to load and carry molecules for sensing [112], catalysis [113], or therapeutic activity [114] in highly effective drug delivery systems [79].

The synthetic process slightly differs from the core@shell. Among the different strategies, selective etching methods based on the Kirkendall effect or the Ostwald ripening [115] can be mentioned. However, a sacrificial-template mediated approach is the most often chosen route to produce YSNPs [116]. In this case, a system with two shells is synthesized in which the intermediate material is later removed by selective etching or dissolution. Among those materials, SiO_2 is one of the most employed inorganic materials, while polymeric coatings are typically employed as sacrificial organic layers.

The space between yolk and shell presents unique opportunities concerning targeted drug delivery, having unique advantages (such as preferential tumor accumulation) and disadvantages (like the inability to convey high enough levels of drug concentrations in comparison with organic particles). To circumvent the obstacle of drug resistance, a yolk-shell Fe_3O_4@$MgSiO_3$ nanoplatform has been reported [14]. The goal of this nanoplatform was to specifically deliver and concentrate doxorubicin (DOX). Initially, Fe_3O_4@$MgSiO_3$ core@shell NPs were synthesized. The presence of this magnetic core allowed magnetic targeting to accumulate the nanocomposites on the tumor site. Afterward, a Fe_3O_4@$MgSiO_3$ yolk-shell structure was created by mixing the previous NPs with $MgCl_2$•$6H_2O$ and NH_4Cl, creating magnetic mesoporous nanocomposites (MMNs). The MMNs were functionalized with PEG and APTES (50 mL) in an N_2 atmosphere, resulting in MMNs-PEG/NH_2 nanocomposites. Finally, these nanocomposites were mixed with 50 mg of folic acid (FA, a promising candidate for tumor targeting) dissolved in 10 mL of dimethyl sulfoxide (DMSO). The synthesized MMNs-PEG/FA nanocomposites were loaded with DOX by immersion (Fig. 3a).

YSNPs have not only been used with biomedical purposes but also in other fields such as photocatalysis. The main advantage of the Y–S structure in catalysis is that the light that falls on the surface of the particles can be reflected several times in the inner cavity between yolk and shell so that much more light can be absorbed by the materials. Xiang et al. were able to synthesize $ZnFe_2O_4$@$ZnFe_2O_4$ MNPs with yolk-shell structure [117], following a self-templated solvothermal method, by dissolving in 10 mL of glycerol and 50 mL of isopropanol, 0.5 mM of $Fe(NO_3)_3$•$9H_2O$, and 0.25 mM of $Zn(NO_3)_2$•$6H_2O$. Then, this precursor needed to be annealed at 350 °C for 2 h. The catalytic performance was investigated on tetracycline, under irradiation with visible light. The mechanism for tetracycline degradation is shown in Fig. 3b. Also, changing the annealing rate to 1 °C/min produced solid $ZnFe_2O_4$ solid nanospheres, without the yolk-shell structure.

Finally, it is worth mentioning that the yolk-shell structure is not limited to spherical NPs. For instance, the fabrication of ellipsoidal silica yolk-shell magnetic structures has been reported [118]. α-Fe_2O_3 ellipsoids and resorcinol-formaldehyde resins were used as cores and sacrificial templates, respectively, and then, constructing the ellipsoidal hierarchical nanostructures composed of α-Fe_2O_3@SiO_2 as yolk-shells. Similarly, nanoscale magnetic stirring bars have also been successfully produced for applications in catalysis [119]. In the first place, α-Fe_2O_3 magnetic spindles were prepared and, with the assistance of tetraethyl orthosilicate, cetyltrimethylammonium bromide, and PVP, a mesoporous SiO_2 coating was formed outside. Calcination produced mSiO_2 shells, and the cores were reduced to Fe under a hydrogen atmosphere. Finally, Pd NPs were formed through in situ galvanic replacement reaction between the Fe core and Na_2PdCl_4. The final product could be used as catalysts for hydrogenation reactions of phenols, olefins, and other chemicals since Pd can dissolve 700 times the volume of hydrogen at room temperature.

3.3. Core-satellite NPs

In core-satellite nanostructures, a single core NP has several other satellite NPs (of a different element) attached to it. In general, heterogeneous nucleation and growth is the most popular approach to synthesizing this structure [79]. This method consists of overgrowing several phases at the surface of the seed (core) NP to form the heterostructure. Another approach is to use ligands to form covalent or physical attachments of preformed satellite particles to the core NP, in a similar way as the Oldenburg method discussed in Section 3.1. Several properties can be identified for this structure that differ from core-shell structures with continuous and complete shells. The space between satellites allows the solvent to access the surface of the inner core, which could decrease the protective properties but can be very convenient in applications such as heterogeneous catalysis (Section 4.4) or biomedical imaging (Section 4.1.4). Additionally, the gap formed between the satellites can generate electromagnetic hotspots when they are made of noble metals, which has been highly exploited in surface-enhanced Raman scattering (SERS) sensing (section 4.2.2).

Qiu et al., for instance, synthesized magnetic Fe_3O_4–Au NPs for SERS detection [120]. The Fe_3O_4 NPs were synthesized following a solvothermal approach, where 0.45 g of $FeCl_3$•$6H_2O$ was dissolved in 14 mL of ethylene glycol. After that, 1.2 g of NaAc and 0.3 g of PEG were added. After stirring for 30 min, the mixture was sealed in a Teflon-lined stainless-steel autoclave and heated to 200 °C and left to react for 8 h. In parallel, the Au NPs were synthesized from $HAuCl_4$, obtaining particles of around 20 nm size. Finally, the Fe_3O_4–Au NPs were prepared by adsorption of the Au NPs on the surface of the Fe_3O_4 NPs through electrostatic interaction (Fig. 3c). The synthesized nanostructures were further functionalized with Raman active molecules and antibodies for labeling.

More complex structures can also be fabricated, for example, if the basic core-satellite structure is further coated with another compound in order to form a core-satellite@shell structure. In this

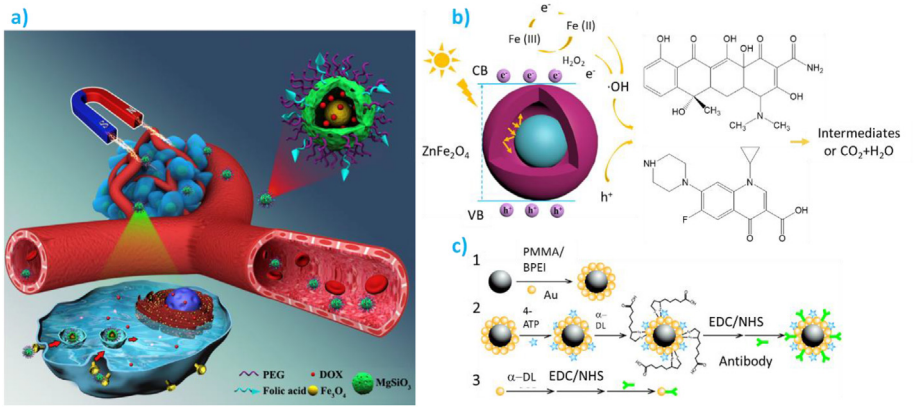

Fig. 3. (**a**) Schematic illustrating the DOX-loaded MMNs-PEG/FA with dual-targeting for overcoming the drug-resistant cancer by intravenous injection. Reproduced with permission of Elsevier from the study by Wang et al. [14]. (**b**) Photo-Fenton mechanism for TC degradation over the yolk-shell $ZnFe_2O_4$ sphere under visible light irradiation. Reproduced with permission of Elsevier from the study by Xiang et al. [117]. (**c**) Schematic illustration of the synthesis of Fe_3O_4–Au NPs. Reproduced with permission from The Royal Society of Chemistry from the study by Qiu et al. [120]. DOX, doxorubicin; FA, Fe_3O_4@SiO_2–Au; MMNs, magnetic mesoporous nanocomposites; PEG, polyethylene glycol.

sense, Fe_3O_4–Au@TiO_2 (FAT) structure has been reported, with applications in detection and photo-reduction of Cr(VI) [121]. First, Fe_3O_4@SiO_2–Au (FA) NPs were synthesized following a procedure by which Fe_3O_4 particles were wrapped first in a SiO_2 shell. These structures were decorated with the cationic polyelectrolyte poly(-diallyldimethylammonium chloride) that acts as a bridge for the connection between the Au NPs and the silicon oxide shell [122]. Then, the colloid TiO_2 NPs were synthesized by mixing 12.5 mL of tetrabutyl titanate with 4 mL of isopropyl alcohol, and shaken until a homogeneous solution appeared. After that, this mixture was added dropwise to a solution containing 150 mL of deionized water and 2 mL of HNO_3 with vigorous stirring at 70–80 °C. Finally, to coat the FA NPs with TiO_2, polyelectrolyte functioned FA-PSS (−) was prepared through a layer-by-layer method. 3 mL of this FA-PSS (−) were dispersed in 1–20 mL of TiO_2 colloids and shaken for 20 min, forming the FAT structures. The final nanocomposite had a 374 nm Fe_3O_4@SiO_2 core surrounded by 20 nm satellite Au NPs, with a 5 nm gap between the Au NPs. All this structure was coated by a 2 nm layer of TiO_2.

3.4. Janus NPs

JNPs, also called heterodimers, are defined as those that present two distinguishable and joined subunits with physicochemical differences [87]. They present two material surfaces that can be independently functionalized and generate a broken symmetry that imparts directionality. This unique property has been applied in very diverse applications, like the generation of catalytic nanomotors (also called nanojets or nanoswimmers) [123], or the creation of specific interactions with biological surfaces and interfaces [124]. This is the case, for instance, of cell membranes where JNPs have been proposed to transport drugs to the cell interiors through an engulfment process [125]. This broken symmetry has also been used to create nanoamphiphiles that can stabilize interfaces, like in the case of oil-water emulsions [126], or guide the self-assembly to obtain higher hierarchical supra-structures [127]. Together with these properties-structure relationships, these types of structures present easy access of the solvent to the two surfaces that, like in the case of core-satellites structures, can facilitate heterogeneous catalysis or enhance the contrast in multimodal imaging techniques (section 4.2 and 4.1.1).

One of the Janus MMNPs that has attracted more interest is the one formed by magnetic materials such as magnetite with gold to combine magnetic with plasmonic properties. These types of JNPs have been successfully synthesized through a thermal decomposition method [128]. In the first place, 4, 7, and 10 nm Au NPs were synthesized by OAm reduction of $HAuCl_4$, which were used as the starting point for a seed-mediated growth method. The Au NPs were added to a solution containing 1 mM of (HDA)•HCl with 12 mL of 1-octadecene (ODE) and 1 mL of OAm at 120 °C. After that, the solution was heated to 180 °C and 2.0 mM of $Fe(CO)_5$ was added to form the 4–15 nm Au–Fe heterodimer NPs. The same reaction conditions, with varying masses of Au NPs of different sized, gave distinct heterodimers, namely, 7–13 nm Au–Fe and 10–11 nm Au–Fe. At last, to form the Au–Fe_3O_4 NPs, a dispersion of the previous heterodimer Au–Fe NPs was mixed and magnetically stirred with 20 mL ODE and 1 mL OAm, then heated to 160 °C for 15 min to oxidize the Fe into Fe_3O_4. TEM and high-resolution TEM images of the particles confirmed the formation of heterodimers. The surface oxidation of Fe forms a Fe_3O_4 shell that prevents further oxidation of the Fe in the core. UV–Vis spectra showed a localized SPR absorption peak at 520 nm for the Au NPs (which is independent of the particle size), but shifts to 538 nm when the Au NPs were coupled to Fe_3O_4 in the heterodimers due to the pull of Au electrons by the attached iron oxide. Fig. 4a shows the TEM images of the Au–Fe_3O_4 heterodimers.

In a similar way, Au–Fe_2C JNPs can be synthesized via a three-step process: preparation of Au seeds, the formation of Au–Fe heterostructures, and the carburization process of Au–Fe_2C Janus NPs [129]. In first step, 1 mL of 9 nm Au NPs, 8 mg of NH_4Br, 15 mL of ODE, and 100 mL of OAm were mixed and stirred in a 10 mL four-neck flask under standard gas (5% H_2 in Ar) atmosphere. Then, the system was heated to 100 °C and degassed for 2 h. After that, the temperature was raised to 180 °C, and 100 mL of $Fe(CO)_5$ was injected into the solution. The carbonization process was carried out by injecting the Au–Fe heterostructures in hexane via a syringe, degassed at 120 °C for 30 min, and finally heated to 300 °C for another 30 min. With this process, the Au–Fe_2C JNPs were obtained (more details can be seen in Fig. 4b). JNPs have also been synthesized with different morphologies, like nanostars [88], or they have been modified to give them interesting features, such as self-propulsion [130].

Dumbbell-like NPs, named after their characteristic shape, can also be regarded as a kind of JNPs with two lobes of similar diameter (as opposed to snowman-like NPs that present very different sizes between the two materials). Gold-iron dumbbell-like NPs have been obtained by the thermal decomposition of iron-oleate complex ($Fe(OL)_3$) in the presence of Au seeds at 310 °C [131]. In

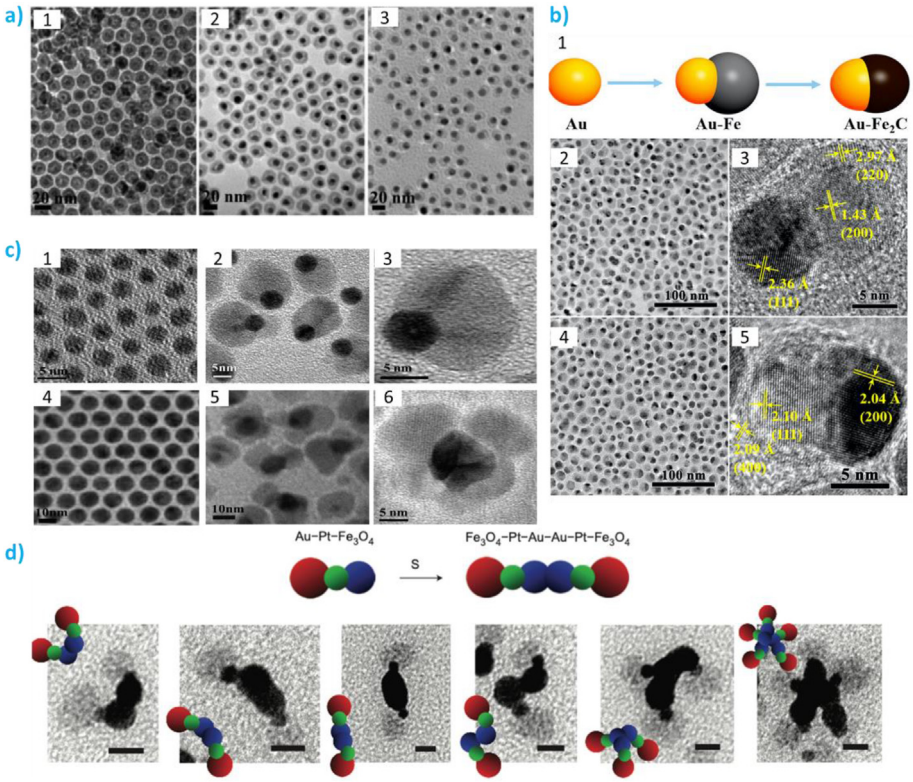

Fig. 4. (**a**) TEM images of the Au−Fe_3O_4 heterodimer NPs with different lobe ratios (1) 4−15 nm, (2) 7−13 nm and (3) 10−11 nm. Reproduced with permission of The Royal Society of Chemistry from the study by Jiang et al. [128]. (**b**) (1) Schematic depiction of the synthetic process of Au−Fe_2C JNPs. HRTEM images of Au−Fe (2,3) and Au−Fe_2C (4,5) Janus NPs [129]. Copyright 2017 American Chemical Society. (c) HRTEM images of (1) 5 nm Au NPs, (2,3) dumbbell-like Au−Fe_3O_4 heterostructures, (4) 10 nm Au NPs, (5,6) flower-like Au−Fe_3O_4. Reproduce with permission of the American Chemical Society form reference [131]. Copyright 2011 American Chemical Society. (d) Schematic showing the sulfur-mediated coupling of Au−Pt−Fe_3O_4 heterotrimers to form higher-order hetero-oligomers, and TEM images of possible branched structures, along with the cartoon representations. Scale bars are 10 nm. Reproduced with permission from Macmillan Publishers Limited from the study by Buck et al. [132]. HRTEM, high-resolution transmission electron microscopy; NP, nanoparticle; TEM, transmission electron microscopy.

this work, they demonstrated that the shape of the heterostructures depended on the size of the Au seeds. When the seeds were small (4 nm), dumbbell-like structures were obtained (Fig. 4c). Histogram analysis of TEM images showed that the Au sizes were in the range 2.8−5.8 nm and the Fe_3O_4 in the range of 11−15 nm, with mean sizes of 5 and 12 nm, respectively. Hysteresis loops at 300 K gave a saturation magnetization (normalized to the unit weight of Fe_3O_4) of 41 emu/g.

3.5. Magnetic nanochains

Magnetic NPs can also be easily arranged into 1D chain-like structures, called nanochains (NCs), either by magnetic fields or by the use of biological synthesis in magnetotactic bacteria [133,134] (Fig. 5a). This offers a unique structure to further obtain MMNPs, for instance, by a subsequent coating to form core-shell NCs. NCs special disposition influences their magnetic properties creating directionality and magnetic anisotropy as opposed to isolated NPs or the bulk material [135,136]. These structures have shown potential in several applications in fields such as micromechanical sensors [137] given their particular interparticle interactions.

In addition, it has been demonstrated that such special disposition can influence the properties of the NCs, differentiating them from the isolated NPs or the bulk material [135,136]. In this sense, several groups have been interested in the synthesis of NCs and the tunability of their properties. For instance, Tadic et al. produced maghemite (γ-Fe_2O_3) NCs and studied their morphology, functionalization, colloidal stability, and magnetic properties, comparing them to the individual maghemite NPs that composed the chain [138]. First, maghemite NPs were synthesized by precipitation from an aqueous solution. Subsequently, nanoclusters of these NPs were produced, and their size was controlled by the combination of PAA and polyvinylpyrrolidone. These nanoclusters were further coated with silica so they could be later arranged in chain morphology and magnetically separated from the solution. The synthesized MMNPs had an average crystallite size of 9.8 nm, 80−100 nm cross-diameter, and 600 nm length (Fig. 5b) and were coated with a shell of silica of around 10 nm or 40 nm. Importantly, the large absolute zeta potential value for the NCs, provided by the silica coating, gave rise to an excellent colloidal stability. *M(H)* curves at 300 K exhibited a superparamagnetic behavior for both the NCs and the clusters. The magnetic moment of the NPs within the chain was larger than the one corresponding to isolated counterparts, thus beautifully demonstrating the structure-property dependence.

Another interesting case of this morphology was highlighted by the group of Yonghui Deng, who produced mesoporous aluminosilicate nanochains (MMAS-NCs) (Fig. 5c) with a well-defined core-shell-shell sandwich structure [139]. In this case, magnetite NPs of 160 nm diameter were synthesized via solvothermal method, so a silica shell could be coated latter. These Fe_3O_4@SiO_2 structures were arranged into NCs by exposing them to a 28.5 mT magnetic field. The NCs were coated again by a mesoporous silica shell to yield a Fe_3O_4@SiO_2@mSiO_2 structure. Depending on the water/n-hexane ratio used during the synthesis, diverse porous sizes were

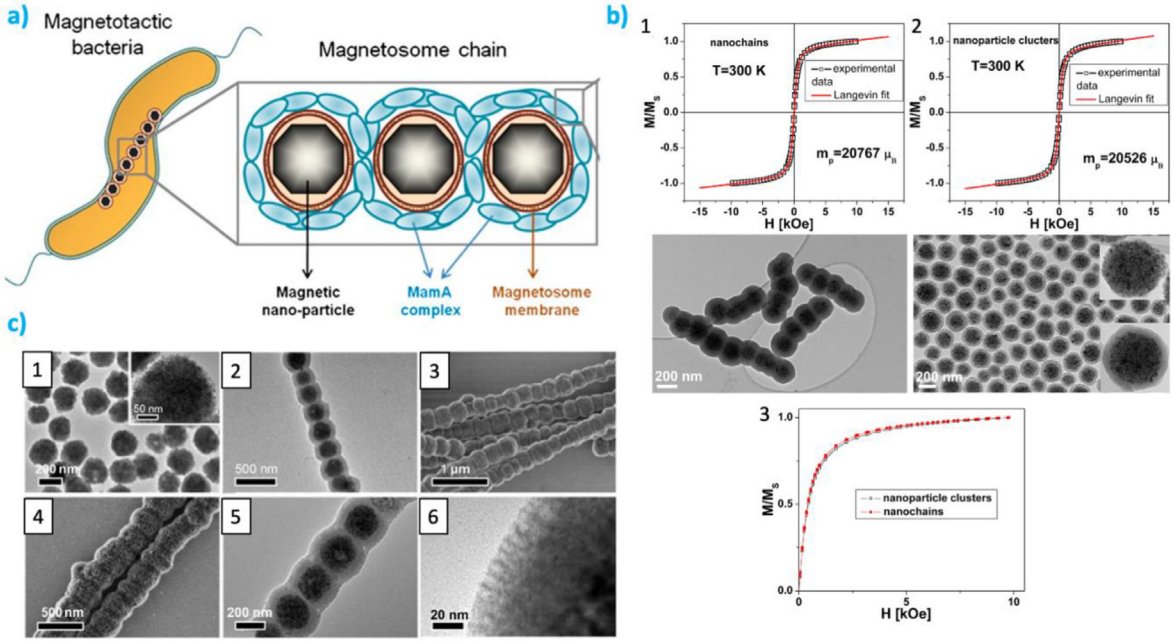

Fig. 5. a) Schematic representation of magnetotactic bacterium with a magnetosome chain. Reproduced with permission from the study by Kralj [134]. (b) Field-dependent magnetization curves and TEM images of (1) nanochains and (2) nanoparticle clusters at 300 K. The red line represents the fit to the Langevin function. Plot of M/M_S vs. H at 300 K for NCs and NP clusters (3). Reproduced with permission of Elsevier form reference [138]. (c) (1), (2), (5), and (6) show TEM and (3), (4) SEM images of magnetite particles (1), Fe_3O_4@SiO_2 nanochains (2,3), and (4–6) MMAS-NCs. The inset at (1) is a HRTEM image of the Fe_3O_4 nanoparticle. Reproduced with permission of Springer from the study by Zhang et al. [139]. HRTEM, high-resolution transmission electron microscopy; MMAS-NCs, mesoporous aluminosilicate nanochains; NC, nanochain; NP, nanoparticle; SEM, scanning electron microscopy; TEM, transmission electron microscopy.

obtained. Moreover, upon the combination of these porous structures with $AlCl_3 \cdot 6H_2O$, MMAS-NCs (Fe_3O_4@SiO_2@m$SiAlO_x$) were fabricated. According to TEM images, the magnetite NPs had a uniform size of around 200 nm, comprising 10 nm nanocrystals. In this sense, the Fe_3O_4@SiO_2 NCs had an average diameter of 300 nm with a silica layer of around 50 nm, and chain lengths ranging from 5 to 10 μm. Each of the NPs was separated from the others by a 20 nm silica interlayer. The resulting MMAS-NCs had a well-preserved 1D chain structure, with a diameter of around 350 nm and abundant mesopores. Owing to their properties, these structures could be used as green solid acid catalysts, where the magnetic core could concomitantly act as a magnetic separator and recycler, and the mesoporous outer shell possesses open channels with a large number of acidic sites adequate for mass transportation and diffusion. The peculiar structure of NPs arranged into chain-like structures offers distinct functional properties useful in applications such as wave absorption [140–142] or drug delivery systems [143].

3.6. Anisotropic NPs

Controlling anisotropy (this is, the change in properties depending on direction) at the nanoscale presents a new opportunity to access new functionalities [144]. Thus, many efforts have been devoted toward obtaining NPs exhibiting a variety of anisotropic shapes, therefore, enabling different avenues to further tailor the material's response. For instance, Au NRs have been extensively studied since their anisotropy originates two SPR dipolar modes: longitudinal and transversal [145]. An interesting approach was presented in our work [146], where core@shell Fe_3O_4@Au NRs, showing potential for both magneto- and photothermia synthesized. First, the Fe_3O_4 magnetic NRs were produced by a solvothermal method. Then, the NRs were functionalized with APTES, and 2–3 nm sized Au NPs were synthesized as well. The functionalized NRs were added to the solution containing the Au NPs to form core-satellite NR structures. The surfaces of these satellites were used as growing sites for the formation of a complete Au shell. Further, the NRs were included inside agarose hydrogels, and the vibrating sample magnetometer (VSM) measurement yielded a saturation magnetization of $M_S = 83.1$ A m^2/kg. Moreover, these NRs could be oriented within the hydrogel with an external magnetic field where they were arrested, showing the effects of anisotropy in the angle-dependent magnetization curves. The feasibility of these NPs was demonstrated in applications of combined magnetothermia and photothermia, where tunability and enhanced effect were produced by modifying the application angle.

Multicomponent NRs have also been studied as mechanochromic materials with predictable color changes in response to mechanical stimuli [147]. Mechanochromic films with precise colorimetric response were prepared with magneto-plasmonic NRs synthesized by colloidal methods. FeOOH NRs were first synthesized by a high-temperature hydrolysis reaction. Then, they were reduced to magnetite by a polyol process with a silica shell. These Fe_3O_4@SiO_2 NRs had a blocking temperature of 190 K, indicating superparamagnetism. Thereafter, the NRs were overcoated with a layer of resorcinol phenol (RF), the SiO_2 layer etched, and a single Au layer was grown perfectly parallel to the magnetic NR. This alignment allowed the control of the plasmonic resonance via a magnetic field, demonstrating that only some of the modes were activated. Further, mechanochromic devices, able to respond to torsion and pressure with changes in color, were prepared by mixing the multicomponent NRs with polydimethylsiloxane (PDMS).

Smart assemblies of NP clusters also allow the realization of anisotropic structures [148]. Magnetic-field induced assembly, for instance, has demonstrated the possibility of creating 1D structures

(nanochains), 2D structures (nanosheets), or even 3D crystals [149]. This assembly has been used, for example, to create orientation-dependent photonic systems [150]. Prussian Blue (PB) nanocubes were synthesized and coated with a layer of silica, and transformed into Fe_3O_4@SiO_2 nanocubes by a polyol process. The cubes had a $M_S = 32.5$ emu/g. Upon application of a magnetic field, the nanocubes tend to align into chain-like structures with parallel alignment to field directions. Compared with chains of NPs, these assemblies with nanocubes showed a strong dependence of the light diffraction on the chain orientation (this is, the orientation of the magnetic field), rather than only on the field strength. They demonstrated the applicability by creating encrypted patterns in polymeric films that could only be observed in certain directions.

Nanoplatelets also seem to present differences in their properties owing to their anisotropy. For instance, it has been demonstrated that the substitution of Sc in barium hexaferrite, which is a strategy employed to decrease the values of M_S, actually has the opposite effect on nanoplatelets [151], where this incorporation increased the magnetization from circa 16 A m^2/kg to over 38 A m^2/kg. These magnetic nanoplatelets can be actuated to disrupt phospholipid membranes, hence destroying cancer cells. The structures were exposed to a uniaxial alternating magnetic field (AMF) with frequencies ranging from 3 Hz to 100 Hz and amplitudes from 2.2 mT to 10.6 mT, while interacting with giant unilamellar vesicles, used as a model system of a cell membrane. After this interaction under the magnetic field, the membrane bending constant of the giant unilamellar vesicles decreased from 1.3×10^{-19} J to 0.86×10^{-19} J, showing that the magneto-mechanical actuation disrupted the membrane.

3.7. Other heterostructures

While the most common structures are summarized in the previous sections, there are other structures more difficultly categorized but that can present properties that are highly convenient for specific applications. Here we report some of those examples in relation to their properties and specific applications.

Polymeric vesicles (polymersomes), for instance, have been successfully synthesized with the incorporation of MNPs either in the surrounding layer interior or the vesicle interior [152,153]. Polymersomes have been widely employed as versatile drug delivery systems due to certain unique characteristics such as compartmentalization, chemical structure, and plasticity, ease to encapsulate different species, mechanical integrity, and colloidal stability. The most evident property-relationship of this structure is the high loading capacity and, when combined with MNPs, the high total magnetization for external manipulation. An elegant method for the controlled release of DOX using magnetically activated polymerosomes has been reported [153]. Ultrasmall superparamagnetic iron oxide nanoparticles were loaded inside polymersomes external layer by a solvent assisted method. First, the copolymer labeling was adjusted to 0.2 mol% by adding unlabeled Poly(trimethylene carbonate)-*block*-poly(L-glutamic acid) (PTMC-*b*-PGA). A solution in anhydrous dimethyl sulfoxide (DMSO) at 10 mg/mL was prepared. The hydrophobically coated Ultrasmall superparamagnetic iron oxide nanoparticles were added at a feed weight ratio (FWR = m_{load}/$m_{polymer}$ x 100) of 30%. The resulting solution was mixed with carbonate buffer (50 mM, pH 10.5). Possible applications of these polymerosomes include drug liberation upon the application of an AMF. In a different example, Ye et al. formed poly(lactic-co-glycolic acid) vesicles *via* emulsion-evaporation. This process of vesicle formation allowed the incorporation of a high number of elements. In this case, the vesicles were designed for use in anticancer treatments incorporating simultaneously an anticancer drug (busulfan) and inorganic NPs (IONPs and Mn:ZnS quantum dots) that added the multimodal imaging capabilities.

The group from Lin et al. also used larger Au NPs, which provided larger surface areas and multiple monocrystalline domains for nucleation of Fe_3O_4 NPs, to obtain flower-like structures, with saturation magnetization at 300 K of 51 emu/g [131]. Opposite to the case-of the Fe_3O_4@Au described in the core-shell section, in this case, the magnetic part is exposed and presents a multi-granular structure. This structure affects the magnetic properties and allows the water to be in contact with the surface. In Lin's study, it was noted that despite these values being smaller than that of bulk magnetite (90 emu/g), they were larger than previously obtained data from particles prepared by similar procedures. A seeded-growth approach is generally the selected method for the synthesis of flower-like structures, where thermal decomposition can be used to obtain precise control over the size of the NPs. Following this procedure, as an example, Au—Fe_3O_4 heterogeneous nanocrystals have been obtained [154]. Although the Au seeds could be obtained in a previous step or in situ, the former approach better controls the monodispersity of the final nanocrystals. In this work, the flower-like structures were obtained by the thermal decomposition of iron precursors (in particular $Fe(CO)_5$ and $Fe(acac)_3$) in the presence of Au NPs. They focused on how the different conditions of the synthesis affected the final product. For instance, when $Fe(acac)_3$ was used as a precursor instead of $Fe(CO)_5$, the heterostructures presented a more rounded shape, which suggests a different nucleation regime depending on the precursor. Furthermore, the molar ratio of Fe to Au also influenced the morphology of the crystals (and not only the nucleation of the iron oxides, as expected). In particular, in the presence of higher iron concentration, heterogeneous nucleation and growth are favored and, therefore, the larger presence of iron precursor led to multiple heterogeneous nucleations on the surface of Au NCs. Also, the coating layer and the surfactant play important roles in the synthesis process. Depending on whether the surfactant is OA or OAm, the morphology and aggregation of the nanocrystals changed. They concluded that both OAm and OA are necessary for obtaining homogeneous Au—Fe_3O_4 NCs, controlling aggregation, and size distribution. The coating was chosen depending on the iron precursor (OAm and 1,2-dodecanediol for $Fe(CO)_5$ and only OAm for $Fe(acac)_3$).

As the last example, it is possible to obtain MMNPs containing multiple nanoscale domains joined together by solid-state interfaces. This allows creating *ad-hoc* designed 'artificial molecules'. Although the complexity initially resided in the lack of a systematic approach to design these structures, Buck et al. were able to show how to apply a step-by-step synthesis procedure in a predictable manner [132]. Since Fe_3O_4-noble metal multicomponent NPs are highly stable, they chose the M-Pt-Fe_3O_4 heterotrimers (with M = Au, Ag, Ni, Pd) as the initial building block for higher-order structures. Pt—Fe_3O_4 heterodimers were synthesized by the thermal decomposition of $Fe(CO)_5$ in 1-ODE that contained Pt seed particles. Then, heterogeneous nucleation of Au on Pt—Fe_3O_4 was achieved through the reduction of a 1-ODE solution of $HAuCl_4$ with oleylamine (OLAM) in the presence of Pt—Fe_3O_4 heterodimers at mild temperatures (60–90 °C). The nucleation of the metals could be produced on the Pt or Fe_3O_4 ends of the heterodimer, on both ends, or even at their interface, thus giving different morphologies. Noteworthy, they were able to take this synthesis one step further, adding a third element to the already achieved nanostructures, thus forming heterotetramers, or even couple several Au—Pt—Fe_3O_4 heterotrimers to form hetero-oligomers, just by heating the heterotrimers to 120–150 °C with a trace amount of sulfur powder in tricotylamine (Fig. 4d). The structure-properties relationship in this kind of structures highly depends on the materials; it allows access of the solvent to the individual components, in many cases independent functionalization, and a versatile approach that opens the possibility to generate more complex morphologies with

Table 2
Summary of typical multicomponent nanostructures, preparation methods, materials and structure-properties.

Structure	Preparation methods	Materials	Properties
Core@shell	Adsorption from precursor (inorganic) Grafting to/Grafting from (organic) Molecular self-assembly (Oldenburg method) Aerosol photopolymerization	Core Iron oxide nanoparticles (Fe_3O_4, Fe_2O_3), Fe_2P, inorganic semiconductors (ZnO, TiO_2) Shell Inorganic (Au, Si), organic (BuA)	Core protection with shell Magnetization enhancement SPR tuning in metal nanoshells
Yolk-shell	Selective etching Kirkendall-effect-based methods Ostwald ripening Sacrificial template	Yolk Iron oxides (Fe_3O_4, Fe_2O_3), $ZnFe_2O_4$ Shell SiO_2, $ZnFe_2O_4$, $MgSiO_3$	Loading capability Independent properties of yolk and shell Improved catalysis
Core-satellite	Heterogeneous nucleation and growth Covalent attachment of satellites	Iron oxide cores Au satellites	Hot spots in the gaps between satellites and SPR tuning Access of solvent to the core
Janus nanoparticles	Seed-mediated growth Thermal decomposition in the presence of seeds	Fe_3O_4–Au Fe_2C–Au	Broken symmetry and directionality Independent functionalization Access of solvent to the different parts
Magnetic nanochains	Precipitation from an aqueous solution Solvothermal	γ-Fe_2O_3 Fe_3O_4@SiO_2	Magnetic shape anisotropy, magnetization enhancement, stability.
Other heterostructures: hetero-oligomers (artificial molecules)	Heterogeneous nucleation	M-Fe_3O_4 (M = Pt, Au, Ag, Ni, Pd)	Higher number of materials Structure versatility Incorporation in organic structures

high potential for futures applications. A summary of the aforementioned structures, the materials employed and the properties related to those structures can be found in Table 2.

4. Multicomponent NPs for advanced applications

4.1. Biomedical

4.1.1. Multimodal imaging

Imaging techniques enable the understanding of complex biological processes. They have been implemented and become an essential tool in the healthcare field for many years, facilitating the diagnosis of, among others, complex diseases such as cancer, or Alzheimer's. These imaging techniques have been classified into two main categories: morphological (or anatomical) and functional (or molecular) [155]. Morphological techniques (such as ultrasound, X-ray computed tomography (CT), MRI, and magnetic particle imaging (MPI)) are generally characterized by high spatial resolution but lower sensitivity. On the other hand, molecular imaging techniques like positron emission tomography (PET), single-photon emission computed tomography, or photoacoustic imaging (PAI) show a higher sensitivity but lower spatial resolution.

MNPs have found applications in biomedical imaging for a long time. They have been commonly used not only as contrast agents for MRI generally as a T_2 (negative) contrast but also as a T_1 (positive) contrast for the case of very small SPIONs [156]. They act also as the basic contrasts agents in MPI, and when further functionalized with a radioactive isotope attached to them (or as doping agents), they can be also employed in techniques like PET and single-photon emission computed tomography. However, the different characteristics of each imaging modality (penetration depth, spatial and temporal resolution, exposure to ionizing radiation, contrast of the different tissues, etc.) render almost impossible to find a unique method that fulfills the conditions of whole-body, highly resolved, and video-framed imaging at once [79]. Hence, multimodal imaging is one of the fields in which the application of multifunctional and multicomponent nanostructures offers more possibilities since the ability of these NPs to serve as probes or contrast agents for two or more imaging methods (as shown in Fig. 6) can supplement the limitations of individual techniques and allow for better-rounded bioimaging.

Different materials can be used depending on the imaging modality. For instance, MNPs (in particular superparamagnetic ones) can be applied as contrast agents for MRI, whereas NPs of high Z-number seem to be appropriate for CT imaging due to their high X-Ray attenuation coefficient [158]. One of the main issues with the selection of materials is that, for them to be useful in a clinical setting, it is paramount that those materials are biocompatible. Inorganic nanomaterials, such as the ones previously mentioned, often show different downsides that impede their approval for clinical use. Thus, we will focus here on the most common materials that are being studied, namely iron and its oxides. The combination of these components, or their functionalization with other elements (e.g. gold, gadolinium), allows the development of multicomponent nanomaterials for two or more types of imaging techniques.

MRI is a non-invasive imaging technology that produces three-dimensional, detailed anatomical images. Employing magnets that produce a strong magnetic field, water protons in the body are forced to align with that field. Then, when a radiofrequency current is pulsed through the patient, the protons are taken out of equilibrium. Upon releasing the alternate current, the MRI sensors are able to detect the energy released by the protons when they realign with the magnetic field. The time it takes for the protons to realign (T_1 in the direction of the magnetic field, *longitudinal*) or loss of magnetic phase (T_2, perpendicular to the magnetic field, *transverse*) depends on the environment and chemical properties of molecules, allowing distinguishing between different tissues. Furthermore, contrast agents can be introduced to modify the relaxation times, producing contrast in the image (darker or brighter regions). The capability of those materials to modify those relaxation times is called the relaxivity (r_1 and r_2) and it is defined as the slope of the inverse of the relaxation times with the concentration. Paramagnetic materials are known to modify the longitudinal relaxation processes of the water protons (named T_1 processes), whereas superparamagnetic and ferromagnetic and ferrimagnetic materials (like SPIONs) modify the transverse (or T_2) relaxation processes [158].

Since Fe oxides are contrast agents for MRI, it is also possible to combine both materials to produce dual contrasts for T_1 as well as T_2. With this in mind, Li et al. synthesized multicomponent core/shell Fe_3O_4/Gd_2O_3 nanocubes for enhanced T_1-T_2 MRI (Fig. 7a) *via* one-step thermal decomposition of a mixture of iron oleate and gadolinium oleate precursors. After preparing the multicomponent nanomaterial, they compared the r_1 and r_2 relaxivity together with that of Gd_2O_3 NPs and Fe_3O_4 nanocubes. The saturation

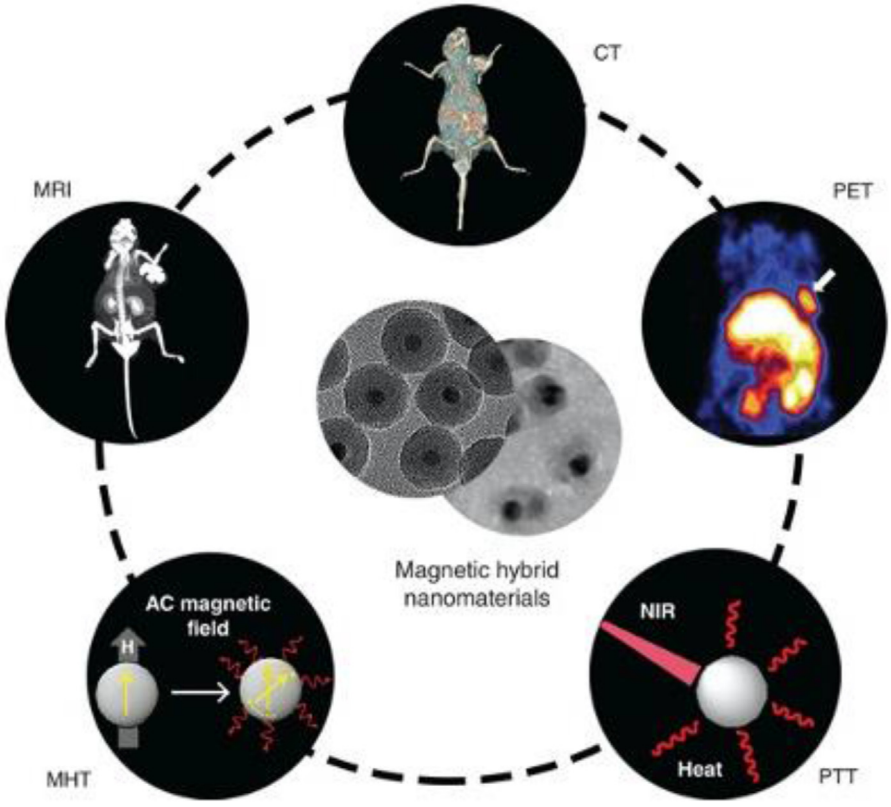

Fig. 6. Schematic illustration of the different functions of MMNPs in biomedical diagnosis and treatment. Reproduced with permission of Wiley from the study by Tian et al. [157]. MMNP, multicomponent magnetic nanoparticle.

magnetization of the Fe_3O_4/Gd_2O_3 nanocubes was 24.9 emu/g, which was lower than one from the Fe_3O_4 nanocubes alone (Fig. 7b), probably due to the reduction of iron oxide content in the structure. Interestingly, the multicomponent Fe_3O_4/Gd_2O_3 nanocubes exhibited r_1 and r_2 of 45.2 ± 0.8 mM^{-1}/s and 186.5 ± 6.0 mM^{-1}/s, respectively, which is a two-fold increase from those obtained for isolated Gd_2O_3 NPs (23.16 ± 2.2 mM^{-1}/s) and Fe_3O_4 nanocubes (93.27 ± 2.6 mM^{-1}/s), when MRI phantom studies were performed. They attributed the r_1 increase to the slower tumbling rate and the r_2 increase to an additional synergistic contribution of T_2 shortening by the Gd ion sitting adjacent to the iron in the multicomponent nanocubes [159]. Moreover, cytotoxicity studies demonstrated that the nanocubes were indeed biocompatible and *in vivo* imaging of rats at 3.0 T showed positive and negative T_1 and T_2 contrast after injection (Fig. 7c).

As mentioned above, iron oxides are also widely used in biomedical imaging since they present excellent *in vivo* biocompatibility, good colloidal stability, and tunable surface modifications [160]. Even more, superparamagnetism in IONPs is especially relevant since it allows to magnetically target and handle the particles and serves as contrast agents for T_2-weighted MRI [161]. As an example, we combined an iron oxide core with a branched gold nanostar in a Janus-like configuration, in which the final Janus magnetic nanostar (JMNS) has two chemically different surface regions [88,127]. The JMNS were synthesized starting from gold nanospheres that were used as seeds for gold-iron oxide nanodumbbells, subsequently using those as seeds for the directional growth of asymmetric gold nanostars. The seed–mediated growth process offered high tunability on the nanostar size varying from 20 up to more than 100 nm while two versions of the iron oxide were obtained with 15 and 20 nm diameter size (Fig. 8a). The nanostar morphology offered tunability on the SPR with excitation in the near-infrared (NIR) region (biological transparency window), what offers the possibility to be used as contrast agents in PAI where the sample is excited with light and the recording is made with the generated ultrasounds. Furthermore, the NPs offer contrast capabilities for MRI (iron oxide lobe) and CT (Au X-ray attenuation). Finally, the Janus nanostars offered several imaging capabilities for *ex vivo* or *in vivo* experiments such as simultaneous bright and dark field optical microscopy, and SERS sensing and mapping [88,162]. In a similar example, PEGylated branched Au–Fe_3O_4 JNPs prepared through a simple hydrogen reduction method (of Au–$Fe(OH)_3$ JNPs) and subsequent Au branched growth, resulted advantageous for MRI, and CT and PAI [163]. A large iron oxide core and a small Au nanostar was found to be the best configuration for MRI, while the presence of gold yielded promising results in CT (due to the high atomic number) and PAI (because of the localized SPR of Au). Other groups have explored the Janus configuration as well for iron, either in combination with gold [129] or with polymers [164] with multimodal imaging capabilities.

Another configuration that has extensively been explored for multimodal imaging is that of core@shell structures. However, one potential issue with these structures is that, when an inorganic material is directly deposited onto the IONP, it seriously limits the proximity of water protons to the magnetic material, reducing its capacity to act as an MRI contrast. In light of this fact, Li-Sen Lin et al. [165] proposed a sub-100 nm yolk-shell nanostructure in which the Fe_3O_4 core is inside a hollow cavity and surrounded by a porous Au shell (Fig. 8b). They used the iron oxide core, which was surrounded by a SiO_2 interlayer and, after forming the porous Au

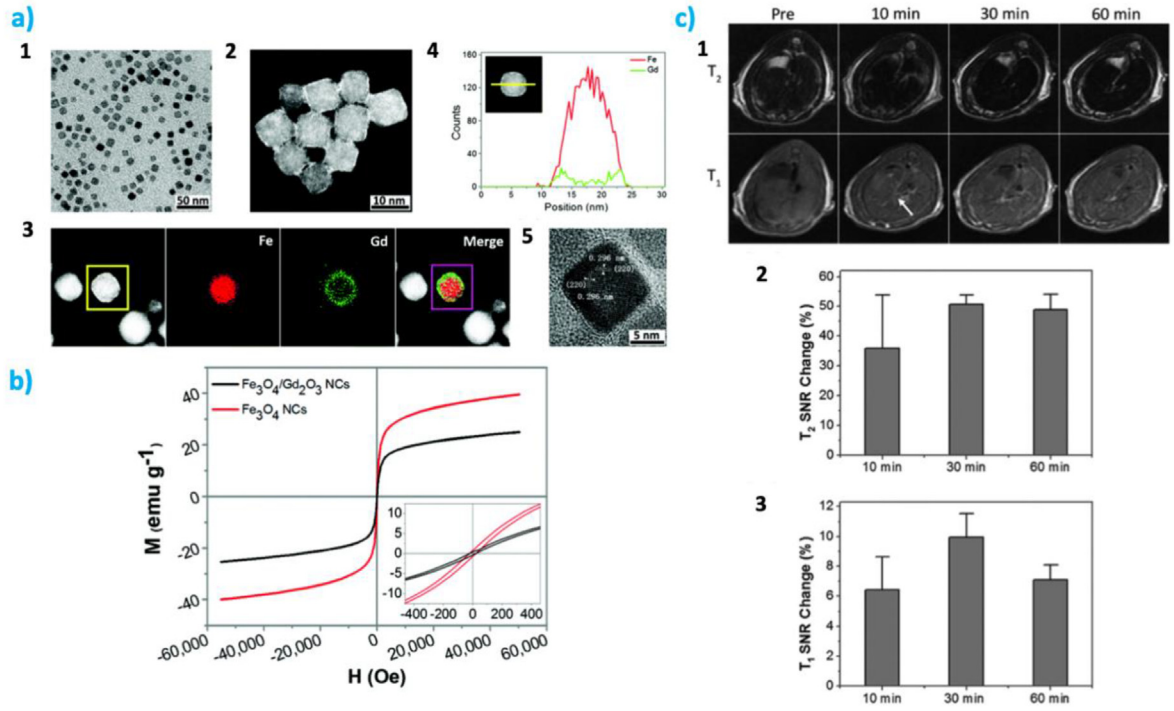

Fig. 7. (**a**) Characterization of Fe_3O_4/Gd_2O_3 nanocubes. (1) TEM image of the monodisperse nanocubes. (2) STEM-HAADF image of core/shell nanocubes. (3) EDX mapping images of one nanocube. (4) EDX line profiles across a nanocube. (5) HRTEM image of one nanocube. Reproduced with permission of The Royal Society of Chemistry from the study by Li et al. [159]. (**b**) Magnetic properties of Fe_3O_4/Gd_2O_3 nanocubes. Field-dependent magnetization curves (M–H) of the Fe_3O_4/Gd_2O_3 nanocubes (black line) and Fe_3O_4 nanocubes (red line) at 300 K. Inset shows both curves in the low-field region. Reproduced with permission of The Royal Society of Chemistry from the study by Li et al. [159]. (**c**) *In vivo* MRI studies on rats at 3.0 T. (1) T_2 and T_1 weighted MR images before and after intravenous injection of Fe_3O_4/Gd_2O_3 nanocubes at a concentration of 2.0 mg of Fe per kg of rat bodyweight (top: T_2 imaging, bottom: T_1 imaging, the arrow indicating the hepatic vascular). SNR changes in the liver of T_2 (2) and T_1 (c) weighted images after administration. Reproduced with permission of The Royal Society of Chemistry from the study by Li et al. [159]. EDX, energy-dispersive X-ray spectroscopy; HRTEM, high-resolution transmission electron microscopy; MRI, magnetic resonance imaging; SNR, signal-to-noise ratio; STEM-HAADF, scanning transmission electron microscopy-high-angle annular dark-field; TEM, transmission electron microscopy.

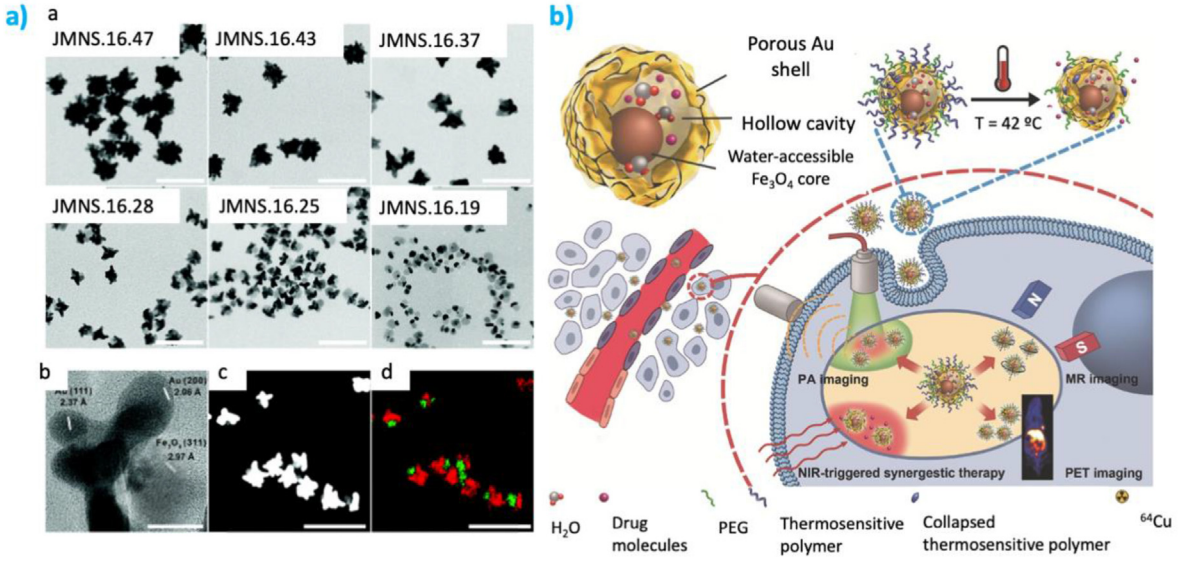

Fig. 8. **a**) (a) TEM images of different JMNSs obtained by varying the ratio of nanodumbbells-seeds to gold salt. As the NP size decreases, the iron oxide part (light grey) can be distinguished from the gold domain (dark grey or black). (**b**) HRTEM image of a NP showing single-crystal nanostar tips and Fe_3O_4. (**c**) HAADF-STEM image of a JMNS, where gold appears white while iron oxide appears grey. (d) EDX mapping of Fe (green) and Au (red) domains in (c). Reproduced with permission from The Royal Society of Chemistry from the study by Reguera et al. [88]. (b) Schematic illustration of the design and application of sub-100 nm yolk-shell Fe_3O_4@Au NPs for MR/PA/PET multimodal imaging. Reproduced with permission from Wiley-Vch from the study by Lin et al. [165]. EDX, energy-dispersive X-ray spectroscopy; HAADF-STEM, high-angle annular dark-field-scanning transmission electron microscopy; JMNS, Janus magnetic nanostar; NP, nanoparticle; PET, positron emission tomography; TEM, transmission electron microscopy.

outer shell, the SiO_2 template was removed. To demonstrate the effectiveness of this structure in preventing the decline in MRI contrast, they compared the relaxivities of the yolk-shell nanostructures with those of a core@shell NP with the same materials. They found that the r_2 for the yolk-shell was 149.4 s^{-1}/mM, compared to 61.9 s^{-1} m/M for the core@shell, resulting in a better contrast and signal-to-noise ratio for MRI. Furthermore, the nanoshell configuration and presence of the hollow cavity caused a redshift in the localized surface plasmon resonance (LSPR) of gold, yielding a strong NIR absorption from 650 to 850 nm (inside the biological transparency window of biological tissues) and making the yolk-shell structure particularly promising for PAI. Finally, by directly depositing a ^{64}Cu radiolabeling agent on the Au surface, they were also able to test the effectiveness of this structure as a contrast for PET imaging. The maximum uptake values in U87MG tumor-bearing mice were 8.55% injected dose·g^{-1} 24 h after injection. Apart from the imaging capabilities, the yolk-shell NPs can potentially be used for drug delivery as is discussed below (section 4.1.3).

We also wanted to highlight the importance that MMNPs have had on the development of novel, non-invasive imaging techniques, such as MPI. MPI was initially proposed by Gleich and Weizenecker [166] and is based on the use of time-varying magnetic fields to directly detect IONPs, instead of indirectly using them on MRI. MPI promises high depth penetration, positive contrast, no radiation, and nearly no background from tissues [167]. In this sense, the synthesis of IONPs with high MPI signals has been reported [164]. A thermal decomposition method of iron-oleate complex in the presence of OA was utilized, with a fixed reaction temperature of 310 °C and different reaction times. TEM images showed relatively uniform sizes, from 14.1 to 16.2 nm depending on the reaction time. Furthermore, the particles were encapsulated in fluorescent semiconducting polymers to produce Fe_3O_4@semiconducting polymer NPs. The performance of the synthesized NPs was compared with a commercial MPI agent (ferucarbotran) and a commercial MRI agent (Feraheme). The MPI signal of the prepared NPs was three times bigger than one of the commercial agents (Vivotrax) and seven times higher than the other (Feraheme) at the same concentration of Fe. Moreover, the encapsulation of the particles on the semiconducting polymer Poly [2,7-(9,9-dioctylfluorene)-*alt*-4,7-bis (thiophen-2-yl)benzo-2,1,3-thiadiazole] (PFODBT) did not produce negative effects on the MPI signal intensity and, what is more, provided good labeling of cells, having the potential for *in vivo* long-term cell tracking by MPI and fluorescence imaging.

Finally, the use of MMNPs makes it possible to combine imaging techniques for diagnosis with therapy applications becoming a complete theranostics biomedical-tool. For instance, a theranostic agent based upon the combination of gold-graphene (Au-rGO) MMNPs decorated with SPIONs has been synthesized [168]. This MMNP was built with four capabilities combined: self-guided MRI, SERS, PTT, and chemodynamic therapy. This nanoprobe was synthesized first by producing graphene oxide, which was later converted into a multicomponent NP by developing 15 nm size gold nanoseeds over the reduced graphene oxide (rGO) layers. Then, the surface was modified with 4-aminothiophenol, which acts as a SERS reported, and finally conjugated with the SPIONs to obtain the final MMNP. The final product presented superparamagnetic behavior, and T_2 relaxivity of 62.8 mM^{-1}/s. A photothermal conversion efficiency of 19.6% was also reported, with the ability to raise the temperature from 27.6 °C to 43 °C in 5 min, when irradiated with a 2 W/cm^{+2} laser (808 nm) at a concentration of 50 μg/mL. *In vivo* studies also confirmed the efficacy of the nanoagents to reduce tumor size in comparison with the control group. Other multicomponent materials have also been reported as theragnostic agents [169,170].

4.1.2. Hyperthermia

Thermal therapies comprise all therapeutic treatments based on the transfer of thermal energy into or out of the body. This includes treatments in oncology, physiotherapy, urology, cardiology, or ophthalmology among other areas of medicine. Thermal therapies have experienced a renewed interest in the last two decades thanks to the use of nanomaterials that can be activated *via* heating, also called nanothermo-therapies, with special relevance in the treatments of cancer tumors [171,172]. The use of NPs allows much higher spatial and temporal control than conventional hyperthermia treatments. Different from other treatments, nanothermotherapies require two events for local heating: first, it is the presence of NPs in the tumor tissue, this is produced by enhanced accumulation, passively by EPR effect or actively through targeting and guiding strategies; and second, an external stimulus such as electromagnetic radiation or AMF. This produces discrimination between healthy and malign tissue in the region of stimulus application as well as prevents the activity on other organs where NPs tend to accumulate naturally (liver, kidneys, etc.). Moreover, the structure of NPs can be made to accommodate active molecules simultaneously allowing combinatorial cancer therapy with different drugs, targeting, imaging, or biomimetics to bypass cellular membranes and overcome drug resistance mechanisms. Although the particles can be used on their own as a standalone treatment, usually they are employed as sensitizers to enhance the effect of other therapies [173].

Magnetic field-induced hyperthermia, also called magnetic hyperthermia (MHT), is based on the use of magnetic particles as heating mediators when subjected to an AMF [174]. Depending on the reaching temperature, the treatment can be differentiated between low-temperature hyperthermia (40–41 °C for 6–72 h), moderate-temperature hyperthermia (42–45 °C for 15–60 min), and thermal ablation or high-temperature hyperthermia (>50 °C for > 4–6 min). Cancer treatment makes use of either moderate-temperature hyperthermia or high-temperature hyperthermia. While the requirements in terms of concentration and AMF for the case of moderate hyperthermia are milder, this low hyperthermia is in general not enough for complete treatment and is used in combination with other cancer treatments such as chemotherapy, radiotherapy, and so on. On the other hand, high-temperature hyperthermia produces complete ablation of the tumors but requires more extreme conditions, such as the direct injection of a high concentration solution of NPs in the tumor tissue and the application of high magnetic fields and frequencies. The heating ability of magnetic NPs under an AMF is expressed by the specific absorption rate or more correctly the specific loss power (SLP), which provides a measure of the rate at which energy is absorbed per unit mass of the magnetic NPs. Eq. (1) describes the calculation of SLP through the measurement of the induced heating or directly measuring the magnetization loop. m in Eq. (1) is the mass of heat-generating material, C the thermal capacity of the whole sample and (dT/dt) the rate of temperature increases as a function of time, f the frequency, and M and H the magnetization and magnetic field strength respectively. Alternatively, although not typically reported, the intrinsic loss power could be used by normalizing the SLP by the frequency and field amplitude and allows a better comparison among different works [175].

$$SLP = \frac{C}{m}\left(\frac{dT}{dt}\right)_{t\to 0} = f\int_{-H_{max}}^{H_{max}} \mu_0 M(H)dH \tag{2}$$

Increasing the magnetic field strength and frequency increases the SLP; however, for a safe application of hyperthermia to patients, it has been experimentally found that the product of the frequency and the magnetic field amplitude (*fH*) should be smaller than a threshold limit, between 4.85 10^8 and 9.6 10^9 A/m/s depending on the analysis type [176–178]. To further increase the SLP at a reasonable NP concentration, it is necessary to develop magnetic NPs with a higher efficient magnetothermal conversion efficiency. This involves the development of new synthesis methods with a better control of composition, shape, size, and uniformity as well as an improvement in our understanding of their effect on heating efficiency. Although this is a complex task, it is known for instance that surface and magneto-crystalline anisotropies play an important role and highly increase the SLP from the bulk form [179,180]. Magnetothermal therapy is based on different mechanisms including hysteresis loss, Néel relaxation and Brown relaxation to convert the energy of an external magnetic field into heat [172,176]. The hysteresis mechanism of MHT takes place in multi-domain NPs. During a quasistatic *H-M* cycle, a hysteresis is produced due to the displacement of domain walls being pinned and released at inhomogeneities and to the rotation process of magnetic moments inside domains. Néel relaxation mechanism is produced in single domain NPs, where the energy barrier for magnetization reversal decreases, and consequentially, thermal fluctuations lead to relaxation phenomena also called Néel relaxation. In this case, the frequency of the AC magnetic field is high enough that the physical orientation of the particle remains unchanged while the moment alternates between parallel and antiparallel orientations with an energy barrier $K{\cdot}V$ (being K is the magnetic anisotropy and V the NP volume). Néel relaxation prevails when there is a higher frequency as well as smaller particle size. In fluid suspensions, another relaxation path, called Brown relaxation, may take place due to the ability of particles to freely rotate. In this case, heating of the NPs occurs due to viscous drag between the particles and the liquid, where the entire particle has a rotational movement with an applied AMF, while the magnetic moment remains fixed relative to the crystal axis. The Brownian relaxation is size-dependent being dominant at the higher particle size and strongly viscosity dependent.

Together with the improvement of the magnetothermal properties, these NPs offer unique properties in imaging (MRI, MPI, etc.) and, in general, good biocompatibility. Furthermore, the combination with other materials allows them to show enhanced properties or to include new functionalities. One example of this is the formation of core@shell NPs where the shell can act as a protective shield for sensitive core materials. The interface of the two materials can be also used to modify the anisotropy constant and therefore produce superior heating properties [181]. Core@shell Fe@Fe_xO_y NPs, for instance, present a high magnetic moment core and they are protected from oxidation by the Fe_xO_y shell. However, for longer terms, a deterioration of the NP can produce degradation and shrink of the NP core diminishing the magnetic properties, therefore requiring additional protection layers. Faminay et al. showed, by using a coating strategy, a resistance of core@shell Fe@Fe_xO_y@PMA MMNPs (PMA stands for poly(isobutylene-alt-maleic anhydride) over two months and an SLP value as high as 660 W/g [182]. Many other combinations have been produced to optimize the magnetic anisotropy through a core@shell structure, including Mn and Co ferrites [183], and different ferrites of Co, Mn, and Zn, including $CoFe_2O_4$@$MnFe_2O_4$, $CoFe_2O_4$@Fe_3O_4, $MnFe_2O_4$@$CoFe_2O_4$, Fe_3O_4@-$CoFe_2O_4$, $Zn_{0.4}Co_{0.6}Fe_2O_4$@$Zn_{0.4}Mn_{0.6}Fe_2O_4$, Fe_3O_4@$Co_xZn_{1-x}Fe_2O_4$ [184,185]. These materials have presented SLP values ranging from 100 to 450 W/g for single-component and between 1000 and 4000 W/g for core@shell NP (Fig. 9) [184]. Other core@shell NPs include those coated by SiO_2 such as $Co_{0.03}Mn_{0.28}Fe_{2.7}O_4$@$SiO_2$ reaching an SLP value of 3417 W/g and the more biocompatible $Zn_{0.3}Fe_{2.7}O4$@SiO_2 NPs achieve SLP of 500 W/g_{metal} [186]. Fe_3O_4@Au NPs have also shown enhanced hyperthermal properties with SLP changing from 313 to 463 W/g upon the core@shell formation while presetting the high biocompatibility of the two materials and the stability given by the Au shell [187].

Together with MHT, PTT is the other major group of nanothermotherapies. In this case, the heat is produced by irradiating a NP-containing sample with NIR light in the biological transparency window [188]. The main groups of NPs are carbon-based and noble metal NPs, mainly Au and Ag exhibiting a SPR [172,189]. Both MHT and PTT present advantages and disadvantages, PTT is simpler to apply with laser or LED illumination and requires mild conditions in terms of light dose and NP concentration. Its main disadvantage is, however, its low penetration depth typically in the order of 1 cm when irradiating in the NIR, and the fact that it requires the use of fiber optics insertion for non-superficial treatments. On the other hand, MHT can be applied to any part of the body but it requires a much higher NP concentration to achieve enough heating to cause an effect. The combination of both therapies can be used to overcome the single treatment drawback. Magnetic NPs such as IONPs present absorption in the NIR and therefore can produce a photothermal effect [190]. However, due to the low extinction coefficient, it requires a high NP concentration. Alternatively, MM-plasmonic NPs can be combined to produce simultaneous PTT and MHT effect. The combined effect is not only limited to hyperthermia but also other nanomaterials properties, such as being a multimodal imaging contrast for simultaneously MRI, MPI, PA, and CT, magnetic guiding, or spectroscopy surface-enhanced techniques, are highly beneficial in any biomedical therapy.

Different NPs have been formulated to produce simultaneous PTT and MHT, most of them combining Fe_xO_y:Au as both materials present excellent biocompatibilities. Espinosa et al. showed, for example, the use of assemblies of core-satellite NPs formed by a multi-NP magnetic core of ~40 nm surrounded by smaller Au NPs to obtain NPs between 47 and 63 nm [191]. Core@shell structures can be also used to modify the plasmonic response of the NPs and present absorption in the red and NIR part of the spectrum allowing its use in simultaneous MHT:PPT (Fig. 10). Fiorito et al. synthesized Fe_3O_4–Au–$Cu_{2-x}S$ trimeric heterostructures that not only combined PTT and MHT but also added ^{64}Cu for radio-insertion for PET [192]. Abdulla-Al-Mamun et al. obtained Fe_3O_4@Au core@shell nanocubes, where the combined effect produced temperature increases up to 22 °C in 5 min [193]. The use of PTT with a very low intensity of 0.03 W/cm white light was enough to increase 6 °C with respect to the Fe_3O_4 NPs in the simultaneous MHT:PTT hyperthermia treatment obtaining a 100% killing of cancer cells in an *in vitro* assay of HELA cell culture [193]. Core@shell NPs of Fe_3O_4 and Ag have also been assayed with a flower-like Ag@Fe_3O_4 structure [194]. In this case, the SLP was increased one order of magnitude after applying dual heating with regard to MHT, from 10 to 130 W/g (for H_{AC} = 200 Oe, f = 310 kHz and P = 0.93W/cm^2). The use of both heating mechanisms allowed the use of mild conditions of the magnetic field and irradiation power; however, due to the lower wavelength of the plasmonic band of spherical Ag, they required illumination with 422 nm laser, which makes it impractical for *in vivo* applications.

To overcome the problem of low-wavelength response, strategies to obtain more anisotropic NPs (that produce a red-shift in the plasmonic band) are required. Espinosa et al. used Janus Fe_3O_4–Au NPs where the Au part presents branched-nanostar morphology [195]. The nanostar presents a plasmonic band in the 650–800 nm highly suitable for PTT. They reported an SLP_{MHT} of 15 W $g^{-1}_{Fe3O4+Au}$ that corresponds to 140 W g^{-1}_{Fe} and a much higher SLP_{PTT} of around 18 000 W $g^{-1}_{Fe3O4+Au}$ at low concentrations ([Fe] = 0.05 mM) that substantially decreases for higher

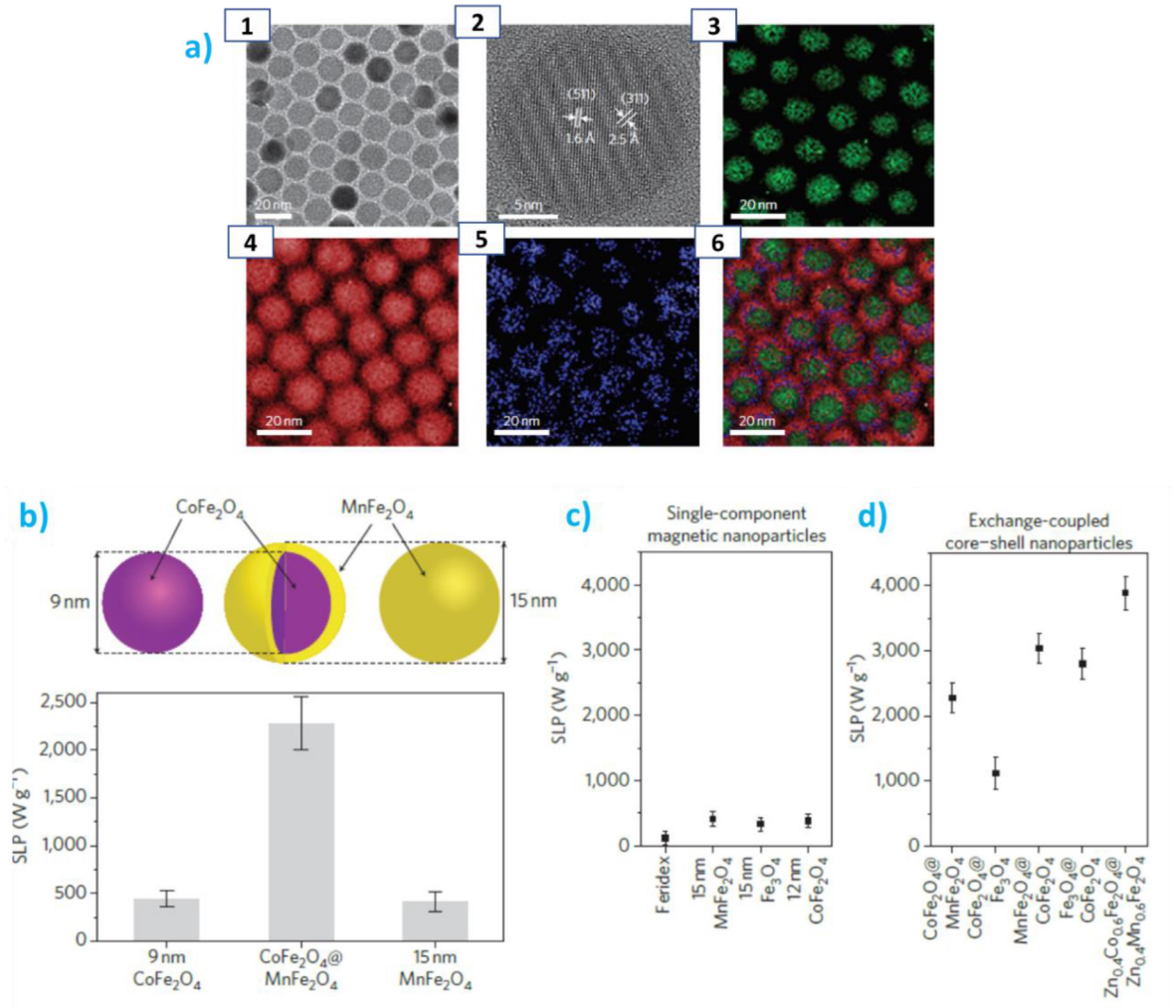

Fig. 9. (**a**) Morphological analyses and magnetic measurements of core@shell NPs: 1: TEM image and 2: high-resolution TEM image of 15 nm$CoFe_2O_4$@$MnFe_2O_4$, showing the narrow size distribution and single crystallinity. 3–6: electron energy loss spectroscopy (EELS) mapped images: Co mapped image (3), Fe mapped image (4), Mn-mapped image (5), and overlay image of 3–5. (b) SLP comparison of magnetic NPs. Schematic of 15 nm $CoFe_2O_4$@$MnFe_2O_4$ NP and its SLP value in comparison with the values for its components (9 nm $CoFe_2O_4$ and 15 nm $MnFe_2O_4$). (c) SLP values of single-component magnetic NPs (Feridex and MFe_2O_4; M¼Mn, Fe and Co) and various combinations of core@shell NPs ($CoFe_2O_4$@$MnFe_2O_4$, $CoFe_2O_4$@Fe_3O_4, $MnFe_2O_4$@$CoFe_2O4$, Fe_3O_4@$CoFe_2O_4$, $Zn_{0.4}Co_{0.6}Fe_2O_4$@$Zn_{0.4}Mn_{0.6}Fe_2O_4$). (d) SLP values range from 100 to 450 W/g for single-component magnetic NPs and values for core@shell NPs range from 1.000 to 4.000 W/g (f = 500 kHz, H0 = 37.3 kA/m). Reproduced with permission of Nature Publishing Group from the study by Lee et al. [184]. NP, nanoparticle; SLP, specific loss power; TEM, transmission electron microscopy.

concentrations due to the absorption saturation SLP_{PTT} = 104 W $g^{-1}_{Fe3O4+Au}$ at [Fe] = 24 mM (470 kHz, 18 mT, and 0.8 W/cm^{+2}, 680 nm). While at low concentrations, the MHT heating is negligible in comparison with the PPT, at high concentrations the dual-mode could be used to overcome the saturation produced in the PPT, passing form SLP_{PTT} = 104 W $g^{-1}_{Fe3O4+Au}$ to a SLP_{Dual} = 130 W $g^{-1}_{Fe3O4+Au}$ at [Fe] = 24 mM. In the same work, the tumor treatment was addressed applying the more effective PTT together with magnetic guiding. The magnetic guiding increased the NP concentration at the tumor site after systemic intravenous injection (3.4% in comparison with 1.5% without the magnet), which in turn elicited an improved therapeutic action, leading to total tumor inhibition growth [195]. Together with this last work, many other plasmonic MMNPs have been applied for combined PTT and magnetic guiding, highly improving the treatment efficacy. The preferred materials for this case tend to be Au-Iron oxide due to the proven biocompatibility of the two materials, and with the morphology being a key parameter in the performance of the system. Among the different morphologies are Au@Fe_3O_4 porous core@shell [196], $Au_{Nanorod}$@Fe_3O_4 core@satelite-shell [197], and Au@Fe@Au multishell [198]. The porosity created in some of the cases allowed the combination with drug delivery generating a multi-variable approach [196], in the goal of complete cancer treatment with very low side-effects.

Finally, together with the hyperthermia capacity of magnetic and plasmonic NPs, heat monitoring can be of special interest for clinical translation of the therapy and fine-tune the therapeutic effect. The temperature in the tumor tissue can be measured in different ways, such as with optical fibers, infrared thermometers, MRI, and so on. However, a more interesting approach is the measurement of the temperature at the NP, ultimately the cause of cell damage and therefore of the therapeutic effect, and where a high discrepancy can appear with respect to the microenvironment temperature. Recently, a direct measurement has been proposed using X-ray absorption spectroscopy on a single component and JNPs [199]; however, its use requires the use of a synchrotron source. A simpler approach is the use of luminescent probes based on the emission of one or several rare-earth elements. The temperature in those cases is calibrated as a function of luminescent intensity, relaxation time, or ratio between different band

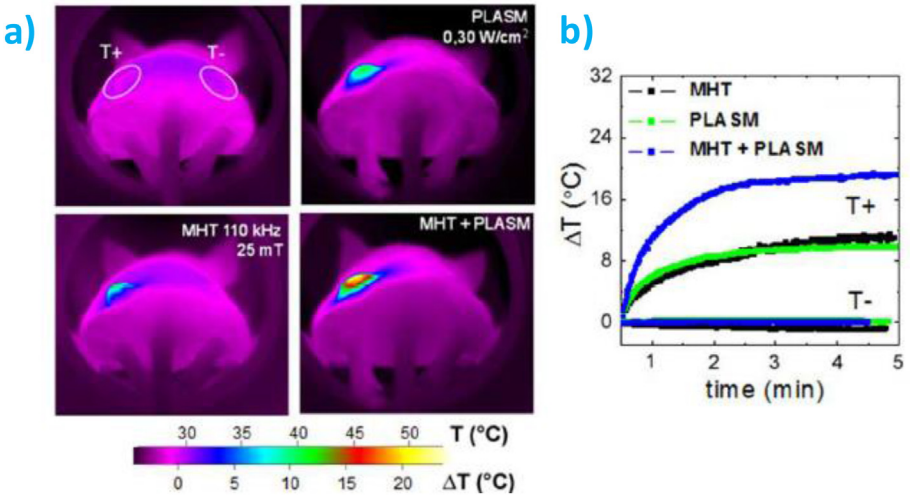

Fig. 10. *In vivo* hyperthermia performance. A solution of [Fe] = 150 mM of 47 nm NPs Mag injected into the tumor (T+). (**a**) Typical infrared thermal imaging pictures after 5 min heating under MHT alone (110 kHz, 25 mT), PTT (PLASM) alone (680 nm, 0.3 W/cm^{+2}), and bimodal MHT + PTT (same parameters). (**b**) Typical temperature elevation profiles of the injected (T+) and non-injected tumors (T-, control tumor) as a function of time for the three treatments. Reproduced with permission from The Royal Society of Chemistry from the study by Li et al. [148]. MHT, magnetic hyperthermia; NP, nanoparticle; PTT, photothermal therapy.

intensities [200]. Several magnetic multicomponent NPs have been synthesized to include them, mainly as core-shell and core-satellites morphologies. Piñol et al. synthesized Fe_2O_3 NPs coated with Eu^{3+} and Tb^{3+} complexes and stabilized by an amphiphilic polymeric shell [201]. The heating of the NP could be monitored by the relative intensities $\Delta = I_{Tb}/I_{Eu}$ achieving a maximum sensibility of 5.8%·K^{-1} at 296 K. MNPs have also been coated with luminescent inorganic materials to achieve higher stability. Some examples are Fe_3O_4@SiO_2@YVO_4:Eu^{3+} [202], $Zn_xMn_{1-x}Fe_2O_4$@SiO_2:$_zNd^{3+}$ [203].

4.1.3. Drug delivery

The development of new cancer therapies has been one of the main focuses of medical nanotechnology in recent years. The design of new therapeutic strategies that are much more efficient, reducing side-effects associated with traditional therapies, such as surgery, chemotherapy, and radiotherapy, and achieving superior outcomes, is the goal of current research [204]. In this sense, targeted and guided drug delivery is one of the most promising alternative therapies, consisting in loading drugs inside different nanostructures that act as carriers that release them in a controlled manner in the region where the therapeutic effect is required. It is clear that magnetic multicomponent NPs appear as a very interesting platform for realizing this application since they can be directed towards the target region, where the drug is to be released. In particular, SPIONs are particularly useful, since their superparamagnetic behavior prevents them from aggregating and are highly biocompatible. As the main drawback, they lack high loading capability in comparison with organic nanostructures, and the attachment of drugs at their surface can compromise their stability in the case or hydrophobic compounds. In this sense, the use of MMNPs with empty interior regions can solve these problems and offer additional advantageous functionalities coming from the different used materials and, at the same time, offer more functionality apart from drug carrying [205,206].

Different nanostructures have been proposed to act as drug delivery systems. One of those structures is that with vesicle morphology, where polymersomes, as seen in Section 3.6, present high stability, and ease of incorporation of inorganic NPs in the shell layer [207]. These vesicles can be loaded with magnetic NPs as well as with different drugs in order to achieve a targeted release of the treatment. DOX-loaded magnetic polymersomes have been reported as theranostic agents for imaging and chemotherapy [208]. Two important parameters should be considered for drug delivery applications. One of them is the *Feed Weight Ratio* (FWR), defined as:

$$FWR = \frac{mass\ of\ engaged\ drug}{mass\ of\ carrier} \times 100 \quad (3)$$

and the other is the *Loading Content* (LC), defined as:

$$LC = \frac{mass\ of\ encapsulated\ drug}{mass\ of\ carrier} \times 100 \quad (4)$$

In this work, hydrophobically modified maghemite (γ-Fe_2O_3) NPs were encapsulated within the membrane of PTMC-*b*-PGA block copolymer vesicles using a nanoprecipitation process. They were embedded together with the efficient antitumor drug DOX into the membrane by one-step nanoprecipitation. The incorporated maghemite SPIONs, with a radius of 4.7 nm, were used to generate heat, producing a relatively small SLP value of 0.07 W/g (at f = 500 kHz and H = 2.12 kA/m). On the other hand, the size of the vesicles was controlled by the water flow rate that triggered self-assembly. An almost instantaneous addition (5 s) led to small vesicles with a hydrodynamic radius of 45–67 nm while a slower addition (15 min) gave rise to 187–202 nm vesicles (Fig. 11a). The maximum FWR was 70 wt% and 50 wt%, respectively. The authors attributed the larger loading capacity of the smaller vesicles to a much faster kinetics of formation, which minimized the probability of SPIONs' clustering before the completion of co-assembly with the copolymer. Dual loading with SPIONs and DOX was performed by nanoprecipitation at pH 10.5, which maximized the loading content to 34%. The authors studied the dynamics of DOX release upon the application of the AMF, observing that the DOX release content was multiplied by a factor of 2 under the MHT compared to the vesicles in normal conditions (Fig. 11b). The authors attributed this increase in release to the moderate heat produced by the SPIONs *via* Néel relaxation, which could increase the fluidity of the semicrystalline polymeric membrane, dramatically increasing the diffusion of the DOX out of the membrane. The same group also demonstrated the applicability of the system in an *in vitro* scenario

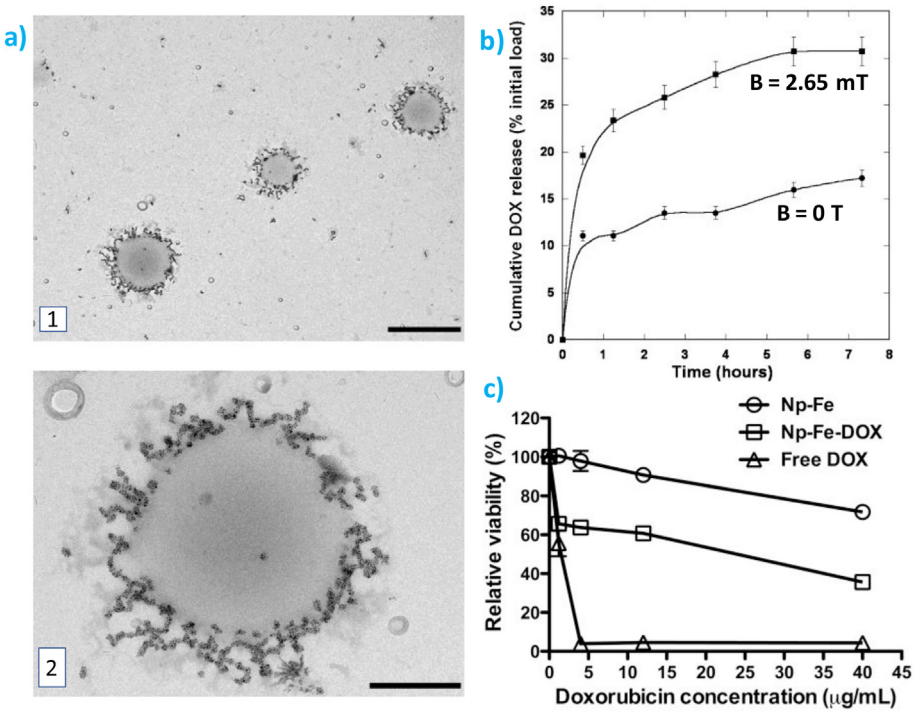

Fig. 11. (**a**) (1) TEM image of large polymersomes (scale bar 1 μm). (2) Close-up view of the vesicle containing approximately 1500 SPIONs measured by image analysis (scale bar 300 nm); (**b**) influence of AMF on the *in vitro* release kinetics at constant temperature of 23 °C (• indicates B = 0T and ■ AC magnetic field (f = 500 kHz, B_0 = 2.65 mT)) [208]. Copyright 2017 American Chemical Society. (**c**) Relative viability of HeLa cells at 72 h post-exposure to SPION loaded polymersomes (Np−Fe), SPION and DOX-loaded polymersomes (Np-Fe-DOX) and free DOX for different doxorubicin concentrations. Reproduced with permission of Elsevier from the study by Oliveira et al. [153]. AMF, alternating magnetic field; DOX, doxorubicin; SPION, superparamagnetic iron oxide nanoparticle; TEM, transmission electron microscopy.

with Human cervical carcinoma (HeLa) cells [153]. They loaded the polymersomes with different drug concentrations and compared the results with the free DOX. As expected, the encapsulation of DOX decreased cell toxicity significantly, supporting polymersome stability and the slow drug release rate (Fig. 11c).

One of the main problems faced by therapeutic agents in cancer treatment is tumor penetration, which prevents efficient drug delivery and therapeutics. In trying to overcome this problem, Bhana et al. prepared a new type of dual magnetic/plasmonic structures that combined PTT and photodynamic therapy in one platform described as Au nanopopcorns (NPCs) containing self-assembled iron oxide cluster (IOC) as the magnetic core [209]. In this case, a photosensitizer acting as a predrug was loaded in the MMNPs. Although this is not technically a drug, the photodynamic therapy taking place on the photosensitizer generates highly reactive species that can have a drug-like activity that chemically acts on the tumor tissue. The synthesis of these NPs started with poly ethylenimine (PEI)-coated IOCs that were further coated with a layer of negatively charged polymer to reverse the surface charge for the subsequent growth of a popcorn-shaped Au layer. The photosensitizer, silicon 2,3-naphthalocyannie dihydroxide (SiNC), was then loaded into the NPs. Finally, the NPs were stabilized with a PEG linker (MUA-PEG) to form MUA-PEG/SiNC/IOC-Au NPCs (Fig. 12a). The SiNC release property was studied under a cellular environment, with incubated SK-BR-3 cells in a medium containing the MUA-PEG/SiNC/IOC-Au NPCs. The results showed a biphasic drug release, with a fast liberation in the first 2 h and a slow increase to 78% released after 5 h. Furthermore, thanks to the magnetic component of the NPs and the ability to concentrate them in the cell environment, the amount of SiNC released increased significantly, from 37% to 52%, after 30 min of incubation. The addition of the plasmonic part added the hyperthermia capabilities for combined synergistic therapy, generating heat with 62% energy conversion efficiency.

Lastly, mesoporous silica ($mSiO_2$) NPs are another nanostructures that have attracted much attention in the field of drug delivery since they can respond to different stimuli (temperature, redox, light, pH or magnetic fields) and can be functionalized with several kinds of capping agents, including NPs and other coatings that change their conformation upon environmental changes [109]. Taking advantage of these stimuli-responsive characteristics is essential to reduce side toxicity and enhance the therapeutic effect, acting as an important tool to improve traditional chemotherapy. In particular, magnetic fields can act as a non-invasive stimulus and possess high penetration in tissues. Guisasola et *al.* embedded SPIONs in a mesoporous silica matrix, thereafter coating the external silica surface with a thermosensitive polymer shell which acted as a gatekeeper of chemotherapeutic drugs trapped in the pore network [210]. The polymer shell, formed with *N*-isopropylacrylamide, *N*-(hydroxymethyl)acrylamide, and *N,N′*-methylenebis(acrylamide), was designed to have a lower critical solution temperature of 42 °C. Hence, above this temperature the polymer suffers a collapse, creating gaps in its structure and allowing the drug release. The complexes were loaded with DOX and introduced via direct injection in tumor-bearing mice, the selected tumor model being C57/BL6. The tumor volume was evaluated after the last hyperthermia treatment (day 3) and 48 h after it (day 5). As shown in Fig. 12b, the tumor volume of all the controls was doubled from day 3 to day 5, whereas the tumor growth in the group with the complete treatment was inhibited. The therapeutic effect demonstrates that the heating effect of the nanocarrier under the AMF overcomes the heat dissipation, causing the lower critical solution temperature of the polymer and thus the release of the DOX.

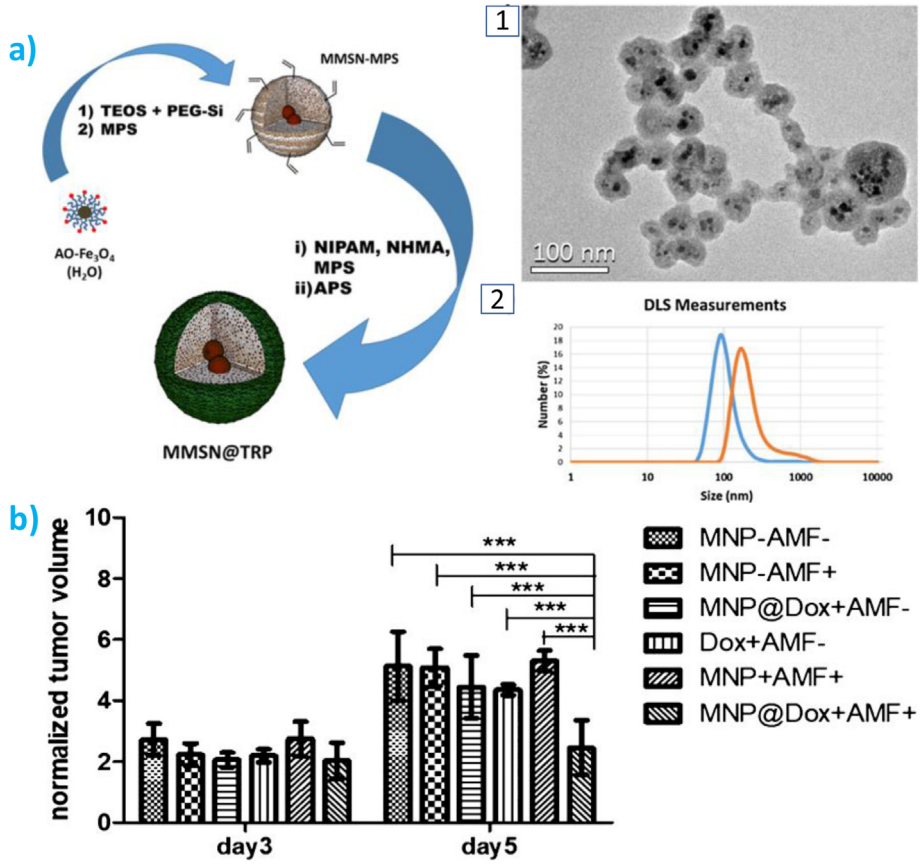

Fig. 12. (**a**) Scheme of the synthetic route of MMSN@TRP. (1) TEM image of the nanocarriers coated with TRP and SPIONs placed inside the silica matrix and (2) hydrodynamic size of the precursor (MMSN-MPS, blue line) and the final nanocarrier (MMSN@TRP, orange line). (**b**) Tumor growth calculated as the ratio between the tumor volume and the initial volume. Day 3 corresponds to the measurements after the last hyperthermia treatment. Day 5 corresponds to 48 h after the last treatment [210]. Copyright 2017 American Chemical Society. SPION, superparamagnetic iron oxide nanoparticle.

4.2. Sensing

4.2.1. Electrode-based sensors

NP-based sensors are gaining increased attention in a wide range of applications in analytical and sensing science. Some of their properties are rapid performance, low-cost, ability to work at room temperature, portability, ease of operation, as well as the ability to generate wireless control, high sensitivity, and selectivity [211]. With the use of MNPs, processes such as the separation and removal processes, alignment at surfaces and interfaces, attachment to monitoring electrodes, and easily modifiable platforms for growing new active layers are possible [212]. The combination with other materials makes them more specific to certain analytes while adding extra functionalities such as optical or conductive response. All of these characteristic advantages make them ideal for quick diagnosis and analysis to maintain public safety [213]. The combination of MMNPs with sensing electrodes has given rise to very novel methods of detection with higher flexibility and low limits of detection. Here, we describe some examples of their use in the sensing of different analytes, including biomedical sensors for viruses, bacteria or health-related substances detection, organic pollutants, and heavy metals.

As evidenced nowadays, the development of accurate and quick sensors for virus detection is essential to limit its propagation, thus reducing the risk of it becoming pandemic and the consequent economic impact they might have [214]. Their detection and quantification by electrode-based sensors was achieved through associated AuNPs, which are commonly used as a detectable label to amplify electrochemical signals due to their outstanding optical and electrical properties. Recently, detection systems based on MMNPs containing iron oxide as the magnetic component have been explored. The use of these magnetic systems helps in the cleaning and purification steps, orientating the NPs to a convenient direction, and stacking the AuNPs onto the electrode. Combining the magnetic and conductive character in MMNP systems, through different structures, enhances the selectivity of the sensors and makes sample processing easier.

Lee et al. developed an Au/iron-oxide magnetic NP-decorated carbon nanotubes (CNT) (Au/MNP-CNT) for influenza and norovirus-DNA sensing channels. Iron oxide magnetic NPs were synthesized and functionalized with gallic acid monohydrate (GA) and used as a reduction agent to form Au NPs from Au^{3+} ions over the CNT surface. In addition, benzene groups in GA attached the IONPs to the surface of CNTs through π-π interactions. Fig. 13a shows a scheme of the MMNP. TEM images showed sizes of Au NPs varying from 20 nm to 200 nm, whereas GA-MNP size was around 12 nm. The Au/MNP-CNTs were aligned and deposited on a planar Pt-interdigitated electrode (Pt-IDE) by an external magnetic field as can be seen in Fig. 13a. In a previous study of the same group, Au/MNP-graphenes (GRPs) with a similar design were employed to detect norovirus-like particles, a virus that causes gastroenteritis symptoms [215]. In that case, multicomponent GRPs were magnetically stacked, instead of directly aligned on the Pt-IDE. As a result, the electron passway of multicomponent CNT on the electrode was shorter than that of the MMNP GRP. A DNA probe was modified with −SH groups in order to attach it to the surface of Au

NPs through thiol chemistry that behaves as an influenza virus or norovirus DNA sensing channel. By using a potentiometer, the sensor measures the change in electrical resistance through I–V curves, depending on the hybridization between the DNA probe and a tDNA on the Au/MNP-CNT surface. In both cases, excellent tDNA selectivity performance was obtained, displaying limits of detections of 8.4 pM and 8.8 pM for influenza virus DNA and norovirus DNA, respectively. This sensor system, with the specific probe and surface modification, could be a universal detection system for different types of DNA [216].

However, the most pursued strategy in virus and pathogen detection is the employment of sandwich-type MMNPs, where a pair of receptors bound to different sites of the same target analyte is used [217]. This method was followed by Sayhi et al. in the development of an electrochemical-based immunoassay combining modified Fe_3O_4 MNPs for immunomagnetic separation of anti-M2 antibody with Au NPs used for both catalytic activities and sensitive detection of influenza A virus, using an immobilization-free carbon microelectrode. Fetuin A-modified AuNPs were conjugated with the magnetic-virus to form the AuNP–fetuin–virus–M2–MNP sandwich complexes. All the process is represented in Fig. 13b. Once the complex was formed, it was magnetically separated from the solution and re-rinsed. Before the analytical measurements, the complexes were destroyed by using an HCl acid solution and sonication. Thus, MNPs can be magnetically removed from the solution containing the AuNPs. These mixtures were deposited on the surface of screen-printed carbon electrodes, which were used for chronoamperometric measurements in the catalytic reduction of protons to hydrogen. A potential difference of + 1.35 V for 1 min and of − 1.00 V for 100 s was applied and the generated current was recorded and was considered as the analytical signal for the influenza virus detection as hydrogen ion reduction is clearly dependent on the concentration of AuNPs solution deposited on the surface of the screen-printed carbon electrodes. The cathodic current decreases as the virus concentration increase in the range of 8–128 hemagglutinin units (HAU) (defined as the amount of virus needed to agglutinate an equal volume of standardized avian red blood cells). A limit of detection (LOD) of more than 8 HAU was achieved. Although the LOD is almost higher than other reported immunosensors [218–220], the process simplicity and short detection time (160 s) of this method are remarkably better [221].

In a similar sandwich-type MMNP, an attomolar sensitive electrochemical genosensor was developed for the detection and quantification of cauliflower mosaic virus 35S (CaMV35S) gene, encouraged by its common use in genetically modified organism (GMO) inserts and the potential common toxic effects that they may cause some genetically modified (GM) foods [222]. On the one hand, a core@shell Fe_3O_4–Au@Ag nanocomposite (Complex 1) was biofunctionalized with a thiol-modified DNA signal probe (sDNA), where MNPs had double functionality in separation and catalytic processes [223]. On the other hand, AuNPs and a carboxylated MWCNTs-modified glassy carbon electrode (AuNPs/cMWCNTs/GCE), here named as Complex 2, was subsequently biofunctionalized with thiolated complementary DNA (cDNA/AuNPs/cMWCNTs/GCE). Finally, the genosensor was obtained after conjugates a CaMV35S target DNA (tDNA), from genetically modified tomatoes, with the modified electrode and magnetic nanocomposite, obtaining complex 1/sDNA/tDNA/cDNA/Complex 2. The whole synthesis procedure is schematically represented in Fig. 13c. They analyzed the electrochemical catalytic activity in the reduction of H_2O_2 by differential pulse voltammetry (DPV) measurements, as the synthesized NPs present peroxidase-like activity. In Fig. 13c, insert DPV curves are represented obtained on different electrodes in N_2-saturated phosphate-buffered saline (0.1 M, pH 7.4) containing 20 mM H_2O_2. The DPV response of Complex 1 sDNA

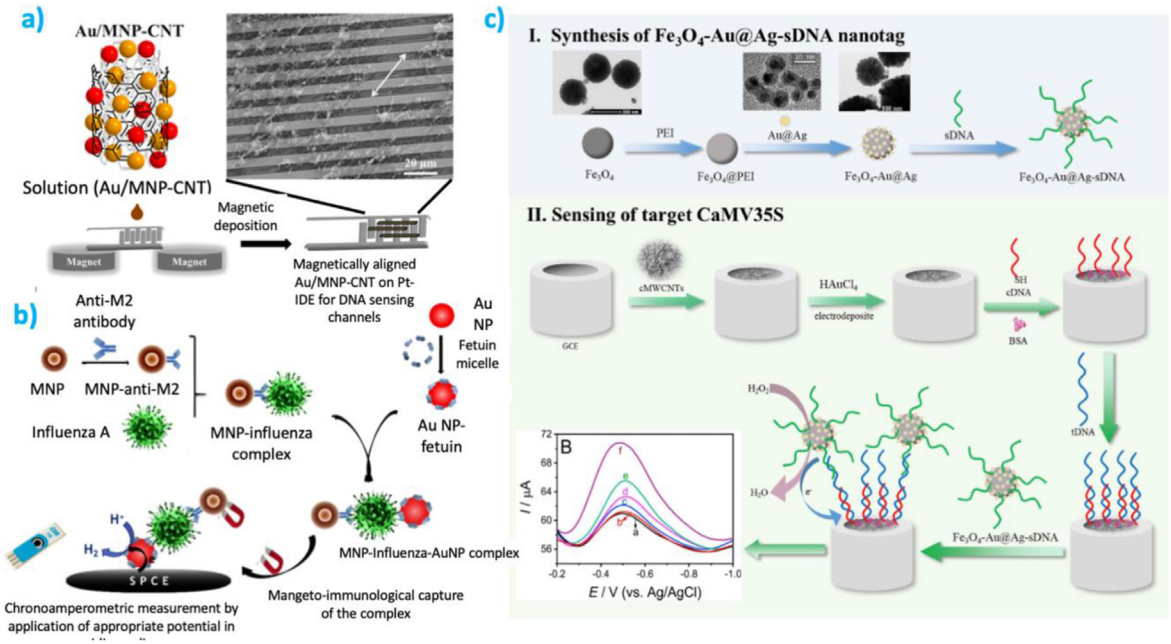

Fig. 13. (**a**) Illustration of the synthesized Au/MNP-CNTs, preparation of the magnetically aligned NPs on the Pt-IDE for DNA sensing channels, and a SEM micrograph of the whole system. Reproduced with permission of Elsevier from the study by Lee et al. [216]. (**b**) Schematic illustration of the strategy used to develop the Au NP-based chronoamperometric magneto-immunosensor for influenza virus. Reproduced with permission of Elsevier from the study by Sayhi et al. [221]. (**c**) Diagram of the fabrication and detection procedures of the genosensor with an inserted graph of DPV curves obtained on different electrode in N_2-saturated PBS (0.1 M, pH 7.4) containing 20 mM H_2O_2. *a:* blank control, *b:* DNA conjugates/Complex 2, *c*: Fe_3O_4- DNA conjugates/Complex 2, *d*: Au- DNA conjugates/Complex 2, *e*: Au@Ag- DNA conjugates/Complex 2, and *f*: Complex 1/DNA conjugates/Complex 2. The concentration of tDNA was 100 pM. Reproduced with permission of Elsevier from the study by Ye et al. [224]. CNT, carbon nanotube; DPV, differential pulse voltammetry; PBS, phosphate-buffered saline; SEM, scanning electron microscopy; tDNA, target DNA.

probe was the highest of all the different signal probes tested, where a synergistic effect in the catalysis process was observed between Fe_3O_4 NPs and Au@Ag NPs. The sensor showed an ultralow LOD of 1.26×10^{-17} M and a linear range of $1 \times 10^{-16} - 1 \times 10^{-10}$ M. They also achieved excellent selectivity, stability, and reproducibility with good performance in real samples of transgenic tomatoes [224].

Bacteria represent the second type of pathogen where MMNPs can offer a rapid and efficient sensing capability. The same strategy, as described above, has been employed for the detection of different bacteria. A sandwich immunosensor based on dual-aptamer for the detection of *Staphylococcus aureus* (*S. aureus*) was proposed. Aptamers functions are similar to antigen-antibody interactions; they are single-stranded oligonucleotides (typically DNA or RNA) or peptides with high affinity and specificity with their targets [225]. In that case, a biotinylated anti-*S.aureus* aptamer was immobilized on streptavidin-coated magnetic beads suspension. Then, a sample of *S. aureus* was added, where the aptamer captures the bacterium. Finally, Ag NPs conjugated with a secondary thiolated anti-S.aureus aptamer (Apt-AgNP) was added to complete the sandwich. The complex (MBeads/Apt/S.aureus/Apt-AgNPs) was magnetically separated and resuspended in a HNO_3 solution to fully dissolve AgNPs. Again, the magnetic part of the complex was removed and the remaining Ag^+ ions were measured by differential pulse anodic stripping voltammetry since the Ag^+ ions concentration was directly proportional to *S. aureus* concentration in the sample. They obtained a good LOD of 1.0 cfu/mL and an ample linear range of $10-10^6$ cfu/mL. Further, the results of the analysis of real water samples were comparable to those obtained by the plate counting method. The simplicity, reduced measuring time, low cost, and high sensitivity are some advantages of this biosensor compared with conventional methods [226].

Analogously, some researchers have developed a new bacteria sensor based on currently existing point-of-care (POC) electrochemical devices using MMNPs as high selective platforms. Jun Bu et al. introduced an electrochemical sensor for *Escherichia coli* O157:H7 (*E. coli* O157: H7) quantification that employs a hand-held hydrogen detector as the transducer. They applied a sandwich-type MMNPs of magnetic beads attached to a peptide−$Cu_3(PO_4)_2$ with embedded PtNPs to catalyze the dehydrogenation of ammonia−borane and generate H_2. The synthesis and analytical process are schematically represented in Fig. 14a. The LOD of that (POC) immunosensor was 10 CFU/mL in a linear range from 10 to 10^4 CFU/mL [227]. Likewise, Bai et al. made use of a personal glucose meter as signal readout in the detection of *E. coli* O157: H7. On the one hand, a sandwich-type MMNPs of Fe_3O_4 embedded magainins I−$Cu_3(PO_4)_2$ flower-like nanocomposites was synthesized, for the magnetic capturing of the bacteria. On the other hand, they also prepared an invertase embedded cecropin P1−$Ca_3(PO_4)_2$ flower-like nanocomposite (PIPs), to be used as "detection" framework. The combination of both complexes is represented in Fig. 14b. In that work, they employed magainins I, and cecropin P1 antimicrobial peptides (AMPs), that display high affinities and specificities for bacterial cells, instead of using aptamers or antibodies for the biorecognition of *E. coli* O157: H7. Finally, the invertase enzyme in the complex hydrolyzes sucrose to glucose. Under optimal conditions, an extended linear range of $10-10^7$ CFU/mL with a LOD of 10 CFU/mL was calculated. Furthermore, comparable results were obtained from spiked milk samples [228].

Apart from pathogens, MMNPs have also been studied in the development of protein quantification systems that help in the diagnosis of several health disorders. A MMNP with a sandwich-like nanostructure was presented for the detection of human platelet-derived growth factor (PDGF) protein (an indicator of tumor angiogenesis [229]) in a homogeneous solution without the need for separation. The proposed MMNP was composed of a yolk-shell-like silica core with Fe_3O_4 NPs shell and a continuous polydopamine (PDA)-Au coating. Then, 4-mercaptophenylboronic acid was assembled onto the surface of the SiO_2@Fe_3O_4@PDA@Au yolk-shell-like composite, for the immobilization and enrichment of PDGF. On the other hand, a signal probe of aptamer-SiO_2- methylene blue (MB) nanostructure was synthesized and used to specifically bind with PDGF. The sandwich-like sensor final conjugate, after all the selective binds, results in yolk-shell-like composite/PDGF/aptamer-SiO_2-MB. This conjugate is collected on the surface of the GCE with an external magnetic field behind the electrode. Fig. 15a shows a scheme of the synthesized NPs and the employed sensor. DPV measurements were performed, resulting in an analytical signal due to the reduction of MB. The developed biosensor LOD was determined to be 0.22 fM. This method has the potential for developing an ultrasensitive quantitative analysis of PDGF-BB or other glycoproteins in complex samples [230].

Aside from using sandwich structures, that usually allows the detection of a single substance, electrochemical sensors are also capable of quantifying different substances simultaneously. Cincatto et al. designed a novel nano-magnetic electrochemical sensor selective for amitriptyline, melatonin, and tryptophan. The sensor comprises Fe_3O_4 magnetic NPs decorated with carbon quantum dots (MagNPs/Cdots) magnetically held onto a GCE by locating behind a miniature neodymium magnet, as shown in Fig. 15b. Magnetic NPSs of 20 nm were synthesized through the co-precipitation method. Carbon dots were synthesized via the amperometrically controlled electrolysis of a propanol solution and

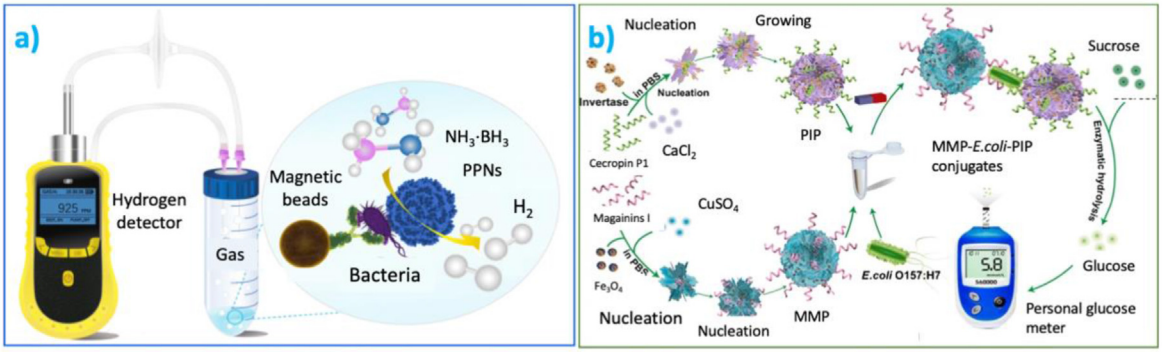

Fig. 14. Schematic representation of the immunosensors for *E. coli* O157:H7 bacteria (**a**) using a H_2 detector as signal readout and (**b**) the synthetic process for antimicrobial peptide-phosphate nanocomposite pair and of the personal glucose meter-based immunoassay. Reproduced with permission of Springer Nature from the study by Bu et al. [227] and Bai et al. [228].

anchored on the surface of MNPs (Fig. 15b). Then, MagNPs/Cdots MMNPs were magnetically confined onto the surface of a GCE. Electrochemical measurements were carried out simultaneously in the oxidation of amitriptyline, melatonin, and tryptophan by DPV, where high selectivity was displayed for the three studied substances compared to potential biological interfering substances such as uric acid, ascorbic acid, dopamine, estriol, and 17β-estradiol, which analytical responses were very low (Fig. 15b). Low detection limits of 5.9 nM, 4.4 nM, and 4.2 nM were obtained for amitriptyline, melatonin, and tryptophan, respectively [231]. In this line, magnetic molecularly imprinted polymers (MMIPs) have been recently developed to determine 17β-estradiol. MMIP consists of core@shell NPs of Fe_3O_4@SiO_2 coated with a polymer of methacrylamide crosslinked with ethylene glycol dimethacrylate. MMIP absorbs 17β-estradiol and is immobilized magnetically on the surface of a carbon paste-based electrode. The measurements were carried out by differential pulse adsorptive stripping voltammetry, performing a low LOD of 0.02 μmol/L. It presented comparable results to those obtained by high-performance liquid chromatography for samples of river water and raw milk [232]. These sensors open new possibilities to develop low-cost, rapid, disposable, and portable medical sensors for mood disorders and reproductive-related substances.

Some electrochemical sensors have focused on non-degradable industrial pollutants, such as heavy metal ions, which can cause many diseases and have been a matter of concern during decades as a global problem [233]. Miao et al. proposed an electrochemical sensor for simultaneous determination of Ag^+ and Hg^{2+}, based on DNA probes, labeled with ferrocene (Fc) and MB, modified Fe_3O_4@Au NPs and magnetic GCE. The synthesis process is shown in Fig. 15c. High selectivity is achieved in the recognition of Ag^+ and Hg^{2+} due to strong bindings with DNA duplexes C–C and T–T mismatches, respectively. The other two DNA probes labeled with Fc and MB are designed to contain mismatched sites with DNA 1 probe, and the hybridization events occur on the basis of C– Ag^+ –C and T– Hg^{2+} –T coordination chemistry. Due to the magnetic property of the electrode, the modified Fe_3O_4@Au NPs can be easily immobilized on the electrode surface in just 2 min, making the solution transparent. Afterward, the electrochemical species can be detected by square wave voltammetry to represent corresponding target heavy metal ions as is shown in Fig. 15c. A significant current peak (Fc) at 0.36 V appears in the presence of Ag+, and the current peak (MB) at −0.39 V emerges in the presence of Hg^{2+}. Both of the two discrete current peaks can be observed simultaneously in the detection of Ag^+ and Hg^{2+}. The LOD for Ag^+ assay is found at 3.4 nM (about 0.37 ppb) and as low as 1.7 nM (about 0.34 ppb) for Hg^{2+}, meeting the USEPA (United States Environmental Protection Agency) guidelines. The amplification-free feature of this method also makes it less time-consuming compared with other sensitive methods, which involve signal amplifications. The signals for Ag^+ and Hg^{2+} are independent, and no interferences were observed, even with other metal ions in the sample [234].

4.2.2. SERS-based sensors

SERS has proven to be an extraordinary tool for ultrasensitive detection in field-based or POC applications and is a clear example of the extraordinary potential of MNPs. Raman spectroscopy is a characterization technique that offers structural information of molecules. It allows high discrimination of molecules, and the possibility of measuring in aqueous samples (as opposed to IR spectroscopy). However, Raman is a quite inefficient process, with only 1 out of 10^6-10^8 scattered photons being a Raman photon. SERS highly increases the efficiency, converting Raman in a sensing technique for low and ultra-low concentration analyses. SERS is based on the electromagnetic field enhancement that takes place at the surface of metal NPs and rough metal surfaces, *i.e.* plasmonic

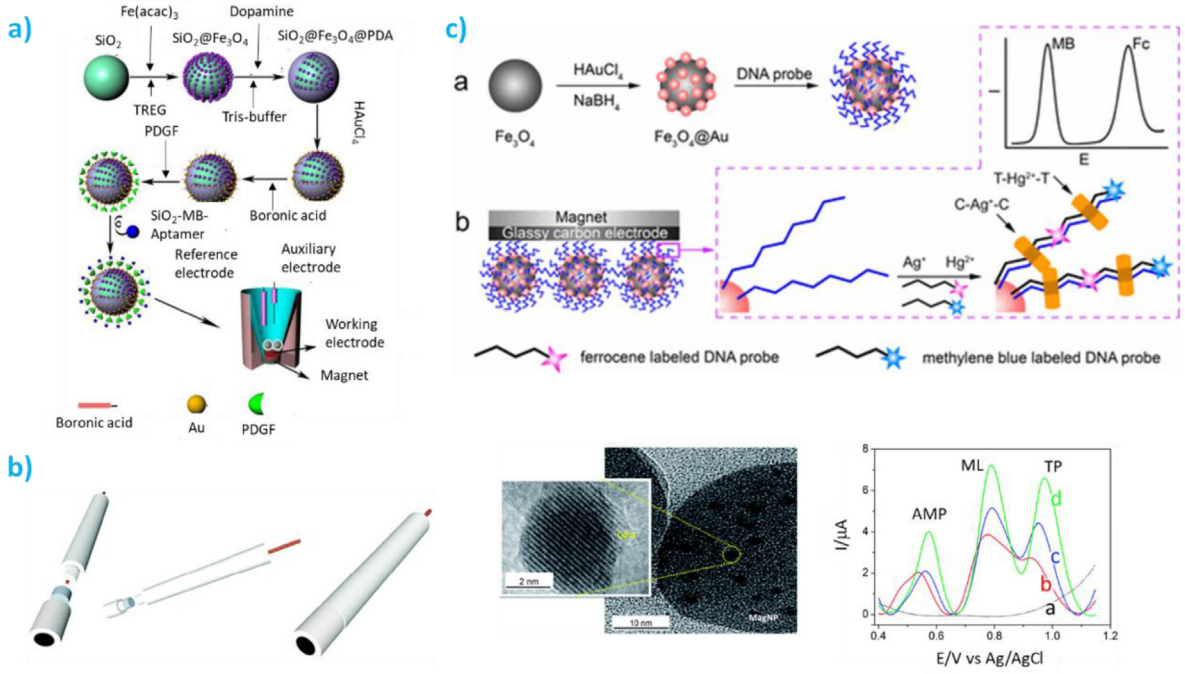

Fig. 15. (**a**) Schematic representation for the configuration of the biosensor for PDGF. Reproduced with permission of Elsevier from the study by Guardia et al. [177]. (**b**) Architectural illustration of the working electrode, showing a disk-shaped miniature neodymium magnet (grey) behind the glassy carbon (left), a HRTEM micrograph of MagNPs/Cdots with an amplified inset of Cdots (middle) and DPV voltammograms obtained under optimized conditions for a: GC/MagNPs/Cdots blank solution; b: bare GC; c: GC/MagNPs and d: GC/MagNPs/Cdots composite (right) [231]. (**c**) a: schematic diagram of DNA-modified Fe_3O_4@Au NPs synthesis; b: schematic diagram of the procedure used for simultaneous detection of Ag+ and Hg^{2+} [234]. Copyright 2017 American Chemical Society. DPV, differential pulse voltammetry; HRTEM, high-resolution transmission electron microscopy; PGDF, platelet-derived growth factor.

materials [235–238]. Analytes at those surfaces experience an enhancement of the electromagnetic field E_{loc}/E_0 from one to three orders of magnitude, which is translated into an electromagnetic enhancement factor EF = $I_{SERS}/I_{Raman} \approx (E_{loc}/E_0)^4$ of 10^4 to 10^{12}, which can be further increased by a chemical enhancement [239]. Engineering NPs for exhibiting high local electromagnetic enhancement regions, also known as hotspots, is crucial to improve the enhancement and therefore to decrease the LOD [236]. These hotspots appear at the tips of elongated morphologies, sharp edges, and corners, known as intrinsic hotsposts, or at the junctions between NPs when they are placed at very close distances (below 10 nm), known as extrinsic hotspots.

Despite the high potential of SERS, its practical use still encounters several challenges, such as the requirement of affinity of analytes to the surface, the interferences from the complex matrix of real samples, the limited concentration/enrichment effect of the substrate for target or the SERS substrate fabrication, or the reproducibility in the fabrication of SERS substrates. The unique properties of multicomponent MNPs may provide efficient solutions to some of these challenges [240,241]. By manipulating magnetic force, it is possible to easily and rapidly separate analytes from a sample matrix to reduce the interference; generate an enrichment of the sample for ultra-low concentration detection; form a controllable aggregation of substrates, which can generate a favorable extrinsic hotspot for further enhancement.

With these advantages in mind, several types of MNPs have been synthesized for the detection of low concentration of sensitive analytes. Commonly, the MMNPs for these tasks are made of iron oxide (Fe_3O_4 and γ-Fe_2O_3) as magnetic material and Au and Ag as the plasmonic metal with a LSPR from the visible to the near IR by varying its shape. Ag is in general better plasmonic material for SERS due to its lower attenuation in the visible region (lower imaginary part of the dielectric function) but, differently than Au, it is prone to oxidation. Therefore, a rational choice depending on the application is required.

Among the different morphologies, there are core@shell, core-satellite, and non-spherical morphologies. Core@shell morphologies offer the advantage of the shell protection to the magnetic core. These structures although they do not have intrinsic hotspots, highly benefit from the magnetic core for controlled aggregation and therefore creation of extrinsic hotspots. Furthermore, the LSPR offers high tunability through the selection of the shell thickness what allows their adaptation to the desired incident laser wavelength of the Raman instrument [242–244]. Core@shell structured such as Fe_3O_4@Au and Fe_3O_4@Ag, have been broadly used as versatile SERS substrates [245–253]. A combination of Au and Ag has shown to produce beneficial characteristics, such as a better tuning of the plasmon band [254], and a general improvement of the EF. Han et al. showed that in Fe_2O_3@Au@Ag structures the addition of the Ag layer produced a much higher signal enhancement than the initial Fe_2O_3@Au. Interestingly, the highest enhancement was obtained for partially Ag-coated NPs presenting small cavities, or pinholes, that could add further plasmon resonances [255]. Further development in the multi-shell structure with intermediate dielectric materials can produce new LSPR modes that can be exploited for a higher EF [242,256,257]. Fe_3O_4@Ag@SiO_2@Au particles displaying long-range plasmon transfer of Ag to Au were also synthesized. The particles presented higher protection due to their external Au layer, and an EF of 2.2×10^4, superior to the 0.67×10^4 Fe_3O_4@Ag NPs and attributed to the new transfer plasmonic modes (Fig. 16) [258].

Core–satellite magnetic NPs have obtained increasing interests as attractive SERS substrates. They present multiple hotspots generated at the gap between adjacent satellite plasmonic NPs exhibiting a high-intensity electromagnetic enhancement that is added to the extrinsic hotspots formed when the NPs magnetically aggregate [120–122,259–266]. Fig. 17a shows the formed hotspots among the different plasmonic surrounding NPs, *i.e.* satellites, as well as the ones formed between two adjacent core-satellite NPs [261]. With this configuration, EFs of 10^5-10^7 have been obtained. The hotspot formation will be dependent on many parameters, including the material, the size, and the gap between the satellites, as well as the packing between different NPs. Several of those parameters are connected and can be easily controlled during the

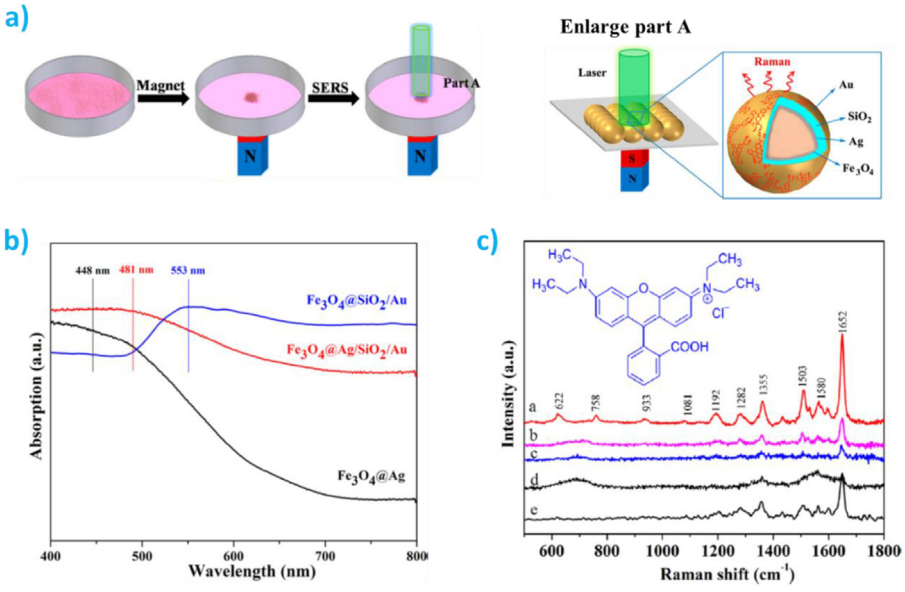

Fig. 16. (**a**) Schematic illustration of magnetic enrichment and in situ SERS detection by Fe_3O_4@Ag/SiO_2/Au microspheres. (**b**) Comparative UV–Vis spectra of Fe_3O_4@Ag, Fe_3O_4@SiO_2/Au, and Fe_3O_4@Ag/SiO_2/Au microspheres. (**c**) Raman and SERS spectra of Rhodamine B (RhB). *a*: Raman of 0.2 M in aqueous solution. *b-e*: SERS spectra of 1×10^{-6} M on *b:* Fe_3O_4@Ag microspheres, *c*: Fe_3O_4@Ag/SiO_2 microspheres, *d*: Fe_3O_4@SiO_2/Au microspheres, and *e*: Fe_3O_4@Ag/SiO_2/Au microspheres (785 nm laser excitation) [258]. Copyright 2017 American Chemical Society. SERS, surface-enhanced Raman scattering; UV, ultraviolet.

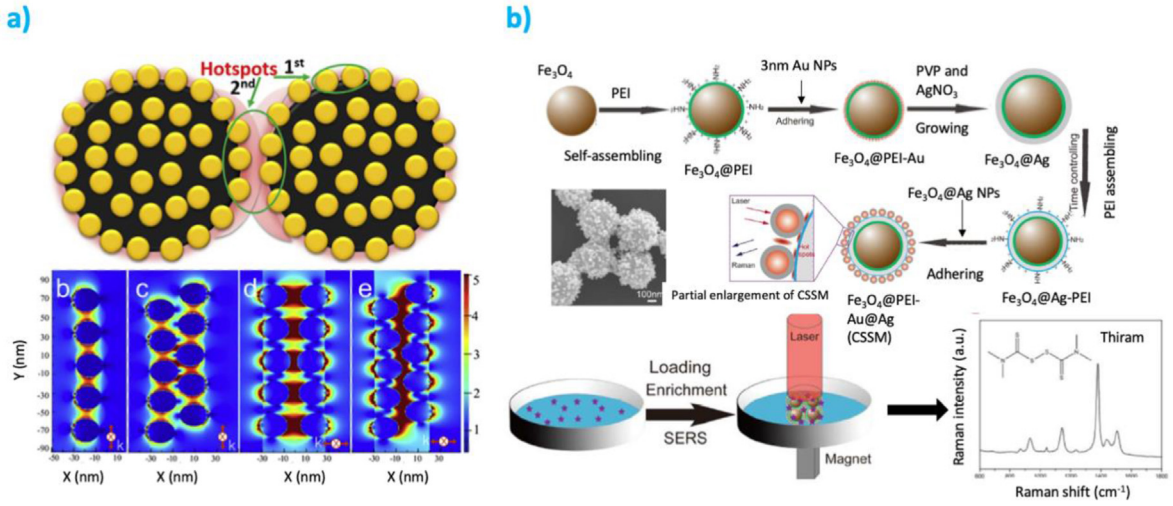

Fig. 17. (**a**) Schematic representation of the two types of plasmonic hotspots formed on Fe_3O_4@Au NPs. Calculated electromagnetic enhancement with 785 nm excitation. Adapted from the study by Du et al. [261]. (**b**) Synthesis procedure of Fe_3O_4@Ag/PEI/Au@Ag core–shell–satellite particles, and approach for the detection of Thripan. Adapted from the study by Wang et al. [269] with permission from The Royal Society of Chemistry. NP, nanoparticle; PEI, polyethylenimine.

synthesis. For instance, the average gap between the satellites will depend on their number and their size, *i.e.* on the amount of Ag or Au that is added either in the form of preformed NPs or in the form of the reagent in the growing steps. On the other side, the extrinsic hotspots between adjacent core@shell NPs are less controllable and will be formed by an ensemble of different packing configurations. In the same way that for the case of core@shell NPs adding an intermediate layer may be used to increase the stability, facilitate the assembly of satellites, further enhance the Raman signals, or protect the satellites from aggregation. Examples of these types of NPs are Fe_3O_4–Au@Ag [259], Fe_3O_4@SiO_2–Au [122], Fe_3O_4@Ag/$mSiO_2$/AuNPs [264], Fe_3O_4–Au@TiO_2 [121], Fe_3O_4–Au@SiO_2 [267], or $CoFe_2O_4$@HNTs/AuNPs [268]. Fig. 17b shows the synthesis steps to form core-satellite NPs with an intermediate Ag plasmonic layer and Au satellites with an intermediate PEI layer, as well as their application through a separation/enrichment process [269].

While engineering spherical morphologies may result simpler in many cases, the development of anisotropic shapes offers many other advantages such as intense intrinsic hotposts or tunability of the plasmonic response [236]. Anisotropic NPs having large aspect ratios, sharp tips, and edges present remarkable enhancements at the high curvature regions. Among the different shapes are star-shaped NPs, also called urchin-shaped or flower-like [270–275], Janus nanostar [162], spindle- or needle-like [276], durian-like [277], dumbbell-like [278], or bigger assemblies and composites [279–288].

All mentioned MMNPs allow the application as SERS substrates with the advantages of magnetic NPs, for separation and enrichment. They allow selectivity thorough sample modifications and recovery to avoid unnecessary NP pollution. In many cases, the NPs can be also reused through specific cleaning procedures [272]. Their direct application involves first an incubation time with the analyte in a determined liquid matrix. The nano-size characteristic offers the advantage of low diffusion distances between the analyte and the NPs, and therefore low incubation times. After this time, the NPs are separated and concentrated with the help of a magnet. This process is often called magnetic solid-phase extraction and is the one reflected in Fig. 17a and b. The process can be also improved through adapted syringes with actionable magnets [289] or with the use of microfluidic systems [290]. This last case, together with the new smaller and affordable portable Raman instruments, offers enormous potential for field-based or point of care applications that are affordable and easy to handle by a wider variety of final users.

The direct application, however, is limited to a small number of molecules that are prone to be adsorbed at the surface of the NPs and own a Raman cross-section high enough to be analyzed at the required LOD. Different strategies can be followed to increase the adsorption of the target analytes to the NPs by modifying the surface physicochemical characteristics. Of special relevance are those that produce high selectivity, such as the use of aptamers and antibodies that together with the increased adsorption, decrease the binding of other molecules and therefore reduce the matrix interferences [252]. Similarly, the use of molecularly imprinted polymers [291] and metal-organic-frameworks can be used in search of this selectivity [292]. On the other hand, strategies based on SERS tags can be applied to improve the Raman cross-section and therefore the sensitivity. These tags can be added to a probe molecule that also binds to the analyte, in this way a sandwich structure of NP-analyte-probe can be used for the detection analysis [293]. Alternatively, SERS tags can be bound directly to a plasmonic NP. A sandwich strategy may be used for an analyte binding a magnetic NP and a plasmonic NP containing the SERS tag [294]; moreover, the use of MNPs helps to the formation of hotspots between the MNP and the tag-containing plasmonic NP producing extrinsic hotspots and therefore higher enhancement of the tag molecule Raman signal [295,296].

Given the versatility of SERS, these systems have been applied to a very wide range of sensing applications. For instance, in environmental pollution, they have been used in the detection of several types of organic molecules. Among them are molecules such as polycyclic aromatic hydrocarbons (PAHs) [297], pesticides [298], or pharmaceutical and personal care products [299,300]. SERS has been also used to detect toxic heavy metals including Cr(VI) [249], Hg^{2+} [262], As (III) or As(V) [251].

Together with environmental applications, biomedicine is the other major area of applications in which SERS detection has proven to be a powerful tool. A MM-plasmonic NP may present several simultaneous functions such as diagnosis, drug delivery, and hyperthermal treatment forming a complete multifunctional medical nanodevice. In diagnosis, magnetic SERS has been widely used in the detection of many illnesses that range from malaria

[301] to breast cancer and leukemia [302,303]. Their potential dramatically expands to many other biomedical areas thanks to their ability to easily detect DNA/RNA fragments [250,304] and proteins and antigens [305,306].

Easy detection of pathogens is also of high interest. Their detection in situ applies not only to the above-cited fields of environment and biomedicine but it is also of interest in fields such as food safety. Among the different types of pathogens, where magnetic SERS has been applied, are bacteria such as *E. coli*, *S. aureus*, or *Salmonella typhimurium* [248,307,308]. There are many other areas of research where magnetic SERS is of high interest, including the detection of explosives [309,310], the monitoring of different reactions [121,311,312], or the detection of illegal food additives [281]. The number of applications is continually expanding and certainly will grow with the design of more complex MNPs with new functionalities and higher sensitivity and selectivity.

4.3. Catalysis

4.3.1. Catalysis for the synthesis of compounds

Metal nanoclusters [313], metal NPs [314], and metal oxide NPs [315] have proven to be efficient for catalytic reactions in many synthetic processes. In spite of the good catalytic performance showed by many homogeneous catalysts, heterogeneous catalysts are preferred as they can be easily removed from the reacting medium, allowing product purification and catalyst recyclability [316]. Even in the case of heterogeneous catalysts, the separation process is a complex task as a result of their small size, resulting in inevitable catalyst loss by conventional separation approaches. A solution to simplify catalyst recovery is the development of magnetically separable catalysts [317,318]. To enhance the limited catalytic activity of magnetic catalysts, they are combined with other catalytically active materials such as transition metals, metal oxides, or organic materials such as graphene.

Palladium (Pd) is among the most widely used metal catalyst in modern organic synthesis. For instance, Pd NPs were immobilized onto Fe_3O_4 upon the reduction of Pd^{2+} to obtain new nanocatalyst useful for the aerobic oxidation of alcohols to aldehydes or ketones along with the formation of O_2 and H_2O (Fig. 18a) [319]. Using 0.2 mol% MMNPs, a good activity on the oxidation of primary benzyl alcohol with different substituents was observed, reaching selectivity values above 99% with yields up to 97% for reactions carried out in water at 80 °C during 4 h (17% yield for the poorer catalysts formed by bare Fe_3O_4). This is a worthy area of research because the selective oxidation of alcohols using oxygen as the terminal oxidant is a relevant reaction in organic synthesis [320]. More recently, ~35 nm Pd NPs were stabilized onto Fe_3O_4 for Suzuki-Miyaura C–C cross-coupling reactions, which is a common reaction for the preparation of biaryls compounds used in the pharmaceutical and polymer synthesis fields [321]. The conversion of various aryl halides into the corresponding biaryl derivatives by Suzuki-Miyaura reaction was achieved in only 5 min. Reaction yields of 99% using 10.5×10^{-2} mM of NPs were achieved following a solvent-free process. Remarkably, Pd–Fe_3O_4 outperforms previously reported heterogeneous catalysts in time and yield through a green solvent-free synthesis process.

Apart from the bicomponet examples shown above, tricomponent MMNPs have also been developed for catalysis. In this sense, Au NPs were immobilized onto rose-like Pd–Fe_3O_4 NPs for the tandem synthesis of 2-phenylindoles from 2-iodoanilines with phenylacetylenes, which is rarely found in the literature [322]. A good catalytic activity was achieved due to electron transfer across the interface and avoidance of the stoichiometric transmetalation by-products, which are common effects in cross-coupling reactions. As a consequence, an improved performance relative to previously reported Cu, Au complexes, and Au NPs in terms of turnover frequency value and conversion degree was obtained. In another work, Pd NPs were embedded into C@Fe_3O_4 core@shell nanospheres to produce an efficient catalyst for cyanation to the corresponding nitriles [323]. The cyanation reaction of aryl iodides, bromides, and chlorides with different solvents and bases and $K_4[Fe(CN)_6]$ as a green cyanating agent was evaluated. The effect of Pd morphology (spherical *vs.* cubical) on the catalysis was analyzed, showing that cubical Pd NPs are more reactive as a result of a larger number of {100} surface facets. This work provides useful information to design novel catalysts thanks to the achieved catalytic efficiency, ease of synthesis, high stability, reusability, and magnetic separation ability.

Due to its peculiar properties, graphene oxide (GO) results very useful in diverse catalytic reactions [324]. Unfortunately, GO sheets tend to aggregate, lowering the exposed surface area and thus reducing their catalytic efficiency. This problem was solved by developing sulfonic acid-modified Fe_3O_4@GO MMNPs, which were proven useful as heterogeneous Brønsted acid-based catalysts [325]. Sulfonation and subsequent oxidation steps served to stabilize the NPs, improving the efficiency of the heterocyclic indazolophthalazinetrione synthesis after the coupling of aldehyde, dimedone, and phtalhydrazide (Fig. 18b). Not only GO but also

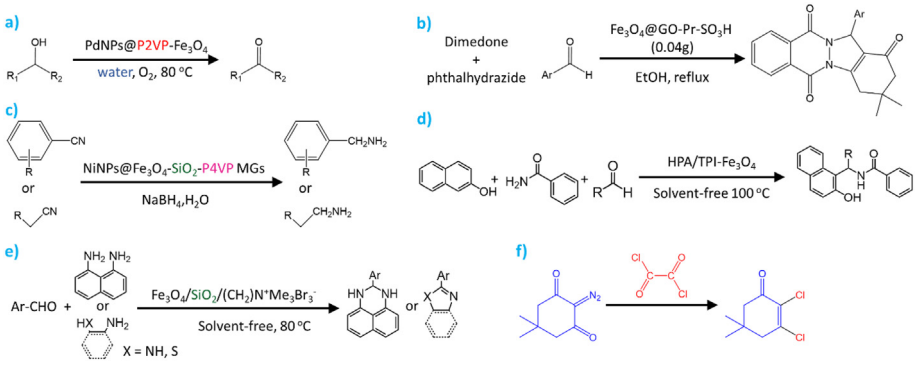

Fig. 18. Examples of catalytic reactions using MMNPs as catalysts: (**a**) Pd@Fe_3O_4 catalysts for aerobic oxidation of alcohols. Reproduced with permission from Springer Nature from the study by Nabid et al. [319]. (**b**) Fe_3O_4@GO for heterocyclic indazolophthalazinetrione formation. Reproduced with permission of Elsevier from the study by Doustkhah and Rostamnia [325]. (**c**) Nitrile reduction with NiNPs@Fe_3O_4–SiO_2–P4VP. Reproduced with permission of John Wiley & Sons Ltd from the study by Nabid et al. [327]. (**d**) 1-amidoalkyl-2-naphthol synthesis with Fe_3O_4–$H_6P_2W_{18}O_{62}$. Reproduced from the study by Tayebee et al. [328] with permission from The Royal Society of Chemistry. (**e**) Synthesis of five- and six-member heterocycles. Reproduced with permission of Elsevier from the study by Farrokhi et al. [329]. (**f**) Cyclic diazodicarbonyl compound synthesis with trimetallic Au–Fe–Ag NPs. Reproduced with permission of Elsevier from the study by Mishra et al. [330]. GO, graphene oxide; MMNP, multicomponent magnetic nanoparticle.

rGO has been used to develop magnetic multicomponent catalysts. 5 nm Fe_3O_4 and Pt NPs were deposited onto rGO to obtain MMNPs useful for the aqueous-phase aerobic oxidation of benzyl alcohol [326]. In spite of the lower electrochemical active surface, the close contact of Fe_3O_4 with Pt active centers enhances the catalytic performance of rGO, improving the turnover frequency (defined as the number of moles of benzyl alcohol converted per mole of active catalyst per hour) and the conversion up to maximum values of 1110 h^{-1} and 33.6%, respectively (430 h^{-1} and 18.6% for Pt/rGO). These MMNP catalysts have great industrial potential as they can easily reduce benzyl alcohol, which is the second most important aromatic molecule after vanillin.

Apart from Pd or graphene, MMNP catalysts based on other materials have been synthesized. In such examples, Fe_3O_4 is generally used as the magnetic substrate. As shown in Fig. 18c, nickel NP encapsulation on Fe_3O_4–SiO_2 (Ni@Fe_3O_4–SiO_2–P4VP) has proven to be an efficient heterogeneous catalyst for nitrile reduction in water [327]. A reduction of 19 different aliphatic and aromatic nitriles to primary amines in refluxing water conditions was obtained with conversion rates above 99% in 2 h (selectivity > 99%), which is usually difficult to achieve as the α hydrogen deprotonation to the nitrile stops the reduction process [331]. Conversion yields for seven consecutive runs did not decrease, which together with their magnetic recovery ability make such NPs robust catalysts for the reduction of many different C–N multiple bonds. Cycloaddition reactions between epoxides and CO_2 to produce cyclic carbonates were facilitated using MMNPs, providing an environmental solution to the presence of CO_2 in the atmosphere as it successfully serves to capture and store CO_2 [332]. Accordingly, SiO_2–Fe_3O_4 MNPs were coated by Cu to reach yields up to 92% after 12 h of reaction at 80 °C under solvent-less and organic halide-free conditions. A pivotal role of Cu was found as it activates CO_2 by 1,8-Diazabicyclo[5.4.0]ndec-7-ene (DBU), enabling the ring-opening step and subsequent cycloaddition reaction.

A magnetically recoverable inorganic-organic multicomponent catalyst was obtained by the anchoring of Wells–Dawson heteropolyacid $H_6P_2W_{18}O_{62}$ onto the surface of modified Fe_3O_4 NPs (Fig. 18d) [328]. A solvent-free and one-pot fabrication of various substituted 1-amidoalkyl-2-naphthols useful for synthetic pharmaceuticals was achieved from the condensation of β-naphthol with 24 different aldehydes (aliphatic and aromatic) and benzamide at 100 °C for 30 min, resulting in yields of 94%. Interestingly, MMNPs showed no loss of activity after 8 cycles, highlighting the potential of these materials for the rapid synthesis of biologically active 1-amidoalkyl-2-naphthols.

Nanocatalysts presenting core@shell morphology show interesting characteristics for magnetic catalyst design. Accordingly, a magnetic Fe_3O_4 core was combined with a porous metal-organic framework shell for biodiesel production [333]. Soybean oil transesterification with methanol in the presence of 1.2 wt% MMNPs resulted in a 92.3% oil conversion to methyl esters after 3 h of reaction at 65 °C. The magnetic nature of the NP solved the complex catalyst recovery and undesirable wastewater yielded in the downstream purification processes often found in homogeneous base-catalyzed transesterification processes. In another work, core@shell $Fe_3O_4/SiO_2/(CH_2)N^+Me_3Br_3^-$ NPs have been proven to be useful for the syntheses of imidazole, benzothiazole, and perimidine derivatives [329]. The synthesis of 28 five- and six-membered heterocycles was analyzed under solvent-free conditions at 80 °C, reaching reaction times as short as 10 min and yields of 95% (Fig. 18e).

Other examples in which Pd, graphene, or Fe_3O_4 are not used can also be found in the literature. For instance, high surface area trimetallic Au–Fe–Ag NPs with strong catalytic activity for the synthesis of α-β and β-β-dichloroenones were developed [330]. Efficient α-β and β-β-dichloroenone synthesis from a diazodicarbonyl compound and oxalylchloride was achieved in fluorobenzene (conversion of 99%, yield of 93% after 3 h). The use of trimetallic Au–Fe–Ag NPs simplifies and improves the common β-dichloroenone processes which result in mixtures of products, low regioselectivity/yields, and long reaction times. The cyclic diazodicarbonyl compound is treated with oxalyl chloride to obtain a yield of 92%, while trimetallic NP results in 93% yield (Fig. 18f).

Although they are not considered as MMNPs, it is worth noticing that magnetic NPs are also used as a support for the anchoring of other catalytically active species, including chiral/non-chiral amines, amino acids, Brønsted acids, metal complexes, crown ethers, quaternary salts, or enzymes [334–336]. Overall, MMNP catalyst particles combine a good catalytic activity with an easy removal by an external magnetic field due to the ferromagnetic/ferrimagnetic nature of one of the multicomponent constituents. After separation, the catalyst can be washed with appropriate solvents such as water, ethanol or dichloromethane, dried under vacuum, and then reused again for many cycles (usually 5–15) under identical synthetic conditions with no activity loss.

4.3.2. Degradation of pollutants

Dye and pharmaceutical industries discharge large amounts of industrial waste-water containing different organic pollutants, contaminating water reservoirs, and resulting in severe adverse effects on humans and wildlife [337,338]. Some of these pharmaceuticals, personal care products, or pesticides are known as persistent organic pollutants, which are difficult to degrade under conventional waste-water treatment processes [339]. Therefore, vast efforts are being now devoted to the development of advanced systems that effectively remove and/or detect organic pollutants from water. Among them, catalytic degradation in heterogeneous catalysis emerges as one of the most cost-effective approaches. Similar to the use of catalysis for synthesis reactions described above, the use of MMNPs allows the recovery of catalysts in an efficient manner while offering colloidal stability and support for different catalytic materials.

The inherent rapid electron conduction of GO can be used to develop magnetic catalysts with enhanced activity. In this sense, GO-Fe_2O_3 MMNPs with a good catalytic activity towards RhB degradation in the presence of H_2O_2 were developed by Song et al. [340]. It was seen the GO incorporation enhances the enzyme-mimetic activity of Fe_2O_3 to H_2O_2 (formation of $O_2^{\bullet-}$/$HO_2^{\bullet}$ and $^{\bullet}OH$) by accelerating the electron transport in the reaction system so the intrinsic oxidation ability of ferric ion is markedly enhanced (Fig. 19a). As a result, 68% of RhB was removed using GO-Fe_2O_3 MMNPs, whereas only 33% and 13% of RhB was degraded using bare Fe_2O_3 and GO groups, respectively (Fig. 19b). As developed materials display a simple synthesis procedure, great stability during storage, and low price, a variety of NPs, including metals, metal oxides, and nanocarbons, have been used to obtain nanoscale artificial enzyme mimics, nanozymes [341]. In this context, dual-shelled core@shell magnetic microspheres having different mono- or bi-metallic nanocrystals of ~11 nm (Au, Pd, PtAu, and PtPd) as mimetic enzymes for the colorimetric detection [342]. Fe_3O_4 NPs were coated by resorcinol/formaldehyde resin and diverse noble metal NPs and mono- and bi-metallic nanocrystals could be tuned by simply changing the metal precursor. MMNPs showed good peroxidase-like activity, providing a LOD of 3.1 and 1.36 μM for H_2O_2 and glucose, respectively. Pt-coated NP clusters consisting of a few hundred 15 nm Fe_3O_4 particles were applied as peroxidase mimics to detect *E. coli* with a LOD of 10 cfu/mL [343]. Catalytic decomposition of added tetramethylbenzidine is promoted by the decomposition of H_2O_2 into two $OH^{\bullet}$ radicals provided by Pt surfaces, turning the solution blue. Other similar

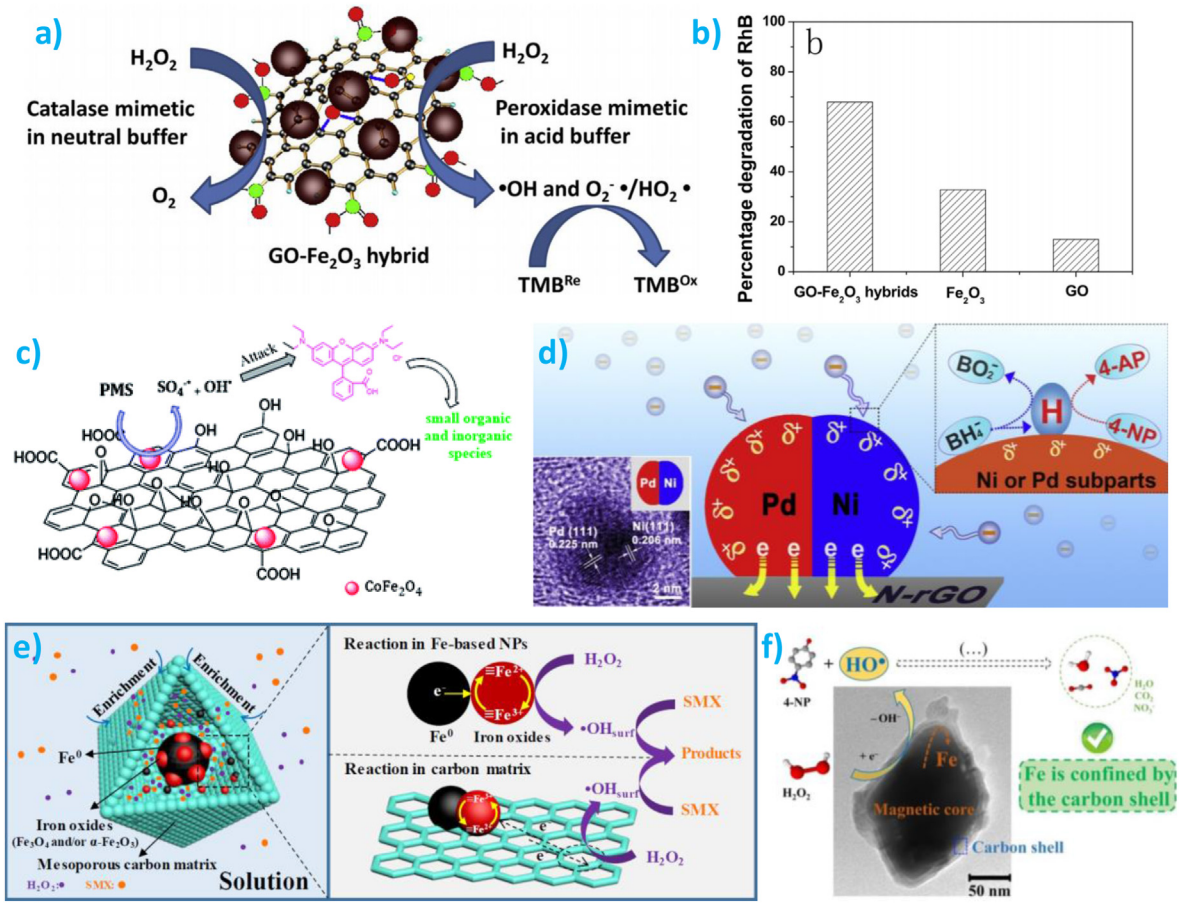

Fig. 19. **a**), (**b**) Scheme summarizing the enzyme mimetic activity of Fe_2O_3 supported onto GO and degradation percentage of RhB for GO-Fe_2O_3, bare Fe_2O_3 and GO. Reproduced with permission of Elsevier from the study by Song et al. [340]. (**c**) RhB decomposition by $CoFe_2O_4$ NPs combined with GO in the presence of PMS. Reproduced from the study by Tabit et al. [347] with permission from The Royal Society of Chemistry. (**d**) Scheme showing the synergistic catalytic degradation of 4-NP over Ni–Pd/NrGO. Reproduced with permission of Elsevier from the study by Liu et al. [350]. (**e**) Schematic illustration depicting H_2O_2 activation and subsequent SMX degradation in the Fe@MesoC/H_2O_2 Fenton-like system. Reproduced with permission of Elsevier from the study by Tang and Wang [351]. (**f**) Schematic representation of 4-NP degradation into H_2O, CO_2, and NO_3^- by a MMNP composed by a magnetic Fe_3O_4 core and an outer carbonaceous shell. Reproduced with permission of Elsevier from the study by Ribeiro et al. [352]. GO, graphene oxide; NP, nanoparticle; PMS, peroxymonosulfate; rGO, reduced graphene oxide; SMX, sulfamethoxazole.

examples include the preparation of magnetic $CoFe_2O_4$@CoS (cobalt sulfide) nanotubes with peroxidase-like activity for dopamine detection [344], ternary magnetic metal-organic framework-based MMNP nanozymes consisting on Fe_3O_4@Au@MIL-100(Fe) with a unique photoinduced enhanced peroxidase-like resulting from the combined peroxidase-like and SERS activity of nanocatalysts [345], or superparamagnetic Fe_3O_4 NP@carbon nitride nanotube MMNPs with ultra-high peroxidase mimetic activity [346].

GO and rGO have also been combined with $CoFe_2O_4$ to obtain MMNPs with efficient dye degradation ability [347]. RhB degradation reactions were performed in the presence of peroxymonosulfate (PMS). When coupled with Co^{2+} ions, better organic contaminant degradation than Fenton reactions could be achieved (Fig. 19c). As a consequence, the total organic carbon removal efficiency of RhB reached 89% in only 12 min. Interestingly, the degradation rate was much faster using GO instead of rGO due to the different electronic structure and additional functional surface –OH groups on GO. By immobilizing 8 nm Ni NPs onto rGO, the reduction of 4-nitrophenol (4-NP) to 4-aminophenol (4-AP) with sodium borohydride ($NaBH_4$) can be enhanced over 2.5 times in comparison with pure Ni NPs [348]. rGO avoids NP agglomeration and increases the electron transfer thanks to its conducting character. Moreover, the strong π-π interactions between 4-NP and rGO afford a high concentration of 4-NP near to the active Ni, promoting a highly efficient contact between them. As a result of such effects, the overall catalytic activity is markedly improved. Similarly, graphene/Fe_3O_4 MMNPs were used as a large surface area support for bi-noble metal AuPt NPs to prepare multifunctional nanocatalysts for 4-NP reduction [349]. It was seen that Fe_3O_4 not only facilitates catalyst recovery but also promotes 4-NP reduction reactions by transferring the electrons from Fe_3O_4 to Au and Pt, yielding a degradation rate as high as 17.99 mg^{-1}/s, which is superior to most Au- or Pt-based nanocatalysts reported.

Heterogeneous Ni–Pd nanodimers were grown onto nitrogen-doped rGO for efficient 4-NP reduction, reaching degradation rate constants as high as 3400 s^{-1}/g [350]. During catalyst preparation, a core@shell structure was avoided as such NPs do not fully exploit the catalytic activity of the core; i.e. the reaction would take place on the Pd shell and Ni core would act as an inert support. Alloying of Ni and Pd was also prevented, as Pd heteroatom incorporation may result in the loss of ferromagnetic properties, hindering the recovery step. As a result of the obtained morphology, the electron transfer between Ni–Pd and the supporting rGO contributes to the strong adsorption of negatively-charged reactants while active hydrogen is formed over Ni–Pd, reducing 4-NP to 4-AP upon $NaBH_4$ addition (Fig. 19d).

Not only graphene but also other carbonaceous structures can be used to boost the catalytic activity of magnetic NPs. Fe-based

magnetic NPs were embedded into mesoporous carbon (Fe@MesoC) to obtain Fenton-like catalyst for the degradation of sulfamethoxazole antibiotic [351]. Thanks to the enrichment of the outer mesoporous carbon matrix which also serves to avoid Fe NP aggregation, the abundant active sites of the inner Fe-based NPs served as active sites together with the outer shell, converting 100% of the antibiotic in only 120 min. As schematically represented in Fig. 19e, authors concluded that the electron transfer from Fe^0 to iron oxide in the inner Fe-based NPs facilitates the reduction of $\equiv Fe^{3+}$ to $\equiv Fe^{2+}$, accelerating hydroxyl radical formation ($^{\bullet}OH$) and thus boosting sulfamethoxazole degradation. 12 nm Fe_3O_4 NPs were encapsulated within a graphitic structure to obtain large specific surface area (330 m^2/g) magnetic catalysts advantageous for catalytic wet peroxide oxidation [352]. Using 4-NP as a model dye, authors concluded that Fe_3O_4 incorporation into graphite enhanced the catalytic activity in catalytic wet peroxide oxidation thanks to increased adsorptive interactions between the catalysts surfaces and pollutant molecules. Additionally, the leaching of Fe species from Fe_3O_4 to the outer medium (which is a commonly found matter which reduces catalytic efficiency) was limited due to the confinement caused by the graphitic structure (Fig. 19f). As a result, 4-NP was reduced to H_2O, CO_2 and NO_3^- with a remarkable pollutant removal ratio as high as 5000 mg/g/h.

There are other examples comprising non-carbonaceous structures as solid supports for MMNP catalyst fabrication. For instance, 28 nm Pd NPs were immobilized onto Fe_3O_4 stabilized with chitosan and agar to form micro-encapsulated particles which efficiently degraded 4-NP to 4-AP in water after only 180 s [321]. Magnetic Fe_3O_4 NPs were coated with a thin SiO_2 layer to be subsequently coated with Au and Ag NPs using stabilizing agents [353]. The synthesized Fe_3O_4@SiO_2@PEI-Au/Ag@PDA NPs were able to degrade 4-NP to 4-AP in 10 min, and thanks to their high saturation magnetization of 48.9 emu/g, they could be easily removed from the reaction medium and used again 8 times keeping a conversion degree above 95%. Halloysite clay nanotubes (HNT), biocompatible naturally occurring aluminosilicate nanotubes with an Al:Si ratio of 1:1, have been efficiently used as supports for catalytically active magnetic NPs thanks to their durable, cheap, and one-dimension characteristics. For instance, dumbbell-like oxygen-containing HNT/Fe_3O_4 MMNPs were prepared for the reduction of the highly toxic Cr(VI) into low-toxicity Cr (III) [354]. After Cr(VI) adsorption (132 mg/L) by ion exchange and coordination interaction, the electron-donor effect of oxygen-containing organic groups was able to reduce the contaminant Cr(VI) to the safer Cr (III). 15 nm Fe_3O_4 NPs were attached to HNT for the degradation of pentachlorophenol (PCP), a highly recalcitrant chlorinated organic compound widely used as a pesticide and disinfectant [355]. Fe_3O_4 remained well-dispersed along the HNT, minimizing the interparticle aggregation and thus accelerating PCP decomposition by nearly 2.5 times in comparison with bare Fe_3O_4.

Thanks to its effectiveness, rapid degradation, and economic viability, photocatalytic degradation has also attracted increasing attention in the last two decades. During photocatalysis, a variety of strong reactive oxidation species such as $OH^{\bullet}$, $O_2^{\bullet-}$, or H_2O_2 are generated as a result of light excitation, which can later oxidize/reduce organic pollutants into H_2O, CO_2, and other biodegradable intermediates [356,357]. Nowadays, TiO_2 is the most commonly used photocatalyst because of its high stability and oxidative power [83,358,359]. However, once the pollutant has been degraded, TiO_2 NPs remain dispersed in the liquid media, making their collection a tedious task. To enable their easy recovery and recycling, photocatalytic NPs can be combined with magnetically active particles. Interestingly, the combination of metal and semiconductor components affords the fabrication of MMNPs with combined optical, magnetic, and catalytic functionalities. In this regard, Fe_3O_4 NPs were coated by TiO_2 NPs for methylene blue (MB) degradation under UV light ($\lambda = 362$ nm) [360]. As a direct contact between TiO_2 and Fe_3O_4 can lower the photoactivity of the MMNPs due to photodissolution and electron-hole recombination effects, authors prepared a polystyrene passivating layer by Pickering miniemulsion polymerization between titania and magnetite. Nearly 90% of MB was degraded after 1 h of irradiance at 2.3 mW/cm^{+2} with no activity loss observed after 3 cycles, indicating the potential of developed materials for the photocatalytic decomposition of pollutants.

To further boost the catalytic activity, noble and magnetic metal Au@Ni nanocrystals were coated with ZnO nanopyramids [361]. Upon irradiation with UV light, the photo-induced electrons in the conduction band of ZnO can transfer to the metal due to its lower Fermi energy level and therefore create an effective charge separation. As a result, 97% of RhB was degraded in 60 min. Core@shell MMNPs having a magnetically active core and a catalytically active shell such as Fe_3O_4@TiO_2 have proven to be efficient in the degradation of different pollutants such as 4-methylaminoantipyrine, the active metabolite of the dipyrone analgesic [362]. Upon irradiation with a 125 W high-pressure mercury lamp ($\lambda = 254$ nm) for 60 min, a 70% mineralization of 4-methylaminoantipyrine was obtained. These results indicate a favorable interaction between electrons in titania surface and the magnetic core, which does not increase the electron-hole recombination and thus keeping the catalytic activity of the TiO_2 shell intact (with the advantage that synthesized MMNPs can be easily removed with external magnetic fields).

In spite of obtained good efficiencies, similarly to TiO_2, the above reported magnetic photocatalysts are mostly excited under UV light, resulting in a low utilization efficiency of the solar spectrum (UV region only accounts for ~5% of the solar spectrum at sea level) [363]. To face this issue, many efforts have been devoted to the development of magnetic photocatalyst which can be excited in the visible region. In this framework, Ag-supported magnetic TiO_2 MMNPs were synthesized for aqueous methyl orange (MO) degradation under visible light irradiation [364]. Upon appropriated Ag content, the absorption band of Ag/TiO_2/Fe_3O_4 was shifted to the visible light range as shown in Fig. 20a, and the bandgap energy decreased to 1.163 eV (3.138 and 2.702 eV for bare TiO_2 and Ag/TiO_2, respectively). These changes were achieved thanks to the LSPR of the Ag and may enhance the photocatalytic activity of magnetic Ag/TiO_2/Fe_3O_4 and increase its potential in applications under visible light. Indeed, Fig. 20b shows a faster MO degradation in the presence of Ag/TiO_2/Fe_3O_4, reaching ~50% after 90 min (note that no degradation is observed under dark conditions). Following this approach, many different catalysts that are activated under visible light can be designed by modifying titania NPs. Alberti et al. prepared TiO_2-zeolite magnetic catalyst for MB degradation under solar illumination using Fly Ash industrial waste as a source material [365]. Zeolites resulted particularly interesting as support materials due to their high surface to volume ratio and porous structure, which may provide a large specific surface area where catalytic reactions can proceed.

Similarly, photocatalytic MMNPs composed of 10 nm Fe_3O_4 NPs assembled onto 120 nm diameter Bi_2O_4 NRs were prepared for a visible-light directed degradation of ibuprofen [367]. Thanks to the combination of the narrow bandgap of 2.0 eV of Bi_2O_4, and the conduction band difference of Fe_3O_4 (+1 eV) and Bi_2O_4 (−0.37 eV), an enhanced photoinduced charge separation of the electron-hole pairs was obtained, resulting in a 75% degradation of ibuprofen in 30 min $ZnFe_2O_4$/C_3N_4 MMNPs show a good photo-Fenton degradation of aqueous organic pollutants under visible light ($\lambda > 420$ nm) irradiation [368]. Using Orange II as a model dye (50% degradation in 60 min), authors observed that graphitic C_3N_4 sheets acted as a p-conjugated material for the heterojunction

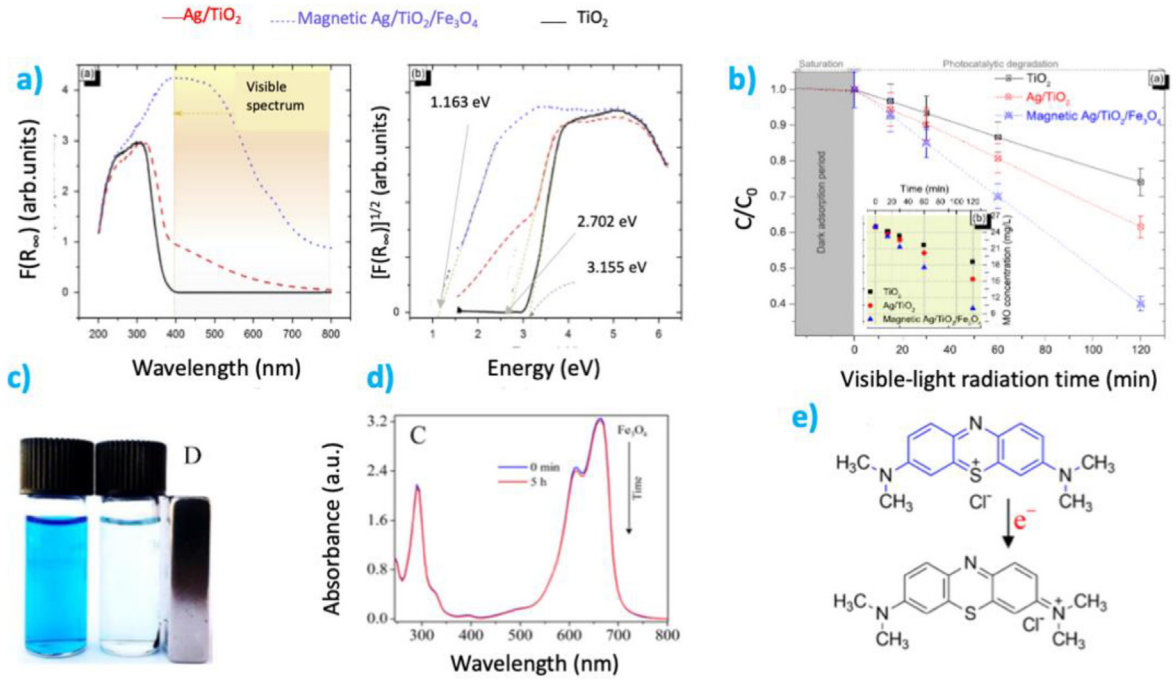

Fig. 20. a) Diffuse reflectance spectra of TiO_2, Ag/TiO_2, and magnetic $Ag/TiO_2/Fe_3O_4$ and its corresponding Kubelka-Munk function plot versus light energy. (b) Methyl orange photodegradation using TiO_2, Ag/TiO_2, and magnetic $Ag/TiO_2/Fe_3O_4$ catalyst as a function of visible light irradiation time. Reproduced with permission of Elsevier from Ref. [364]. (c) UV–Vis absorbance spectra showing methylene blue degradation in 9 min by Fe_3O_4@Ch-Au; (d) normalized rate constant (k_{nor}) values depending on the illumination type; (e) disappearance of methylene blue dye color following degradation with Fe_3O_4@Ch-Au and the removal of the NPs using an external magnet [366]. Copyright 2017 American Chemical Society NP, nanoparticle; UV, ultraviolet.

formation with the magnetic $ZnFe_2O_4$ (bandgap of 1.9 eV, visible-light response), while catalytically decomposing H_2O_2 to $^{\bullet}OH$ radicals. Upon combination with $ZnFe_2O_4$, the absorption range of C_3N_4 is extended, improving the quantum yield and preventing the inherent high recombination rate of photogenerated electron–hole pairs in C_3N_4 sheets. Moreover, a remarkable catalytic ability at neutral conditions was obtained, representing a great advantage over the traditional Fenton system (Fe(III) hydroxides tend to precipitate at pH > 3) [369].

Due to the ability of graphene to accept the electrons from semiconductor and prevent recombination of photogenerated electron-hole pairs, different photocatalysts have been anchored onto graphene-related materials. For example, 24 nm $ZnFe_2O_4$ NPs have been deposited onto rGO sheets for photo-Fenton-like degradation under visible irradiation using PMS as an oxidant [370]. rGO prevented $ZnFe_2O_4$ NP aggregation and activated PMS to produce sulfate radicals ($SO_4^{\bullet-}$) which degrade more than 80% of recalcitrant organic pollutants (Orange II, MO, methyl violet, RhB or MB) in less than 120 min. A similar mechanism involving $SO_4^{\bullet-}$ formation was also found for $MnFe_2O_4$/rGO, although the degradation of organic dyes was initiated upon the addition of potassium PMS as an oxidation agent for PMS instead of using visible light [371]. Similarly, rGO-$CoFe_2O_4$ MMNPs were developed for the photodegradation of malachite green in water [372]. Due to the higher valence band energy of $CoFe_2O_4$ in comparison with rGO, the photogenerated electrons are transferred from $CoFe_2O_4$ to rGO, boosting the sunlight-excited photo-Fenton-like photocatalytic activity.

Parandhaman et al. immobilized Au and Pd NPs onto Fe_3O_4 using chitosan (Ch) to obtain separable MMNPs with a good catalytic performance [366]. Prepared Fe_3O_4@Ch-Au and Fe_3O_4@Ch-Pd showed absorption peaks at $\lambda = 525$ and 305 nm, respectively, and were used as photocatalysts under different illumination conditions. As seen in Fig. 20c, the degradation of MB was tested as a model dye under different conditions, reaching a complete degradation after 1, 2, and 3 min upon UV light (10 W, 285 nm), sunlight (average amount of solar radiation of 5.12 $kWh \cdot m^2$), and visible light (mercury vapor lamp, 400 W) exposure, respectively (Fig. 20d). Moreover, the catalysts were easily recoverable after MB degradation using an external magnet (Fig. 20e), allowing its reuse multiple times with no catalytic activity loss.

5. Life cycle assessment and circular economy considerations

The beginning of the 21st century has witnessed a boom in the development and application of nanomaterials. In this framework, magnetic NPs are being increasingly used for applications including environmental remediation/catalysis [340,347,373], sensing [215,216], and imaging [13,78]. Their current widespread use, together with the projections of their incorporation into consumer goods, is raising serious concerns about their safety and toxicity. This topic will not be covered in this work as several reviews have thoroughly analyzed the toxicity effects associated with different kinds of NPs [374–376]. On the contrary, the environmental risks associated with the use of magnetic NPs have been scarcely investigated. This is in contrast with the recent government policies which call for significant reductions in energy demand and non-renewable materials consumption. A remarkable example is the European Green Deal brought forward by the European Commission, which aims towards a climate neutral Europe by 2050 [377]. It is thus essential to provide a holistic understanding of the environmental impacts associated with the fabrication, use, and recycling/disposal of magnetic NPs. This can be done in the light of the life cycle assessment (LCA) methodology as it provides the means to account for the environmental impacts or materials, processes, products, or even services [378,379], where the impact of the synthetic routes followed for the production of NPs (including raw material extraction and energy required for fabrication), together

with their use, management, and their end-of-life are analyzed. Implementing a '*cradle to grave*' product cycle LCA may allow the identification of the key parameters affecting the environmental impact of magnetic NPs, enabling their optimization and further up-scaling. Importantly, not only greenhouse gas emissions are quantified but also impact categories such as fine particulate matter formation, eutrophication, human toxicity, land use, mineral resource scarcity or acidification are considered [378]. In addition, the early application of LCA through eco-design strategies enables making informed choices on the sustainability of new products, so the processes having low Technological Readiness Levels could be re-designed to lower their footprint when up-scaled [380]. Unfortunately, despite the intensive works carried out in the field of consumer products, the LCA of magnetic NPs in general, and MMNPs especially, has been limited to a few examples. Therefore, in this section, we mostly rely on studies based on single-component magnetic nanomaterials which can be extrapolated in many cases to MMNPs.

As magnetic NP fabrication approaches usually rely on the use of toxic raw materials, it becomes essential to substitute the reagents by more sustainable precursors, reducing, and stabilizing agents. In 2017, Feijoo et al. used a *cradle-to-gate* LCA to provide the first detailed life cycle inventory and environmental assessment of different magnetic NP production (see Fig. 21 for the environmental impact potentials) [381]. Sterically stabilized magnetite (9.9 nm) and coated NPs with oleic-acid (7.8 nm), silica (21.5 nm) or PEI (10 nm) were synthesized and the outcomes from the fabrication process were used as the life cycle inventory data. The functional unit (FU) was defined as the amount of NPs in mg produced per batch. Ecoinvent® 2016 database, the average electricity generation and import/export data from Spain and the ReCiPe method were used. Results reveal that $FeCl_3$, NH_4OH, and TMAOH contribute mostly during the synthesis of sterically stabilized magnetite NPs, while the HCl used to adjust medium pH to 4 for PEI-coated NPs contributes by more than 60% to the environmental impacts (its substitution by H_2SO_4 was encouraged). The cylcohexane used during re-dispersion of OA-coated and silica-coated NPs accounts for 90 and 25%, respectively. Overall, the manufacturing stage is dominated by the environmental impacts associated with energy and chemical use, especially for silica-coated NPs. Indeed, energy consumption contributes to over 90% of life cycle burdens in this case. Sterically-stabilized, PEI-coated and OA NPs present lower and similar environmental impact contributions. Although silica-coated NPs are the most reliable option performance-wise, their associated environmental impacts hinder its selection as an adequate alternative. In this sense, PEI-coated NPs are preferred as they show a good balance between performance and limited environmental impact.

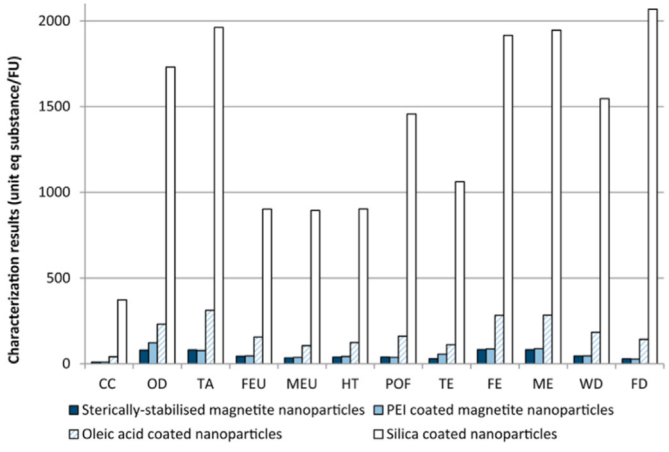

Fig. 21. Total environmental impact depending on magnetic NP production. Impacts are categorized into: climate change (CC), ozone depletion (OD), terrestrial acidification (TA), freshwater eutrophication (FEU), marine eutrophication (MEU), human toxicity (HT), photochemical oxidants formation (POF), terrestrial ecotoxicity (TE), freshwater ecotoxicity (FE), marine ecotoxicity (ME), water depletion (WD) and fossil fuel depletion (FD). Reproduced with permission of Elsevier from the study by Feijoo et al. [381].

The environmental assessment of magnetite NPs prepared *via* a large-scale co-precipitation approach reveals that this method is a preferred environmentally friendly choice over other synthetic processes [382]. Fe_3O_4 NPs synthesized with glutathione as both the reductant and stabilizer show a markedly reduced environmental impact than the Fe_3O_4 produced by the conventional co-precipitation method (FU: 1 g NP) [383]. The energy demand associated with the synthesis was reduced from 46 to 0.25 kJ, although the amount of raw materials used remained similar. As a result, the global warming potential (GWP) was reduced by 10 times (Fig. 22a) while human toxicity remained comparable (Fig. 22b). Overall, sodium hydroxide and glutathione contributed mostly to the environmental impact of the so-called 'green synthesis' (Figs. 22c and d). Importantly, no coating step was required as the glutathione led to the reactive surface −SH groups, avoiding the need for further energy- and material-intensive procedures.

Essentially, LCA studies of magnetic NPs have been focused on a *cradle-to-gate* approach. However, a *cradle-to-grave* approach may provide a real picture of the environmental impact associated with these materials. Baresel et al. recently analyzed how the recovery rate affects the resulting LCA of magnetic NPs used for water treatment purposes [384]. Magnetite NPs prepared from $NaBH_4$ reduction of iron acetylacetonate solution and subsequently modified with polystyrene or divalent amino acid-based surfactants were used as adsorbents for heavy metal ions. As shown in Fig. 22e, the effect of the recovery ratio from 0 to 100% by external magnetic forces after water treatment on the total GWP was studied. For all the cases, the raw materials account for nearly two-thirds of the impacts. The GWP can be reduced by 835 times upon full recovery of NPs, reflecting the pivotal role of the recovery rate towards minimizing the environmental impact of magnetic materials. A laser vaporization synthesis has been recently proposed to fabricate spherical pure γ-Fe_2O_3 (ferromagnetic) and core@shell γ-Fe_2O_3/SiO_2 (superparamagnetic) NPs with reduced environmental impact [385]. LCA data were extracted from two pilot-scale plants and the previously reported works, and the FU was selected as the MRI contrast agent unit dose required for a patient with 70 kg body weight. After process optimization, their method required no metal catalyst or halogenated organic solvents, such as DMF or toluene, decreasing resource depletion, environmental impacts, and ozone depletion. Thanks to reduced energy demand, a decrease of the GWP up to 64% was achieved. Occupational risk assessment according to ISO/TG 12901-2 confirmed a low toxicological and biological hazard potential. These results confirm that in contrast to wet chemical synthesis, laser vaporization is an effective method to develop core@shell NPs with reduced environmental impact and low hazard potential.

Scarce works have been done to date to analyze the environmental impacts associated with multicomponent magnetic materials. In one of such works, a LCA of magnetic NPs used for Fenton and photo-Fenton catalysts based on Fe_3O_4 NPs stabilized with PAA, PEI, and SiO_2 supported onto TiO_2 or ZnO has been reported [386]. Authors experimentally performed NP synthesis and used such data to study the LCA (Ecoinvent®database, ReCiPe methodology). NPs used for photocatalysis show a markedly increase environmental impact, mostly arising from the complexity of the downstream stages necessary for the final formulation, which require

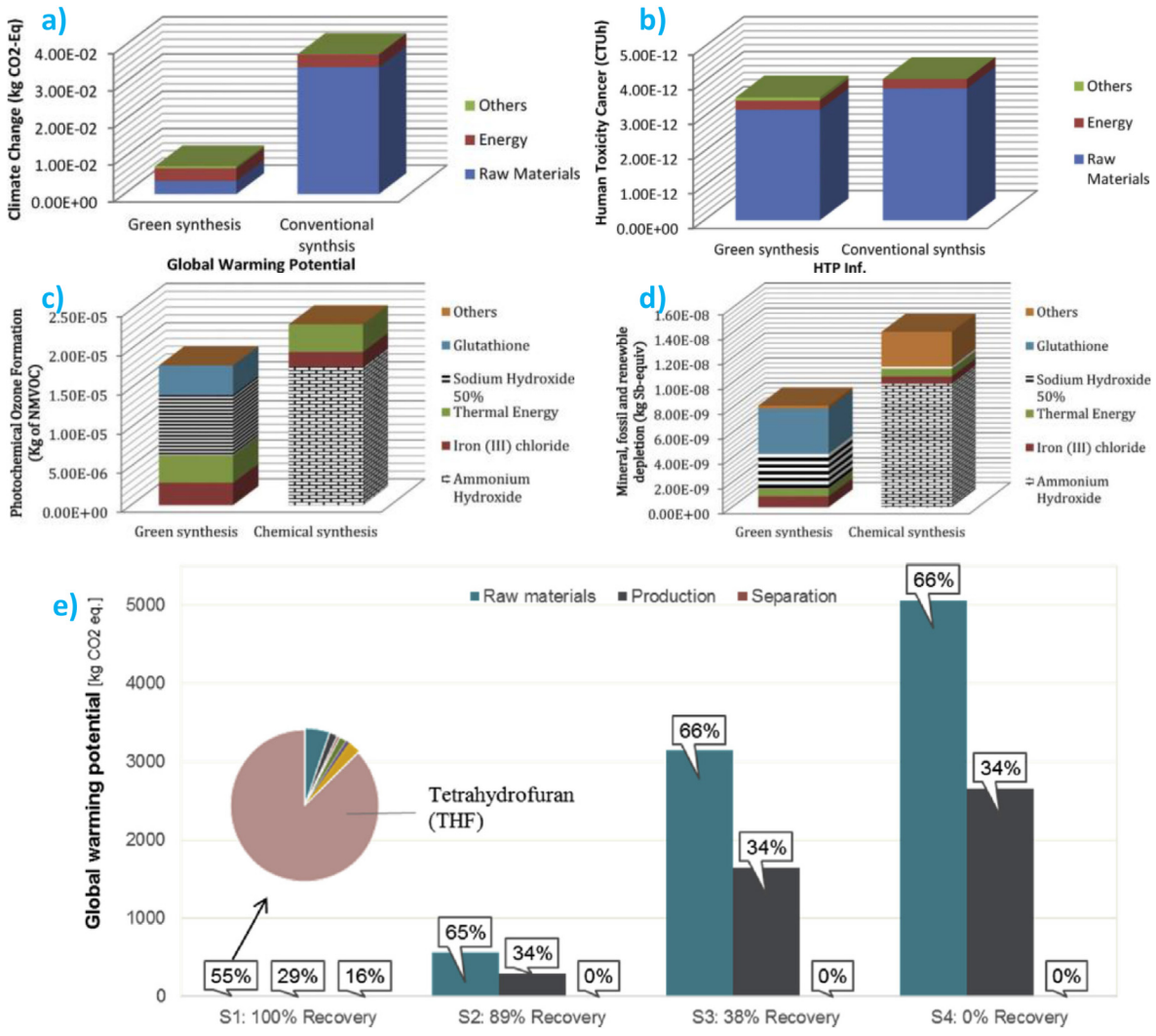

Fig. 22. Environmental impacts on the synthesis step for (**a**) global warming potential and (**b**) human toxicity. Distribution of impact on (**c**) photochemical ozone formation and (**d**) mineral fossil and renewable depletion. Reproduced with permission of Elsevier from the study by Marimón-Bolívar and E.E. González [383]. (**e**) GWP distribution depending on the NP recovery ratio. Reproduced with permission of Elsevier from the study by Baresel et al. [384]. GWP, global warming potential; NP, nanoparticle.

additional energy and chemical products (Fig. 23). Based on the performance of synthesized NPs, the removal of model organic pollutants, together with the environmental impact analysis, was studied. Authors concluded that Fe_3O_4@PAA and Fe_3O_4/ZnO NPs were preferred for Fenton and photo-Fenton processes, respectively.

Most of the works conclude that energy and chemical consumption have a dominant contribution to the life cycle environmental impacts. In this framework, as chemicals can contribute up to 60% of the environmental burdens [381], the replacement of raw materials is encouraged towards providing cleaner approaches to the chemical synthesis of magnetic NPs. This can be done for instance using waste as a source for NP development, which represents a plausible approach toward upcycling [387,388]. An excellent circular economy example applied to magnetic NPs is the preparation of TiO_2-based heterogeneous magnetic photocatalyst from fly ash, i.e. iron and steel industrial waste material [365]. Fly ash was converted into a magnetic zeolite upon a one-step hydrothermal activation process, providing both a solution to the waste management in landfill and solving the water pollution issues associated with the multi-step processes. Other attractive green solution results in the microbial synthesis of magnetic NPs using metal-reducing bacteria, which can enzymatically reduce several high oxidation state metals to yield cell-templated NPs [389]. In contrast to conventional abiotic processes that include mining, crushing,

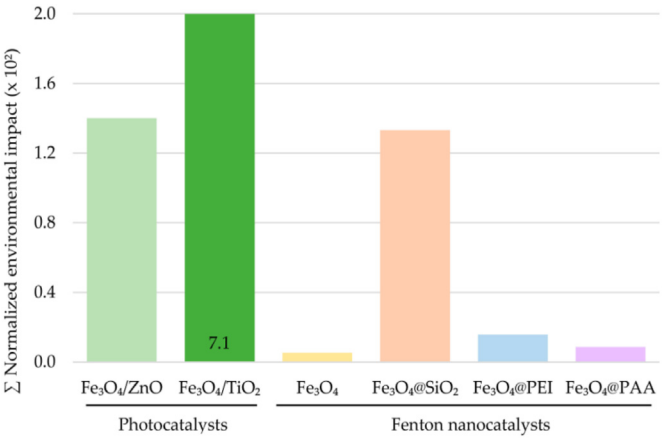

Fig. 23. Normalized environmental impacts associated with the synthesis of Fenton and photo-Fenton magnetic catalysts NPs. Reproduced from the study by Feijoo et al. [386]. NP, nanoparticle.

grinding, concentration, titration, filtration, and purification steps, which in turn increase the energy and raw material input, biosynthetic approaches do not require harsh chemicals and the synthesis is performed under ambient temperatures. In this line, Joshi et al. reported the synthesis and LCA of the microbial reduction of natural Fe(III) to yield magnetic Fe(II) NPs [390]. In comparison with current industrial fabrication, savings of 0.77 kg·CO_2 eq. (GWP), 3.53 MJ (natural gas), 13.73 MJ (fossil resources), and 4.97 m^3 (water) were achieved per kg of NP, lowering the production cost by 315 €·kg^{-1}.

In spite of the growing awareness of the life cycle of NPs at both the scientific and industrial level, there is still a lack of comparable and reliable reported studies. As a consequence, many uncertainties with the estimation of the environmental impacts associated with their use are found. Main obstacles arise from the immature technology and markets associated with MNPs, a reluctant perspective to provide accurate information on the synthetic route, and the lack of knowledge on the end-of-life of magnetic NPs. Moreover, the development of a 'substitution guideword' addressing possible safer processes for MMNPs (similarly to those prepared form general metal NPs) synthesis is needed [391]. Hopefully, new published works may arise in this field, shedding further light. The public disclosure of the environmental impacts related to MNP production may guide new sustainable designs may help scientist and industry to fulfill the UN 2030 agenda regarding the Sustainable Development Goal 12 (Responsible consumption and production), 13 (Climate action), 14 (Life below water), and 15 (Life on land) [392].

Overall, reported LCA results highlight the pivotal role that presents the efficient reuse toward lowering their associated environmental impacts. As shown in this work, this can be relatively easily achieved as magnetic NPs (either in dispersion or within a matrix) are efficiently separated and captured through external magnetic fields [360,364]. This functionality can be also used to obtain materials with novel functionalities. In this context, Ge et al. reported a clever strategy to enhance the reusability of the magnetic NPs used for algae harvesting [393]. Steric acid-coated Fe_3O_4–ZnO MMNPs shift their hydrophobidity under UV_{365} irradiation due to the generation of $^{\bullet}OH$ radicals, promoting algae detachment, and enormously facilitating the recovery of the NPs from algal slurry. As a result, one of the bottlenecks of algae harvesting (lack of efficient procedures for separating microalgae on a large scale) can be solved. Moving from the bench on the industrial scale results essential to lower the environmental footprint, considering that the environmental impacts of NP production (bio-based in this case) can be lowered by a factor of 6.5 when transitioning from 10 g to 50 kg production [394]. In this sense, it results compulsory to enable NP separation-capture under continuous flow conditions. Using an optimized high gradient magnetic separation process, Powell et al. recovered up to >95% of Fe_3O_4 NPs presenting adsorbed contaminants from flowing water at 1 L/min (500 ppm NP concentration) [395], providing an excellent technology to be integrated into real-world water treatment devices.

Although the potential applications of MMNPs cover plethora of fields, the majority of the studies remain at the early development stage. In this sense, the non-mature technology character or MNP synthesis, the data scarcity neglecting certain relevant experimental conditions and the determination of the FU (the unit at which impact is normalized) are the most relevant current bottlenecks to obtain comparable results. In addition, sustainability in the field of MNP engineering should go along with circularity. In this sense, the benefits originating from the product lifetime extension should be considered as these strategies are at the core of circular patterns [396]. For instance, the use of magnetic multicomponent nanomaterials in catalysis enables their recovery by external magnetic fields and subsequent re-use [397], the application of protective coatings based on NPs can prevent metal corrosion and enhance durability [398], and the electric/magnetic-coupling effects in Ni@CNTs/Al_2O_3 multicomponent ceramic composites can protect electric/electronic devices due to the attenuation of electromagnetic wave energy by electrical conduction, dielectric loss, and magnetic loss [399].

A step further towards environmentally sustainable MNP synthesis may arise from the consideration of the atom economy, one of the 12 Green Chemistry principles [400]. Atom utilization efficiency indicates the process efficiency regarding material use and is obtained as:

$$AUE = \frac{M_{dp}}{M_{dp} + M_{wp}}\, x\, 100 \tag{5}$$

where M_{dp} and M_{wp} are the molecular weight of the targeted products and by-products, respectively. In fact, the implementation of atom utilization efficiency enhances the understanding on how material-efficient the processes are, which emerge as one of the cornerstones of the circular economy [401].

6. Final remarks and outlook

In this review, the most recent key developments concerning synthesis, structure, properties, and application of MNPs have been presented and discussed. Special attention has been paid to establishing the existing relationships between how MNP morphologies affect the resulting functional properties in specific applications. Although a wide variety of elements combining several metals show magnetic activity, during the last years special attention has been paid to magnetite (Fe_3O_4), maghemite (γ-Fe_2O_3), and metallic substituted ferrites (MFe_2O_4, where M = Co, Cu, Ni, Mn, Mg). Given their shape isotropy, good size tunability, high yields, and ease of preparation, until the date most of the works rely on the use of spherical NPs. However, not only their size but also their shapes affect the magnetic properties of resulting MNPs. Therefore, here we have shown how different synthetic procedures can be applied to obtain nanomaterials with tailored structures, and thus, properties. We have focused on wet chemistry bottom-up approaches as the most spread synthetic methods, including co-precipitation, microemulsion, thermal decomposition, sol-gel, and solvothermal/hydrothermal processes. We discussed their advantages and disadvantages in terms of simplicity, scalability, and ability to control the chemistry and structure of magnetic NPs, and the existing relationship between such bottom-up methods and the resulting NP uniformity, size, and shape are summarized.

Besides structural and morphological features, combining MNPs with other materials to obtain MMNPs allows obtaining properties that offer enhanced functionalities in comparison with each individual constituent. To that end, magnetic NPs can be combined with porous NPs to provide additional specific surface area for drug delivery or pollutant removal, with plasmonically active metal NPs for optical – imaging - sensing applications, or with catalytically active moieties for environmental remediation. In all cases, awareness should be taken into consideration regarding the possible adverse effects depending on the application, for instance, for biomedical in vivo or environmental applications, and the necessary tests are regulations should be implemented. Among the different reported morphologies, core@shell, core-satellite, yolk-shell, Janus NPs, and nanochains formed by a set of NPs are the most abundant ones. The underlying relationship between preparation methods, materials, and properties of these commonly found multicomponent nanostructures are outlined.

Although combining two or more components typically results in enhanced functionalities, special care should be taken when selecting the counterpart materials and the type of heterostructure morphology as the generated synergistic effects may not be desirable. For example, if an intimate contact between both components of the MNP with its surrounding environments is required, JNPs are preferred over core@shell NPs as the core (in the latter type) is encapsulated and does not directly interact with the outside medium. When applied to catalysis, these issues play a pivotal role, as the more catalytically active component cannot remain protected from the environment. On the other side, core@shell offers protective layers for long-term operations in biomedical applications. Thus, together with the selection of nanomaterials, the nanostructure type-properties relationship is of utmost importance for the feasibility of different applications and their final performance.

MMNPs are being currently explored as both *in vivo* and *in vitro* active materials for multimodal imaging. In such applications, MMNPs are used as contrast agents for two or more imaging modalities which together can overcome the drawbacks showed by each of the imaging techniques. Similarly, MMNPs have enabled a renewed interest in thermal therapies for cancer, where their use allows AMF-induced hyperthermia provides much higher spatial and temporal control than conventional hyperthermia treatments. Their combined use with photothermia or other theranostic functionalities transforms the NPs into a complete nanomedical system. This use is often combined with drug delivery, where the therapeutic drug is carried to the region of interest where the treatment activity is needed and released under an external stimulus, minimizing the possible drug side-effects. As a matter of fact, MMNP-based sensors are ideal for accurate and quick diagnosis and can be used as a tool for the detection of very low concentrations of sensitive analytes through electrode-based sensing or surface-enhanced Raman scattering. MMNPs also show great potential for catalytic applications, where after being combined with a high specific surface area or optically-catalytically active NPs, improved yields and catalytic activities taking advantage of the whole spectrum of the solar irradiation with easy removal through external magnetic fields can be achieved. Moreover, some specific substrates can improve electron transfer during the reaction, while others can limit the leaching of Fe species from Fe_3O_4.

The increased interest at both the scientific and industrial level raised by MMNPs makes their fabrication process a worrisome issue regarding the associated environmental impact. Although the environmental risks associated with the use of magnetic NPs has not been investigated in detail, mainly because of their recent appearance and the low level of technological readiness level, a holistic understanding of the environmental impacts associated with their synthesis, application, and recycling/disposal should be provided. The scarce works presented in the field using LCA methodology conclude that the environmental impacts are dominated by the energy and raw material use. Therefore, the replacement of raw materials is encouraged to provide cleaner approaches to the preparation of MNPs. In any case, it should be noted that the full recovery of NPs by external magnetic fields can minimize their environmental impact by up to 835 times, opening new possibilities for the development of MMNPs with reduced environmental footprint.

Given their outstanding properties, MMNPs are ready to be applied in many areas at the interface between biology, medicine, chemistry, physics, and engineering. These multifunctional materials show a bright future to address emerging biomedical and environmental challenges such as the coronavirus COVID-19 pandemic and water pollution. However, the quest for novel MMNPs with tailored morphology through environmentally-friendly and scalable approaches should be a priority to enable their industrial implementation. Moreover, special effort should be addressed to the simplification of synthesis methods that brings their use to other science disciplines while generating more robust NPs with higher enhanced synergistic properties. We hope this work will help to increase the interest in the synthesis and application of MMNPs, which is of prime interest across fundamental and applied materials science.

Declaration of competing interest

The authors declare the following financial interests/personal relationships which may be considered as potential competing interests:

Javier Reguera reports financial support was provided by Agencia Estatal de Investigación. Mikel Rincon Iglesias reports financial support was provided by Basque Government. Senentxu Lanceros-Mendez reports financial support was provided by Basque Government. Erlantz Lizundia reports financial support was provided by Basque Government.

Data availability

No data was used for the research described in the article.

Acknowledgments

The authors thank funding from the Spanish State Research Agency (AEI) through the project PID2019-106099RB-C43/AEI/10.13039/501100011033 and from the Basque Government Industry and Education Department under the ELKARTEK, HAZITEK and PIBA (PIBA-2018-06) programs, respectively.

References

[1] H. Althues, J. Henle, S. Kaskel, Functional inorganic nanofillers for transparent polymers, Chem. Soc. Rev. 36 (2007) 1454–1465, https://doi.org/10.1039/B608177K.

[2] O.A. Noqta, A.A. Aziz, I.A. Usman, M. Bououdina, Recent advances in iron oxide nanoparticles (IONPs): synthesis and surface modification for biomedical applications, J. Supercond. Nov. Magnetism 32 (2019) 779–795, https://doi.org/10.1007/s10948-018-4939-6.

[3] Q. Li, C.W. Kartikowati, S. Horie, T. Ogi, T. Iwaki, K. Okuyama, Correlation between particle size/domain structure and magnetic properties of highly crystalline Fe_3O_4 nanoparticles, Sci. Rep. 7 (2017) 9894, https://doi.org/10.1038/s41598-017-09897-5.

[4] E.D. Smolensky, H.-Y.E. Park, Y. Zhou, G.A. Rolla, M. Marjańska, M. Botta, V.C. Pierre, Scaling laws at the nanosize: the effect of particle size and shape on the magnetism and relaxivity of iron oxide nanoparticle contrast agents, J. Mater. Chem. B. 1 (2013) 2818–2828, https://doi.org/10.1039/C3TB00369H.

[5] H. Zeng, S. Sun, Syntheses, properties, and potential applications of multicomponent magnetic nanoparticles, Adv. Funct. Mater. 18 (2008) 391–400, https://doi.org/10.1002/adfm.200701211.

[6] J. Kudr, Y. Haddad, L. Richtera, Z. Heger, M. Cernak, V. Adam, O. Zitka, Magnetic nanoparticles: from design and synthesis to real world applications, Nanomaterials 7 (2017) 243, https://doi.org/10.3390/nano7090243.

[7] Alejandro G. Roca, Lucía Gutiérrez, Helena Gavilán, Maria Eugènia Fortes Brollo, Sabino Veintemillas-Verdaguer, María del Puerto Morales, Design strategies for shape-controlled magnetic iron oxide nanoparticles, Adv. Drug Deliv. Rev. (2019) 68–104, https://doi.org/10.1016/j.addr.2018.12.008.

[8] E. Lizundia, A. Maceiras, J.L. Vilas, P. Martins, S. Lanceros-Mendez, Magnetic cellulose nanocrystal nanocomposites for the development of green functional materials, Carbohydr. Polym. 175 (2017) 425–432, https://doi.org/10.1016/j.carbpol.2017.08.024.

[9] M. Rincon-Iglesias, E. Lizundia, S. Lanceros-Mendez, Water-soluble cellulose derivatives as suitable matrices for multifunctional materials, Biomacromolecules 20 (2019) 2786–2795, https://doi.org/10.1021/acs.biomac.9b00574.

[10] Z. Wu, S. Yang, W. Wu, Shape control of inorganic nanoparticles from solution, Nanoscale 8 (2016) 1237–1259, https://doi.org/10.1039/C5NR07681A.

[11] L. Wu, A. Mendoza-Garcia, Q. Li, S. Sun, Organic phase syntheses of magnetic nanoparticles and their applications, Chem. Rev. 116 (2016) 10473–10512, https://doi.org/10.1021/acs.chemrev.5b00687.

[12] N. Zhu, H. Ji, P. Yu, J. Niu, M.U. Farooq, M.W. Akram, I.O. Udego, H. Li, X. Niu, Surface modification of magnetic iron oxide nanoparticles, Nanomaterials 8 (2018) 810, https://doi.org/10.3390/nano8100810.
[13] N. Kang, D. Xu, Y. Han, X. Lv, Z. Chen, T. Zhou, L. Ren, X. Zhou, Magnetic targeting core/shell Fe3O4/Au nanoparticles for magnetic resonance/photoacoustic dual-modal imaging, Mater. Sci. Eng. C. 98 (2019) 545–549, https://doi.org/10.1016/j.msec.2019.01.013.
[14] Y. Wang, R. Zhao, S. Wang, Z. Liu, R. Tang, In vivo dual-targeted chemotherapy of drug resistant cancer by rationally designed nanocarrier, Biomaterials 75 (2016) 71–81, https://doi.org/10.1016/j.biomaterials.2015.09.030.
[15] J. Duchet, R. Legras, S. Demoustier-Champagne, Chemical synthesis of polypyrrole: structure–properties relationship, Synth. Met. 98 (1998) 113–122, https://doi.org/10.1016/S0379-6779(98)00180-5.
[16] M.Z. Rong, M.Q. Zhang, Y.X. Zheng, H.M. Zeng, R. Walter, K. Friedrich, Structure–property relationships of irradiation grafted nano-inorganic particle filled polypropylene composites, Polymer 42 (2001) 167–183, https://doi.org/10.1016/S0032-3861(00)00325-6.
[17] J. Wang, Q. Ma, Y. Wang, Z. Li, Z. Li, Q. Yuan, New insights into the structure–performance relationships of mesoporous materials in analytical science, Chem. Soc. Rev. 47 (2018) 8766–8803, https://doi.org/10.1039/C8CS00658J.
[18] B. Prasai, Y. Ren, S. Shan, Y. Zhao, H. Cronk, J. Luo, C.-J. Zhong, V. Petkov, Synthesis-atomic structure-properties relationships in metallic nanoparticles by total scattering experiments and 3D computer simulations: case of Pt–Ru nanoalloy catalysts, Nanoscale 7 (2015) 8122–8134, https://doi.org/10.1039/C5NR00800J.
[19] F. Ahmad, N. Ashraf, T. Ashraf, R.-B. Zhou, D.-C. Yin, Biological synthesis of metallic nanoparticles (MNPs) by plants and microbes: their cellular uptake, biocompatibility, and biomedical applications, Appl. Microbiol. Biotechnol. 103 (2019) 2913–2935, https://doi.org/10.1007/s00253-019-09675-5.
[20] M.C. Mascolo, Y. Pei, T.A. Ring, Room temperature co-precipitation synthesis of magnetite nanoparticles in a large pH window with different bases, Materials 6 (2013) 5549–5567, https://doi.org/10.3390/ma6125549.
[21] S. Rajput, C.U. Pittman, D. Mohan, Magnetic magnetite (Fe_3O_4) nanoparticle synthesis and applications for lead (Pb^{2+}) and chromium (Cr^{6+}) removal from water, J. Colloid Interface Sci. 468 (2016) 334–346, https://doi.org/10.1016/j.jcis.2015.12.008.
[22] S. Majidi, F. Zeinali Sehrig, S.M. Farkhani, M. Soleymani Goloujeh, A. Akbarzadeh, Current methods for synthesis of magnetic nanoparticles, Artif. Cell Nanomed. Biotechnol. 44 (2016) 722–734, https://doi.org/10.3109/21691401.2014.982802.
[23] F. Yazdani, M. Seddigh, Magnetite nanoparticles synthesized by co-precipitation method: the effects of various iron anions on specifications, Mater. Chem. Phys. 184 (2016) 318–323, https://doi.org/10.1016/j.matchemphys.2016.09.058.
[24] T. Hosono, H. Takahashi, A. Fujita, R.J. Joseyphus, K. Tohji, B. Jeyadevan, Synthesis of magnetite nanoparticles for AC magnetic heating, J. Magn. Magn Mater. 321 (2009) 3019–3023, https://doi.org/10.1016/j.jmmm.2009.04.061.
[25] S. Sun, H. Zeng, D.B. Robinson, S. Raoux, P.M. Rice, S.X. Wang, G. Li, Monodisperse MFe_2O_4 (M = Fe, Co, Mn) nanoparticles, J. Am. Chem. Soc. 126 (2004) 273–279, https://doi.org/10.1021/ja0380852.
[26] H. Shokrollahi, L. Avazpour, Influence of intrinsic parameters on the particle size of magnetic spinel nanoparticles synthesized by wet chemical methods, Particuology 26 (2016) 32–39, https://doi.org/10.1016/j.partic.2015.10.004.
[27] G. Gnanaprakash, S. Mahadevan, T. Jayakumar, P. Kalyanasundaram, J. Philip, B. Raj, Effect of initial pH and temperature of iron salt solutions on formation of magnetite nanoparticles, Mater. Chem. Phys. 103 (2007) 168–175, https://doi.org/10.1016/j.matchemphys.2007.02.011.
[28] A.R. Yasemian, M. Almasi Kashi, A. Ramazani, Surfactant-free synthesis and magnetic hyperthermia investigation of iron oxide (Fe_3O_4) nanoparticles at different reaction temperatures, Mater. Chem. Phys. 230 (2019) 9–16, https://doi.org/10.1016/j.matchemphys.2019.03.032.
[29] E. Hutamaningtyas, Suharyana Utari, B. Purnama, A.T. Wijayanta, Effects of the synthesis temperature on the crystalline structure and the magnetic properties of cobalt ferrite nanoparticles prepared via coprecipitation, J. Korean Phys. Soc. 69 (2016) 584–588, https://doi.org/10.3938/jkps.69.584.
[30] T. Saragi, B.L. Depi, S. Butarbutar, B. Permana, Risdiana, The impact of synthesis temperature on magnetite nanoparticles size synthesized by co-precipitation method, J. Phys. Conf. Ser. 1013 (2018), 12190, https://doi.org/10.1088/1742-6596/1013/1/012190.
[31] P. Azcona, R. Zysler, V. Lassalle, Simple and novel strategies to achieve shape and size control of magnetite nanoparticles intended for biomedical applications, Colloid Surf. A Physicochem. Eng. Asp. 504 (2016) 320–330, https://doi.org/10.1016/j.colsurfa.2016.05.064.
[32] M.R. Ghazanfari, M. Kashefi, M.R. Jaafari, Investigation of stabilization mechanism and size controlling of Fe3O4 nanoparticles using anionic chelating agents, Appl. Surf. Sci. 375 (2016) 50–56, https://doi.org/10.1016/j.apsusc.2016.03.067.
[33] A. Bahadur, A. Saeed, M. Shoaib, S. Iqbal, M.I. Bashir, M. Waqas, M.N. Hussain, N. Abbas, Eco-friendly synthesis of magnetite (Fe_3O_4) nanoparticles with tunable size: dielectric, magnetic, thermal and optical studies, Mater. Chem. Phys. 198 (2017) 229–235, https://doi.org/10.1016/j.matchemphys.2017.05.061.
[34] S. Akbari, S.M. Masoudpanah, S.M. Mirkazemi, N. Aliyan, PVA assisted coprecipitation synthesis and characterization of $MgFe_2O_4$ nanoparticles, Ceram. Int. 43 (2017) 6263–6267, https://doi.org/10.1016/j.ceramint.2017.02.030.
[35] R.G.D. Andrade, S.R.S. Veloso, E.M.S. Castanheira, Shape anisotropic iron oxide-based magnetic nanoparticles: synthesis and biomedical applications, Int. J. Mol. Sci. 21 (2020) 2455, https://doi.org/10.3390/ijms21072455.
[36] L. Feng, L. Jiang, Z. Mai, D. Zhu, Polymer-controlled synthesis of Fe_3O_4 single-crystal nanorods, J. Colloid Interface Sci. 278 (2004) 372–375, https://doi.org/10.1016/j.jcis.2004.06.019.
[37] D. Lisjak, A. Mertelj, Anisotropic magnetic nanoparticles: a review of their properties, syntheses and potential applications, Prog. Mater. Sci. 95 (2018) 286–328, https://doi.org/10.1016/j.pmatsci.2018.03.003.
[38] W. Zhang, S. Jia, Q. Wu, J. Ran, S. Wu, Y. Liu, Convenient synthesis of anisotropic Fe_3O_4 nanorods by reverse co-precipitation method with magnetic field-assisted, Mater. Lett. 65 (2011) 1973–1975, https://doi.org/10.1016/j.matlet.2011.03.101.
[39] Y. Zhang, L. Sun, Y. Fu, Z.C. Huang, X.J. Bai, Y. Zhai, J. Du, H.R. Zhai, The shape anisotropy in the magnetic field-assisted self-assembly chain-like structure of magnetite, J. Phys. Chem. C 113 (2009) 8152–8157, https://doi.org/10.1021/jp807937d.
[40] A. Drmota, Microemulsion Method for Synthesis of Magnetic Oxide Nanoparticles, IntechOpen, Rijeka, 2012, pp. 191–214, https://doi.org/10.5772/36154.
[41] A. Najafi, K. Nematipour, Synthesis and magnetic properties evaluation of monosized FeCo alloy nanoparticles through microemulsion method, J. Supercond. Nov. Magnetism 30 (2017) 2647–2653, https://doi.org/10.1007/s10948-017-4052-2.
[42] M. Mahmoudi, S. Sant, B. Wang, S. Laurent, T. Sen, Superparamagnetic iron oxide nanoparticles (SPIONs): development, surface modification and applications in chemotherapy, Adv. Drug Deliv. Rev. 63 (2011) 24–46, https://doi.org/10.1016/j.addr.2010.05.006.
[43] M. Bustamante-Torres, D. Romero-Fierro, J. Estrella-Nuñez, B. Arcentales-Vera, E. Chichande-Proaño, E. Bucio, Polymeric composite of magnetite iron oxide nanoparticles and their application in biomedicine: a review, Polym 14 (2022), https://doi.org/10.3390/polym14040752.
[44] T. Lu, J. Wang, J. Yin, A. Wang, X. Wang, T. Zhang, Surfactant effects on the microstructures of Fe_3O_4 nanoparticles synthesized by microemulsion method, Colloid Surf. A Physicochem. Eng. Asp. 436 (2013) 675–683, https://doi.org/10.1016/j.colsurfa.2013.08.004.
[45] D. Wang, C. Cao, S. Xue, H. Zhu, γ-Fe_2O_3 oriented growth by surfactant molecules in microemulsion, J. Cryst. Growth 277 (2005) 238–245, https://doi.org/10.1016/j.jcrysgro.2004.12.174.
[46] V.K. LaMer, R.H. Dinegar, Theory, production and mechanism of formation of monodispersed hydrosols, J. Am. Chem. Soc. 72 (1950) 4847–4854, https://doi.org/10.1021/ja01167a001.
[47] S.G. Kwon, Y. Piao, J. Park, S. Angappane, Y. Jo, N.-M. Hwang, J.-G. Park, T. Hyeon, Kinetics of monodisperse iron oxide nanocrystal formation by "heating-up" process, J. Am. Chem. Soc. 129 (2007) 12571–12584, https://doi.org/10.1021/ja074633q.
[48] L. Song, C. Yan, W. Zhang, H. Wu, Z. Jia, M. Ma, J. Xie, N. Gu, Y. Zhang, Influence of reaction solvent on crystallinity and magnetic properties of $MnFe_2O_4$ nanoparticles synthesized by thermal decomposition, J. Nanomater. 2016 (2016), 4878935, https://doi.org/10.1155/2016/4878935.
[49] B. Park, B.H. Kim, T. Yu, Synthesis of spherical and cubic magnetic iron oxide nanocrystals at low temperature in air, J. Colloid Interface Sci. 518 (2018) 27–33, https://doi.org/10.1016/j.jcis.2018.02.026.
[50] S. Belaïd, D. Stanicki, L. Vander Elst, R.N. Muller, S. Laurent, Influence of experimental parameters on iron oxide nanoparticle properties synthesized by thermal decomposition: size and nuclear magnetic resonance studies, Nanotechnology 29 (2018), 165603, https://doi.org/10.1088/1361-6528/aaae59.
[51] E. Wetterskog, C.-W. Tai, J. Grins, L. Bergström, G. Salazar-Alvarez, Anomalous magnetic properties of nanoparticles arising from defect structures: topotaxial oxidation of $Fe_{1-x}O|Fe_{3-\delta}O_4$ core-shell nanocubes to single-phase particles, ACS Nano 7 (2013) 7132–7144, https://doi.org/10.1021/nn402487q.
[52] H. Yang, T. Ogawa, D. Hasegawa, M. Takahashi, Synthesis and magnetic properties of monodisperse magnetite nanocubes, J. Appl. Phys. 103 (2008), 07D526, https://doi.org/10.1063/1.2833820.
[53] D. Kim, N. Lee, M. Park, B.H. Kim, K. An, T. Hyeon, Synthesis of uniform ferrimagnetic magnetite nanocubes, J. Am. Chem. Soc. 131 (2009) 454–455, https://doi.org/10.1021/ja8086906.
[54] G. Cotin, C. Kiefer, F. Perton, D. Ihiawakrim, C. Blanco-Andujar, S. Moldovan, C. Lefevre, O. Ersen, B. Pichon, D. Mertz, S. Bégin-Colin, Unravelling the thermal decomposition parameters for the synthesis of anisotropic iron oxide nanoparticles, Nanomaterials 8 (2018) 881, https://doi.org/10.3390/nano8110881.
[55] Z. Nemati, J. Alonso, L.M. Martinez, H. Khurshid, E. Garaio, J.A. Garcia, M.H. Phan, H. Srikanth, Enhanced magnetic hyperthermia in iron oxide nano-octopods: size and anisotropy effects, J. Phys. Chem. C 120 (2016) 8370–8379, https://doi.org/10.1021/acs.jpcc.6b01426.
[56] S. Laurent, D. Forge, M. Port, A. Roch, C. Robic, L. Vander Elst, R.N. Muller, Magnetic iron oxide nanoparticles: synthesis, stabilization, vectorization, physicochemical characterizations, and biological applications, Chem. Rev. 110 (2010), https://doi.org/10.1021/cr900197g, 2574–2110.
[57] B.L. Cushing, V.L. Kolesnichenko, C.J. O'Connor, Recent advances in the liquid-phase syntheses of inorganic nanoparticles, Chem. Rev. 104 (2004) 3893–3946, https://doi.org/10.1021/cr030027b.

[58] M.M.L. Sonia, S. Anand, V.M. Vinosel, M.A. Janifer, S. Pauline, A. Manikandan, Effect of lattice strain on structure, morphology and magneto-dielectric properties of spinel $NiGd_xFe_{2-x}O_4$ ferrite nano-crystallites synthesized by sol-gel route, J. Magn. Magn Mater. 466 (2018) 238–251, https://doi.org/10.1016/j.jmmm.2018.07.017.

[59] M. Ben Ali, K. El Maalam, H. El Moussaoui, O. Mounkachi, M. Hamedoun, R. Masrour, E.K. Hlil, A. Benyoussef, Effect of zinc concentration on the structural and magnetic properties of mixed Co–Zn ferrites nanoparticles synthesized by sol/gel method, J. Magn. Magn Mater. 398 (2016) 20–25, https://doi.org/10.1016/j.jmmm.2015.08.097.

[60] S.T. Fardood, Z. Golfar, A. Ramazani, Novel sol–gel synthesis and characterization of superparamagnetic magnesium ferrite nanoparticles using tragacanth gum as a magnetically separable photocatalyst for degradation of reactive blue 21 dye and kinetic study, J. Mater. Sci. Mater. Electron. 28 (2017) 17002–17008, https://doi.org/10.1007/s10854-017-7622-y.

[61] P. Laokul, V. Amornkitbamrung, S. Seraphin, S. Maensiri, Characterization and magnetic properties of nanocrystalline $CuFe_2O_4$, $NiFe_2O_4$, $ZnFe_2O_4$ powders prepared by the Aloe vera extract solution, Curr. Appl. Phys. 11 (2011) 101–108, https://doi.org/10.1016/j.cap.2010.06.027.

[62] F. Ansari, A. Sobhani, M. Salavati-Niasari, Simple sol-gel synthesis and characterization of new $CoTiO_3/CoFe_2O_4$ nanocomposite by using liquid glucose, maltose and starch as fuel, capping and reducing agents, J. Colloid Interface Sci. 514 (2018) 723–732, https://doi.org/10.1016/j.jcis.2017.12.083.

[63] R.S. Yadav, I. Kuřitka, J. Vilcakova, J. Havlica, J. Masilko, L. Kalina, J. Tkacz, M. Hajdúchová, V. Enev, Structural, dielectric, electrical and magnetic properties of $CuFe_2O_4$ nanoparticles synthesized by honey mediated sol–gel combustion method and annealing effect, J. Mater. Sci. Mater. Electron. 28 (2017) 6245–6261, https://doi.org/10.1007/s10854-016-6305-4.

[64] S.S. Deshmukh, A.V. Humbe, A. Kumar, R.G. Dorik, K.M. Jadhav, Urea assisted synthesis of $Ni_{1-x}Zn_xFe_2O_4$ ($0 \leq x \leq 0.8$): magnetic and Mössbauer investigations, J. Alloys Compd. 704 (2017) 227–236, https://doi.org/10.1016/j.jallcom.2017.01.176.

[65] S. V Bhandare, R. Kumar, A.V. Anupama, H.K. Choudhary, V.M. Jali, B. Sahoo, Annealing temperature dependent structural and magnetic properties of $MnFe_2O_4$ nanoparticles grown by sol-gel auto-combustion method, J. Magn. Magn Mater. 433 (2017) 29–34, https://doi.org/10.1016/j.jmmm.2017.02.040.

[66] F. Ansari, M. Salavati-Niasari, Simple sol-gel auto-combustion synthesis and characterization of lead hexaferrite by utilizing cherry juice as a novel fuel and green capping agent, Adv. Powder Technol. 27 (2016) 2025–2031, https://doi.org/10.1016/j.apt.2016.07.011.

[67] S. Javadi, S.M. Masoudpanah, A. Zakeri, Conventional versus microwave combustion synthesis of CoFe2O4 nanoparticles, J. Sol. Gel Sci. Technol. 79 (2016) 176–183, https://doi.org/10.1007/s10971-016-4010-7.

[68] F. Ebrahimi, F. Ashrafizadeh, S.R. Bakhshi, M. Farle, Synthesis and structure of strontium ferrite nanowires and nanotubes of high aspect ratio, J. Sol. Gel Sci. Technol. 77 (2016) 708–717, https://doi.org/10.1007/s10971-015-3902-2.

[69] H. Zheng, M.-G. Han, L.-J. Deng, Fabrication of $CoFe_2O_4$ ferrite nanowire arrays in porous silicon template and their local magnetic properties, Chin. Phys. B 25 (2016), 26201, https://doi.org/10.1088/1674-1056/25/2/026201.

[70] S. Komarneni, Y.D. Noh, J.Y. Kim, S.H. Kim, H. Katsuki, Solvothermal/hydrothermal synthesis of metal oxides and metal powders with and without microwaves, Zeitschrift Für Naturforsch. B. 65 (2010) 1033–1037, https://doi.org/10.1515/znb-2010-0809.

[71] W. Lojkowski, C. Leonelli, T. Chudoba, J. Wojnarowicz, A. Majcher, A. Mazurkiewicz, High-energy-low-temperature technologies for the synthesis of nanoparticles: microwaves and high pressure, Inorganics 2 (2014) 606–619, https://doi.org/10.3390/inorganics2040606.

[72] K. Byrappa, T. Adschiri, Hydrothermal technology for nanotechnology, Prog. Cryst. Growth Charact. Mater. 53 (2007) 117–166, https://doi.org/10.1016/j.pcrysgrow.2007.04.001.

[73] G. Chen, J. Wang, L. Zhou, W. Ma, D. Zhang, F. Ren, H. Yan, G. Qiu, X. Liu, A facile solvothermal synthesis and magnetic properties of $MnFe_2O_4$ spheres with tunable sizes, J. Am. Ceram. Soc. 95 (2012) 3569–3576, https://doi.org/10.1111/j.1551-2916.2012.05344.x.

[74] A. Yan, X. Liu, G. Qiu, H. Wu, R. Yi, N. Zhang, J. Xu, Solvothermal synthesis and characterization of size-controlled Fe_3O_4 nanoparticles, J. Alloys Compd. 458 (2008) 487–491, https://doi.org/10.1016/j.jallcom.2007.04.019.

[75] Y. Chen, J. Zhang, Z. Wang, Z. Zhou, Solvothermal synthesis of size-controlled monodispersed superparamagnetic iron oxide nanoparticles, Appl. Sci. 9 (2019) 5157, https://doi.org/10.3390/app9235157.

[76] H. Sun, B. Chen, X. Jiao, Z. Jiang, Z. Qin, D. Chen, Solvothermal synthesis of tunable electroactive magnetite nanorods by controlling the side reaction, J. Phys. Chem. C 116 (2012) 5476–5481, https://doi.org/10.1021/jp211986a.

[77] W.E.M. Elsayed, F.S. Al-Hazmi, L.S. Memesh, L.M. Bronstein, A novel approach for rapid green synthesis of nearly mono-disperse iron oxide magnetic nanocubes with remarkable surface magnetic anisotropy density for enhancing hyperthermia performance, Colloid Surf. A Physicochem. Eng. Asp. 529 (2017) 239–245, https://doi.org/10.1016/j.colsurfa.2017.06.008.

[78] M. Saeed, M.Z. Iqbal, W. Ren, Y. Xia, C. Liu, W.S. Khan, A. Wu, Controllable synthesis of Fe_3O_4 nanoflowers: enhanced imaging guided cancer therapy and comparison of photothermal efficiency with black-TiO_2, J. Mater. Chem. B. 6 (2018) 3800–3810, https://doi.org/10.1039/C8TB00745D.

[79] D. Kim, K. Shin, S.G. Kwon, T. Hyeon, Synthesis and biomedical applications of multifunctional nanoparticles, Adv. Mater. 30 (2018), 1802309, https://doi.org/10.1002/adma.201802309.

[80] B. Shen, Y. Ma, S. Yu, C. Ji, Smart multifunctional magnetic nanoparticle-based drug delivery system for cancer thermo-chemotherapy and intracellular imaging, ACS Appl. Mater. Interfaces 8 (2016) 24502–24508, https://doi.org/10.1021/acsami.6b09772.

[81] Y. Li, J. Shi, Hollow-structured mesoporous materials: chemical synthesis, functionalization and applications, Adv. Mater. 26 (2014) 3176–3205, https://doi.org/10.1002/adma.201305319.

[82] J. Liu, H. He, D. Xiao, S. Yin, W. Ji, S. Jiang, D. Luo, B. Wang, Y. Liu, Recent advances of plasmonic nanoparticles and their applications, Materials 11 (2018) 1833, https://doi.org/10.3390/ma11101833.

[83] M. Lucchini, E. Lizundia, S. Moser, M. Niederberger, G. Nystrom, Titania-cellulose hybrid monolith for in-flow purification of water under solar illumination, ACS Appl. Mater. Interfaces 10 (2018) 29599–29607, https://doi.org/10.1021/acsami.8b09735.

[84] P.G. Georgiou, C.S. Guy, M. Hasan, A. Ahmad, S.-J. Richards, A.N. Baker, N. V Thakkar, M. Walker, S. Pandey, N.R. Anderson, D. Grammatopoulos, M.I. Gibson, Plasmonic detection of SARS-CoV-2 spike protein with polymer-stabilized glycosylated gold nanorods, ACS Macro Lett. 11 (2022) 317–322, https://doi.org/10.1021/acsmacrolett.1c00716.

[85] S. Talebian, G.G. Wallace, A. Schroeder, F. Stellacci, J. Conde, Nanotechnology-based disinfectants and sensors for SARS-CoV-2, Nat. Nanotechnol. 15 (2020) 618–621, https://doi.org/10.1038/s41565-020-0751-0.

[86] X. Zhang, Q. Fu, H. Duan, J. Song, H. Yang, Janus nanoparticles: from fabrication to (Bio)Applications, ACS Nano 15 (2021) 6147–6191, https://doi.org/10.1021/acsnano.1c01146.

[87] S.F. Javier Requera, Hyewon Kim, Advances in Janus nanoparticles, Chim. Int. J. Chem. 67 (2013) 811–818.

[88] J. Reguera, D. Jiménez de Aberasturi, M. Henriksen-Lacey, J. Langer, A. Espinosa, B. Szczupak, C. Wilhelm, L.M. Liz-Marzán, Janus plasmonic–magnetic gold–iron oxide nanoparticles as contrast agents for multimodal imaging, Nanoscale 9 (2017) 9467–9480, https://doi.org/10.1039/C7NR01406F.

[89] H. Su, C.-A. Hurd Price, L. Jing, Q. Tian, J. Liu, K. Qian, Janus particles: design, preparation, and biomedical applications, Mater, Today Bio 4 (2019), 100033, https://doi.org/10.1016/j.mtbio.2019.100033.

[90] M. Ha, J.-H. Kim, M. You, Q. Li, C. Fan, J.-M. Nam, Multicomponent plasmonic nanoparticles: from heterostructured nanoparticles to colloidal composite nanostructures, Chem. Rev. 119 (2019) 12208–12278, https://doi.org/10.1021/acs.chemrev.9b00234.

[91] Y. Xu, X. Liu, Y. Zheng, C. Li, K.W. Kwok Yeung, Z. Cui, Y. Liang, Z. Li, S. Zhu, S. Wu, Ag_3PO_4 decorated black urchin-like defective TiO_2 for rapid and long-term bacteria-killing under visible light, Bioact. Mater. 6 (2021) 1575–1587, https://doi.org/10.1016/j.bioactmat.2020.11.013.

[92] Z. Hanani, S. Merselmiz, M. Amjoud, D. Mezzane, M. Lahcini, J. Ghanbaja, M. Spreitzer, D. Vengust, M. El Marssi, I.A. Luk'yanchuk, Z. Kutnjak, B. Rožič, M. Gouné, Novel lead-free BCZT-based ceramic with thermally-stable recovered energy density and increased energy storage efficiency, J. Materiomics 8 (2022) 873–881, https://doi.org/10.1016/j.jmat.2021.12.011.

[93] Y. Rao, L. Long, T. Jing, X. Qi, Q. Peng, X. Gong, Y. Chen, R. Xie, W. Zhong, Y. Du, Magnetic modulation of core@shell MoS_2-based flower-like multicomponent nanocomposites to improve microwave attenuation, J. Colloid Interface Sci. 608 (2022) 2387–2398, https://doi.org/10.1016/j.jcis.2021.10.138.

[94] Y. Pan, S. Zhou, C. Liu, X. Ma, J. Xing, B. Parshad, W. Li, A. Wu, R. Haag, Dendritic polyglycerol-conjugated gold nanostars for metabolism inhibition and targeted photothermal therapy in breast cancer stem cells, Adv. Healthc. Mater. 11 (2022), 2102272, https://doi.org/10.1002/adhm.202102272.

[95] M.B. Gawande, A. Goswami, T. Asefa, H. Guo, A.V. Biradar, D.-L. Peng, R. Zboril, R.S. Varma, Core–shell nanoparticles: synthesis and applications in catalysis and electrocatalysis, Chem. Soc. Rev. 44 (2015) 7540–7590, https://doi.org/10.1039/C5CS00343A.

[96] Y. Long, J. Li, L. Wu, Q. Wang, Y. Liu, X. Wang, S. Song, H. Zhang, Construction of trace silver modified core@shell structured Pt-Ni nanoframe@CeO_2 for semihydrogenation of phenylacetylene, Nano Res. 12 (2019) 869–875, https://doi.org/10.1007/s12274-018-2315-x.

[97] L. Hao, Y. Leng, L. Zeng, X. Chen, J. Chen, H. Duan, X. Huang, Y. Xiong, X. Chen, Core–shell-heterostructured magnetic–plasmonic nanoassemblies with highly retained magnetic–plasmonic activities for ultrasensitive bioanalysis in complex matrix, Adv. Sci. 7 (2020), 1902433, https://doi.org/10.1002/advs.201902433.

[98] R. Hu, M. Zheng, J. Wu, C. Li, D. Shen, D. Yang, L. Li, M. Ge, Z. Chang, W. Dong, Core-shell magnetic gold nanoparticles for magnetic field-enhanced radiophotothermal therapy in cervical cancer, Nanomaterials 7 (2017) 111, https://doi.org/10.3390/nano7050111.

[99] M. Shaban, J. Poostforooshan, A.P. Weber, Surface-initiated polymerization on unmodified inorganic semiconductor nanoparticles via surfactant-free aerosol-based synthesis toward core–shell nanohybrids with a tunable shell thickness, J. Mater. Chem. A 5 (2017) 18651–18663, https://doi.org/10.1039/C7TA04985D.

[100] T.S. Le, M. Takahashi, N. Isozumi, A. Miyazato, Y. Hiratsuka, K. Matsumura, T. Taguchi, S. Maenosono, Quick and mild isolation of intact lysosomes using magnetic–plasmonic hybrid nanoparticles, ACS Nano 16 (2022) 885–896, https://doi.org/10.1021/acsnano.1c08474.

[101] J. Shan, L. Wang, H. Yu, J. Ji, W.A. Amer, Y. Chen, G. Jing, H. Khalid, M. Akram, N.M. Abbasi, Recent progress in Fe_3O_4 based magnetic nanoparticles: from synthesis to application, Mater. Sci. Technol. 32 (2016) 602–614, https://doi.org/10.1179/1743284715Y.0000000122.

[102] V.F. Cardoso, A. Francesko, C. Ribeiro, M. Bañobre-López, P. Martins, S. Lanceros-Mendez, Advances in magnetic nanoparticles for biomedical applications, Adv. Healthc. Mater. 7 (2018), 1700845, https://doi.org/10.1002/adhm.201700845.

[103] J. Mohapatra, J. Elkins, M. Xing, D. Guragain, S.R. Mishra, J.P. Liu, Magnetic-field-induced self-assembly of $FeCo/CoFe_2O_4$ core/shell nanoparticles with tunable collective magnetic properties, Nanoscale 13 (2021) 4519–4529, https://doi.org/10.1039/D1NR00136A.

[104] Z. Tong, Z. Liao, Y. Liu, M. Ma, Y. Bi, W. Huang, Y. Ma, M. Qiao, G. Wu, Hierarchical Fe_3O_4/Fe@C@MoS_2 core-shell nanofibers for efficient microwave absorption, Carbon 179 (2021) 646–654, https://doi.org/10.1016/j.carbon.2021.04.051.

[105] S.J. Oldenburg, R.D. Averitt, S.L. Westcott, N.J. Halas, Nanoengineering of optical resonances, Chem. Phys. Lett. 288 (1998) 243–247, https://doi.org/10.1016/S0009-2614(98)00277-2.

[106] A.T. Kelly, C.S. Filgueira, D.E. Schipper, N.J. Halas, K.H. Whitmire, Gold coated iron phosphide core–shell structures, RSC Adv. 7 (2017) 25848–25854, https://doi.org/10.1039/C7RA01195D.

[107] C.S. Levin, C. Hofmann, T.A. Ali, A.T. Kelly, E. Morosan, P. Nordlander, K.H. Whitmire, N.J. Halas, Magnetic–plasmonic core–shell nanoparticles, ACS Nano 3 (2009) 1379–1388, https://doi.org/10.1021/nn900118a.

[108] S.A. Maboudi, S.A. Shojaosadati, A. Arpanaei, Synthesis and characterization of multilayered nanobiohybrid magnetic particles for biomedical applications, Mater. Des. 115 (2017) 317–324, https://doi.org/10.1016/j.matdes.2016.11.064.

[109] X. Xu, S. Lü, C. Gao, X. Bai, C. Feng, N. Gao, M. Liu, Multifunctional drug carriers comprised of mesoporous silica nanoparticles and polyamidoamine dendrimers based on layer-by-layer assembly, Mater. Des. 88 (2015) 1127–1133, https://doi.org/10.1016/j.matdes.2015.09.069.

[110] V. Kalidasan, X.L. Liu, T.S. Herng, Y. Yang, J. Ding, Bovine serum albumin-conjugated ferrimagnetic iron oxide nanoparticles to enhance the biocompatibility and magnetic hyperthermia performance, Nano-Micro Lett. 8 (2016) 80–93, https://doi.org/10.1007/s40820-015-0065-1.

[111] R. Purbia, S. Paria, Yolk/shell nanoparticles: classifications, synthesis, properties, and applications, Nanoscale 7 (2015) 19789–19873, https://doi.org/10.1039/C5NR04729C.

[112] D. Li, F. Guo, L. Qi, Gold nanoarrow-based core–shell and yolk–shell nanoparticles for surface-enhanced Raman scattering, ACS Appl. Nano Mater. 5 (2022) 126–132, https://doi.org/10.1021/acsanm.1c04203.

[113] H. Li, Q. Gao, G. Wang, B. Han, K. Xia, C. Zhou, Fabricating yolk–shell structured CoTiO3@Co3O4 nanoreactor via a simple self-template method toward high-performance peroxymonosulfate activation and organic pollutant degradation, Appl. Surf. Sci. 536 (2021), 147787, https://doi.org/10.1016/j.apsusc.2020.147787.

[114] H. Liang, J. Guo, Y. Shi, G. Zhao, S. Sun, X. Sun, Porous yolk-shell Fe/Fe_3O_4 nanoparticles with controlled exposure of highly active Fe(0) for cancer therapy, Biomaterials 268 (2021), 120530, https://doi.org/10.1016/j.biomaterials.2020.120530.

[115] M. Priebe, K.M. Fromm, Nanorattles or yolk–shell nanoparticles-What are they, how are they made, and what are they good for? Chem. Eur J. 21 (2015) 3854–3874, https://doi.org/10.1002/chem.201405285.

[116] R.G. Parkhomenko, M. Knez, Facile fabrication of gold Nanorods@Polystyrenesulfonate yolk–shell nanoparticles for spaser applications, ACS Appl. Nano Mater. 5 (2022) 4629–4633, https://doi.org/10.1021/acsanm.2c00967.

[117] Y. Xiang, Y. Huang, B. Xiao, X. Wu, G. Zhang, Magnetic yolk-shell structure of $ZnFe_2O_4$ nanoparticles for enhanced visible light photo-Fenton degradation towards antibiotics and mechanism study, Appl. Surf. Sci. 513 (2020), 145820, https://doi.org/10.1016/j.apsusc.2020.145820.

[118] J. Fang, Y. Zhang, Y. Zhou, S. Zhao, C. Zhang, H. Zhang, X. Sheng, K. Wang, Fabrication of ellipsoidal silica yolk–shell magnetic structures with extremely stable Au nanoparticles as highly reactive and recoverable catalysts, Langmuir 33 (2017) 2698–2708, https://doi.org/10.1021/acs.langmuir.6b03873.

[119] S. Yang, C. Cao, L. Peng, P. Huang, Y. Sun, F. Wei, W. Song, Spindle-shaped nanoscale yolk/shell magnetic stirring bars for heterogeneous catalysis in macro- and microscopic systems, Chem. Commun. 52 (2016) 1575–1578, https://doi.org/10.1039/C5CC09104G.

[120] Y. Qiu, D. Deng, Q. Deng, P. Wu, H. Zhang, C. Cai, Synthesis of magnetic Fe_3O_4 –Au hybrids for sensitive SERS detection of cancer cells at low abundance, J. Mater. Chem. B. 3 (2015) 4487–4495, https://doi.org/10.1039/C5TB00638D.

[121] B. Lv, Z. Sun, J. Zhang, C. Jing, Multifunctional satellite Fe3O4-Au@TiO_2 nanostructure for SERS detection and photo-reduction of Cr(VI), Colloid Surf. A Physicochem. Eng. Asp. 513 (2017) 234–240, https://doi.org/10.1016/j.colsurfa.2016.10.048.

[122] Z. Sun, J. Du, L. Yan, S. Chen, Z. Yang, C. Jing, Multifunctional Fe_3O_4@SiO_2 Au satellite structured SERS probe for charge selective detection of food dyes, ACS Appl. Mater. Interfaces 8 (2016) 3056–3062, https://doi.org/10.1021/acsami.5b10230.

[123] T. Patiño, X. Arqué, R. Mestre, L. Palacios, S. Sánchez, Fundamental aspects of enzyme-powered micro- and nanoswimmers, Acc. Chem. Res. 51 (2018) 2662–2671, https://doi.org/10.1021/acs.accounts.8b00288.

[124] J.J. Giner-Casares, J. Reguera, Directed self-assembly of inorganic nanoparticles at air/liquid interfaces, Nanoscale 8 (2016) 16589–16595, https://doi.org/10.1039/C6NR05054A.

[125] H. Ding, Y. Ma, Interactions between Janus particles and membranes, Nanoscale 4 (2012) 1116–1122, https://doi.org/10.1039/C1NR11425E.

[126] H. Fan, A. Striolo, Mechanistic study of droplets coalescence in Pickering emulsions, Soft Matter 8 (2012) 9533–9538, https://doi.org/10.1039/C2SM26416A.

[127] J. Reguera, T. Flora, N. Winckelmans, J.C. Rodríguez-Cabello, S. Bals, Self-assembly of Janus Au:Fe3O4 branched nanoparticles. From organized clusters to stimuli-responsive nanogel suprastructures, Nanoscale Adv. 2 (2020) 2525–2530, https://doi.org/10.1039/D0NA00102C.

[128] G. Jiang, Y. Huang, S. Zhang, H. Zhu, Z. Wu, S. Sun, Controlled synthesis of Au–Fe heterodimer nanoparticles and their conversion into Au–Fe_3O_4 heterostructured nanoparticles, Nanoscale 8 (2016) 17947–17952, https://doi.org/10.1039/C6NR06395K.

[129] Y. Ju, H. Zhang, J. Yu, S. Tong, N. Tian, Z. Wang, X. Wang, X. Su, X. Chu, J. Lin, Y. Ding, G. Li, F. Sheng, Y. Hou, Monodisperse Au–Fe_2C Janus nanoparticles: an attractive multifunctional material for triple-modal imaging-guided tumor photothermal therapy, ACS Nano 11 (2017) 9239–9248, https://doi.org/10.1021/acsnano.7b04461.

[130] P.S. Schattling, M.A. Ramos-Docampo, V. Salgueiriño, B. Städler, Double-fueled Janus swimmers with magnetotactic behavior, ACS Nano 11 (2017) 3973–3983, https://doi.org/10.1021/acsnano.7b00441.

[131] F. Lin, R. Doong, Bifunctional Au–Fe_3O_4 heterostructures for magnetically recyclable catalysis of nitrophenol reduction, J. Phys. Chem. C 115 (2011) 6591–6598, https://doi.org/10.1021/jp110956k.

[132] M.R. Buck, J.F. Bondi, R.E. Schaak, A total-synthesis framework for the construction of high-order colloidal hybrid nanoparticles, Nat. Chem. 4 (2012) 37–44, https://doi.org/10.1038/nchem.1195.

[133] Y. Lu, L. Dong, L.-C. Zhang, Y.-D. Su, S.-H. Yu, Biogenic and biomimetic magnetic nanosized assemblies, Nano Today 7 (2012) 297–315, https://doi.org/10.1016/j.nantod.2012.06.011.

[134] S.-M. Kralj, SilviaTI - bioinspired magnetic nanochains for medicine, Bioinspired Magnetic Nano. Med. Pharm. 13 (2021) 1262, https://doi.org/10.3390/pharmaceutics13081262.

[135] L. Kopanja, M. Tadić, S. Kralj, J. Žunić, Shape and aspect ratio analysis of anisotropic magnetic nanochains based on TEM micrographs, Ceram. Int. 44 (2018) 12340–12351, https://doi.org/10.1016/j.ceramint.2018.04.021.

[136] V. Malik, A. Pal, O. Pravaz, J.J. Crassous, S. Granville, B. Grobety, A.M. Hirt, H. Dietsch, P. Schurtenberger, Hybrid magnetic iron oxide nanoparticles with tunable field-directed self-assembly, Nanoscale 9 (2017) 14405–14413, https://doi.org/10.1039/C7NR04518B.

[137] H. Wang, Y. Yu, Y. Ssun, Q. Chen, Magnetic nanochains: a review, Nano 6 (2011) 1–17, https://doi.org/10.1142/S1793292011002305.

[138] M. Tadic, S. Kralj, L. Kopanja, Synthesis, particle shape characterization, magnetic properties and surface modification of superparamagnetic iron oxide nanochains, Mater. Char. 148 (2019) 123–133, https://doi.org/10.1016/j.matchar.2018.12.014.

[139] T. Zhang, Q. Yue, P. Pan, Y. Ren, X. Yang, X. Cheng, F.A. Alharthi, A.A. Alghamdi, Y. Deng, One-dimensional nanochains consisting of magnetic core and mesoporous aluminosilicate for use as efficient nanocatalysts, Nano Res. 14 (2021) 4197–4203, https://doi.org/10.1007/s12274-021-3383-2.

[140] C.-D. Chen HaitaoAU - Wang, JiayuanAU - Chen, WenAU - Li, DenghuiAU - Cai, MengAU - Zhou, KunTI - a general way to fabricate chain-like ferrite with ultralow conductive percolation threshold and wideband Absorbing ability, Nanomaterials 12 (2022) 1603, https://doi.org/10.3390/nano12091603.

[141] M. Ma, W. Li, Z. Tong, Y. Ma, Y. Bi, Z. Liao, J. Zhou, G. Wu, M. Li, J. Yue, X. Song, X. Zhang, NiCo2O4 nanosheets decorated on one-dimensional $ZnFe_2O_4$@SiO_2@C nanochains with high-performance microwave absorption, J. Colloid Interface Sci. 578 (2020) 58–68, https://doi.org/10.1016/j.jcis.2020.05.044.

[142] M. Qiao, J. Wang, D. Wei, J. Li, X. Lei, W. Lei, J. Wei, Q. Zhang, Influence of crystalline phase evolution of shells on microwave absorption performance of core-shell Fe_3O_4@TiO_2 nanochains, Mater, Today Nano 18 (2022), 100203, https://doi.org/10.1016/j.mtnano.2022.100203.

[143] B. Kang, M.-K. Shin, S. Han, I. Oh, E. Kim, J. Park, H.Y. Son, T. Kang, J. Jung, Y.-M. Huh, S. Haam, E.-K. Lim, Magnetic nanochain-based smart drug delivery system with remote tunable drug release by a magnetic field, BioChip J 16 (2022) 280–290, https://doi.org/10.1007/s13206-022-00072-1.

[144] A.K. Pearce, T.R. Wilks, M.C. Arno, R.K. O'Reilly, Synthesis and applications of anisotropic nanoparticles with precisely defined dimensions, Nat. Rev. Chem 5 (2021) 21–45, https://doi.org/10.1038/s41570-020-00232-7.

[145] J. Zheng, X. Cheng, H. Zhang, X. Bai, R. Ai, L. Shao, J. Wang, Gold nanorods: the most versatile plasmonic nanoparticles, Chem. Rev. 121 (2021) 13342–13453, https://doi.org/10.1021/acs.chemrev.1c00422.

[146] M. Rincón-Iglesias, I. Rodrigo, L.B. Berganza, E.S.A. Serea, F. Plazaola, S. Lanceros-Méndez, E. Lizundia, J. Reguera, Core–shell Fe_3O_4@Au nanorod-loaded gels for tunable and anisotropic magneto- and photothermia, ACS Appl. Mater. Interfaces 14 (2022) 7130–7140, https://doi.org/10.1021/acsami.1c20990.

[147] Z. Li, J. Jin, F. Yang, N. Song, Y. Yin, Coupling magnetic and plasmonic anisotropy in hybrid nanorods for mechanochromic responses, Nat. Commun. 11 (2020) 2883, https://doi.org/10.1038/s41467-020-16678-8.
[148] Z. Li, Q. Fan, Y. Yin, Colloidal self-assembly approaches to smart nanostructured materials, Chem. Rev. 122 (2022) 4976–5067, https://doi.org/10.1021/acs.chemrev.1c00482.
[149] Z. Li, F. Yang, Y. Yin, Smart materials by nanoscale magnetic assembly, Adv. Funct. Mater. 30 (2020), 1903467, https://doi.org/10.1002/adfm.201903467.
[150] Z. Li, M. Wang, X. Zhang, D. Wang, W. Xu, Y. Yin, Magnetic assembly of nanocubes for orientation-dependent photonic responses, Nano Lett. 19 (2019) 6673–6680, https://doi.org/10.1021/acs.nanolett.9b02984.
[151] D. Makovec, M. Komelj, G. Dražić, B. Belec, T. Goršak, S. Gyergyek, D. Lisjak, Incorporation of Sc into the structure of barium-hexaferrite nanoplatelets and its extraordinary finite-size effect on the magnetic properties, Acta Mater. 172 (2019) 84–91, https://doi.org/10.1016/j.actamat.2019.04.050.
[152] M. Krack, H. Hohenberg, A. Kornowski, P. Lindner, H. Weller, S. Förster, Nanoparticle-loaded magnetophoretic vesicles, J. Am. Chem. Soc. 130 (2008) 7315–7320, https://doi.org/10.1021/ja077398k.
[153] H. Oliveira, E. Pérez-Andrés, J. Thevenot, O. Sandre, E. Berra, S. Lecommandoux, Magnetic field triggered drug release from polymersomes for cancer therapeutics, J. Contr. Release 169 (2013) 165–170, https://doi.org/10.1016/j.jconrel.2013.01.013.
[154] E. Fantechi, A.G. Roca, B. Sepúlveda, P. Torruella, S. Estradé, F. Peiró, E. Coy, S. Jurga, N.G. Bastús, J. Nogués, V. Puntes, Seeded growth synthesis of Au–Fe_3O_4 heterostructured nanocrystals: rational design and mechanistic insights, Chem. Mater. 29 (2017) 4022–4035, https://doi.org/10.1021/acs.chemmater.7b00608.
[155] P. Padmanabhan, A. Kumar, S. Kumar, R.K. Chaudhary, B. Gulyás, Nanoparticles in practice for molecular-imaging applications: an overview, Acta Biomater. 41 (2016) 1–16, https://doi.org/10.1016/j.actbio.2016.06.003.
[156] H. Wei, O.T. Bruns, M.G. Kaul, E.C. Hansen, M. Barch, A. Wiśniowska, O. Chen, Y. Chen, N. Li, S. Okada, J.M. Cordero, M. Heine, C.T. Farrar, D.M. Montana, G. Adam, H. Ittrich, A. Jasanoff, P. Nielsen, M.G. Bawendi, Exceedingly small iron oxide nanoparticles as positive MRI contrast agents, Proc. Natl. Acad. Sci. USA 114 (2017) 2325, https://doi.org/10.1073/pnas.1620145114. LP – 2330.
[157] X. Tian, L. Zhang, M. Yang, L. Bai, Y. Dai, Z. Yu, Y. Pan, Functional magnetic hybrid nanomaterials for biomedical diagnosis and treatment, WIREs Nanomed. Nanobiotechnol. 10 (2018) e1476, https://doi.org/10.1002/wnan.1476.
[158] D. Kim, J. Kim, Y. Il Park, N. Lee, T. Hyeon, Recent development of inorganic nanoparticles for biomedical imaging, ACS Cent. Sci. 4 (2018) 324–336, https://doi.org/10.1021/acscentsci.7b00574.
[159] F. Li, D. Zhi, Y. Luo, J. Zhang, X. Nan, Y. Zhang, W. Zhou, B. Qiu, L. Wen, G. Liang, Core/shell Fe_3O_4/Gd_2O_3 nanocubes as T_1–T_2 dual modal MRI contrast agents, Nanoscale 8 (2016) 12826–12833, https://doi.org/10.1039/C6NR02620F.
[160] Y. Hu, S. Mignani, J.-P. Majoral, M. Shen, X. Shi, Construction of iron oxide nanoparticle-based hybrid platforms for tumor imaging and therapy, Chem. Soc. Rev. 47 (2018) 1874–1900, https://doi.org/10.1039/C7CS00657H.
[161] N. Lee, D. Yoo, D. Ling, M.H. Cho, T. Hyeon, J. Cheon, Iron oxide based nanoparticles for multimodal imaging and magnetoresponsive therapy, Chem. Rev. 115 (2015) 10637–10689, https://doi.org/10.1021/acs.chemrev.5b00112.
[162] J. Reguera, D. Jiménez De Aberasturi, N. Winckelmans, J. Langer, S. Bals, L.M. Liz-Marzán, Synthesis of Janus plasmonic-magnetic, star-sphere nanoparticles, and their application in SERS detection, Faraday Discuss 191 (2016) 47–59, https://doi.org/10.1039/C6FD00012F.
[163] X. Chen, G. Li, Q. Han, X. Li, L. Li, T. Wang, C. Wang, Rational design of branched Au–Fe_3O_4 Janus nanoparticles for simultaneous trimodal imaging and photothermal therapy of cancer cells, Chem. Eur J. 23 (2017) 17204–17208, https://doi.org/10.1002/chem.201704514.
[164] G. Song, M. Chen, Y. Zhang, L. Cui, H. Qu, X. Zheng, M. Wintermark, Z. Liu, J. Rao, Janus iron oxides@semiconducting polymer nanoparticle tracer for cell tracking by magnetic particle imaging, Nano Lett. 18 (2018) 182–189, https://doi.org/10.1021/acs.nanolett.7b03829.
[165] L.-S. Lin, X. Yang, Z. Zhou, Z. Yang, O. Jacobson, Y. Liu, A. Yang, G. Niu, J. Song, H.-H. Yang, X. Chen, Yolk–Shell nanostructure: an ideal architecture to achieve harmonious integration of magnetic–plasmonic hybrid theranostic platform, Adv. Mater. 29 (2017), 1606681, https://doi.org/10.1002/adma.201606681.
[166] B. Gleich, J. Weizenecker, Tomographic imaging using the nonlinear response of magnetic particles, Nature 435 (2005) 1214–1217, https://doi.org/10.1038/nature03808.
[167] B. Zheng, T. Vazin, P.W. Goodwill, A. Conway, A. Verma, E. Ulku Saritas, D. Schaffer, S.M. Conolly, Magnetic Particle Imaging tracks the long-term fate of in vivo neural cell implants with high image contrast, Sci. Rep. 5 (2015), 14055, https://doi.org/10.1038/srep14055.
[168] K. Jibin, M. Victor, G. Saranya, H. Santhakumar, V. Murali, K.K. Maiti, R.S. Jayasree, Nanohybrids of magnetically intercalated optical metamaterials for magnetic resonance/Raman imaging and in situ chemodynamic/photothermal therapy, ACS Appl. Bio Mater. 4 (2021) 5742–5752, https://doi.org/10.1021/acsabm.1c00510.
[169] L. Yang, T.-H. Kim, H.-Y. Cho, J. Luo, J.-M. Lee, S.-T.D. Chueng, Y. Hou, P.T.-T. Yin, J. Han, J.H. Kim, B.G. Chung, J.-W. Choi, K.-B. Lee, Hybrid graphene-gold nanoparticle-based nucleic acid conjugates for cancer-specific multimodal imaging and combined therapeutics, Adv. Funct. Mater. 31 (2021), 2006918, https://doi.org/10.1002/adfm.202006918.
[170] X. Wang, Z. Liu, R. Jin, B. Cai, S. Liu, Y. Bai, X. Chen, Multifunctional hierarchical nanohybrids perform triple antitumor theranostics in a cascaded manner for effective tumor treatment, Acta Biomater. 128 (2021) 408–419, https://doi.org/10.1016/j.actbio.2021.04.019.
[171] A.E. Dunn, D.J. Dunn, M. Lim, C. Boyer, N.T.K. Thanh, Recent developments in the design of nanomaterials for photothermal and magnetic hyperthermia induced controllable drug delivery, in: Nanoscience, the Royal Society of Chemistry, 2014, pp. 225–254, https://doi.org/10.1039/9781849737623-00225.
[172] S.K. Sharma, N. Shrivastava, F. Rossi, L.D. Tung, N.T.K. Thanh, Nanoparticles-based magnetic and photo induced hyperthermia for cancer treatment, Nano Today 29 (2019), 100795, https://doi.org/10.1016/j.nantod.2019.100795.
[173] V. Hosseini, M. Mirrahimi, A. Shakeri-Zadeh, F. Koosha, B. Ghalandari, S. Maleki, A. Komeili, S.K. Kamrava, Multimodal cancer cell therapy using Au@Fe_2O_3 core–shell nanoparticles in combination with photo-thermo-radiotherapy, Photodiagnosis Photodyn. Ther. 24 (2018) 129–135, https://doi.org/10.1016/j.pdpdt.2018.08.003.
[174] R.E. Rosensweig, Heating magnetic fluid with alternating magnetic field, J. Magn. Magn Mater. 252 (2002) 370–374, https://doi.org/10.1016/S0304-8853(02)00706-0.
[175] R.R. Wildeboer, P. Southern, Q.A. Pankhurst, On the reliable measurement of specific absorption rates and intrinsic loss parameters in magnetic hyperthermia materials, J. Phys. D Appl. Phys. 47 (2014), 495003, https://doi.org/10.1088/0022-3727/47/49/495003.
[176] R. Hergt, S. Dutz, Magnetic particle hyperthermia-biophysical limitations of a visionary tumour therapy, J. Magn. Magn Mater. 311 (2007) 187–192, https://doi.org/10.1016/j.jmmm.2006.10.1156.
[177] P. Guardia, R. Di Corato, L. Lartigue, C. Wilhelm, A. Espinosa, M. Garcia-Hernandez, F. Gazeau, L. Manna, T. Pellegrino, Water-soluble iron oxide nanocubes with high values of specific absorption rate for cancer cell hyperthermia treatment, ACS Nano 6 (2012) 3080–3091, https://doi.org/10.1021/nn2048137.
[178] B. Herrero de la Parte, I. Rodrigo, J. Gutiérrez-Basoa, S. Iturrizaga Correcher, C. Mar Medina, J.J. Echevarría-Uraga, J.A. Garcia, F. Plazaola, I. García-Alonso, Proposal of new safety limits for in vivo experiments of magnetic hyperthermia antitumor therapy, Cancers 14 (2022) 3084, https://doi.org/10.3390/cancers14133084.
[179] M.S. Carrião, A.F. Bakuzis, Mean-field and linear regime approach to magnetic hyperthermia of core-shell nanoparticles: can tiny nanostructures fight cancer? Nanoscale 8 (2016) 8363–8377, https://doi.org/10.1039/c5nr09093h.
[180] I. Hilger, In vivo applications of magnetic nanoparticle hyperthermia, Int. J. Hyperth. 29 (2013) 828–834, https://doi.org/10.3109/02656736.2013.832815.
[181] S. hyun Noh, S.H. Moon, T.H. Shin, Y. Lim, J. Cheon, Recent advances of magneto-thermal capabilities of nanoparticles: from design principles to biomedical applications, Nano Today 13 (2017) 61–76, https://doi.org/10.1016/j.nantod.2017.02.006.
[182] S. Famiani, A.P. Lagrow, M.O. Besenhard, S. Maenosono, N.T.K. Thanh, Synthesis of fine-tuning highly magnetic Fe@Fe_xO_y nanoparticles through continuous injection and a study of magnetic hyperthermia, Chem. Mater. 30 (2018) 8897–8904, https://doi.org/10.1021/acs.chemmater.8b04056.
[183] Q. Zhang, I. Castellanos-Rubio, R. Munshi, I. Orue, B. Pelaz, K.I. Gries, W.J. Parak, P. Del Pino, A. Pralle, Model driven optimization of magnetic anisotropy of exchange-coupled core-shell ferrite nanoparticles for maximal hysteretic loss, Chem. Mater. 27 (2015) 7380–7387, https://doi.org/10.1021/acs.chemmater.5b03261.
[184] J.H. Lee, J.T. Jang, J.S. Choi, S.H. Moon, S.H. Noh, J.W. Kim, J.G. Kim, I.S. Kim, K.I. Park, J. Cheon, Exchange-coupled magnetic nanoparticles for efficient heat induction, Nat. Nanotechnol. 6 (2011) 418–422, https://doi.org/10.1038/nnano.2011.95.
[185] G.C. Lavorato, R. Das, Y. Xing, J. Robles, F.J. Litterst, E. Baggio-Saitovitch, M.-H. Phan, H. Srikanth, Origin and shell-driven optimization of the heating power in core/shell bimagnetic nanoparticles, ACS Appl. Nano Mater. 3 (2020) 1755–1765, https://doi.org/10.1021/acsanm.9b02449.
[186] S. He, H. Zhang, Y. Liu, F. Sun, X. Yu, X. Li, L. Zhang, L. Wang, K. Mao, G. Wang, Y. Lin, Z. Han, R. Sabirianov, H. Zeng, Maximizing specific loss power for magnetic hyperthermia by hard-soft mixed ferrites, Small 14 (2018), 1800135, https://doi.org/10.1002/smll.201800135.
[187] F. Mohammad, G. Balaji, A. Weber, R.M. Uppu, C.S.S.R. Kumar, Influence of gold nanoshell on hyperthermia of superparamagnetic iron oxide nanoparticles, J. Phys. Chem. C 114 (2010) 19194–19201, https://doi.org/10.1021/jp105807r.
[188] A.M. Smith, M.C. Mancini, S. Nie, Bioimaging: second window for in vivo imaging, Nat. Nanotechnol. 4 (2009) 710–711, https://doi.org/10.1038/nnano.2009.326.
[189] D. Jaque, L. Martínez Maestro, B. del Rosal, P. Haro-Gonzalez, A. Benayas, J.L. Plaza, E. Martín Rodríguez, J. García Solé, Nanoparticles for photothermal therapies, Nanoscale 6 (2014) 9494–9530, https://doi.org/10.1039/C4NR00708E.
[190] A. Espinosa, R. Di Corato, J. Kolosnjaj-Tabi, P. Flaud, T. Pellegrino, C. Wilhelm, Duality of iron oxide nanoparticles in cancer therapy: amplification of

heating efficiency by magnetic hyperthermia and photothermal bimodal treatment, ACS Nano 10 (2016) 2436–2446, https://doi.org/10.1021/acsnano.5b07249.
[191] A. Espinosa, M. Bugnet, G. Radtke, S. Neveu, G.A. Botton, C. Wilhelm, A. Abou-Hassan, Can magneto-plasmonic nanohybrids efficiently combine photothermia with magnetic hyperthermia? Nanoscale 7 (2015) 18872–18877, https://doi.org/10.1039/c5nr06168g.
[192] S. Fiorito, N. Soni, N. Silvestri, R. Brescia, H. Gavilán, J.S. Conteh, B.T. Mai, T. Pellegrino, Fe_3O_4@Au@$Cu_{2-x}S$ heterostructures designed for tri-modal therapy: photo- magnetic hyperthermia and 64Cu radio-insertion, Small 18 (2022), 2200174, https://doi.org/10.1002/smll.202200174.
[193] M. Abdulla-Al-Mamun, Y. Kusumoto, T. Zannat, Y. Horie, H. Manaka, Au-ultrathin functionalized core-shell (Fe_3O_4@Au) monodispersed nanocubes for a combination of magnetic/plasmonic photothermal cancer cell killing, RSC Adv. 3 (2013) 7816–7827, https://doi.org/10.1039/c3ra21479f.
[194] R. Das, N. Rinaldi-Montes, J. Alonso, Z. Amghouz, E. Garaio, J.A. García, P. Gorria, J.A. Blanco, M.H. Phan, H. Srikanth, Boosted hyperthermia therapy by combined AC magnetic and photothermal exposures in Ag/Fe_3O_4 nanoflowers, ACS Appl. Mater. Interfaces 8 (2016) 25162–25169, https://doi.org/10.1021/acsami.6b09942.
[195] A. Espinosa, J. Reguera, A. Curcio, Á. Muñoz-Noval, C. Kuttner, A. Van De Walle, L.M. Liz-marzán, C. Wilhelm, Janus magnetic-plasmonic nanoparticles for magnetically guided and thermally activated cancer therapy, Small 16 (2020), 1904960, https://doi.org/10.1002/smll.201904960.
[196] L. Huang, L. Ao, D. Hu, W. Wang, Z. Sheng, W. Su, Magneto-plasmonic nanocapsules for multimodal-imaging and magnetically guided combination cancer therapy, Chem. Mater. 28 (2016) 5896–5904, https://doi.org/10.1021/acs.chemmater.6b02413.
[197] H.W. Yang, H.L. Liu, M.L. Li, I.W. Hsi, C.T. Fan, C.Y. Huang, Y.J. Lu, M.Y. Hua, H.Y. Chou, J.W. Liaw, C.C.M. Ma, K.C. Wei, Magnetic gold-nanorod/PNIPAAmMA nanoparticles for dual magnetic resonance and photoacoustic imaging and targeted photothermal therapy, Biomaterials 34 (2013) 5651–5660, https://doi.org/10.1016/j.biomaterials.2013.03.085.
[198] H.J. Kim, S.M. Lee, K.H. Park, C.H. Mun, Y.B. Park, K.H. Yoo, Drug-loaded gold/iron/gold plasmonic nanoparticles for magnetic targeted chemo-photothermal treatment of rheumatoid arthritis, Biomaterials 61 (2015) 95–102, https://doi.org/10.1016/j.biomaterials.2015.05.018.
[199] A. Espinosa, G.R. Castro, J. Reguera, C. Castellano, J. Castillo, J. Camarero, C. Wilhelm, M.A. García, Á. Muñoz-Noval, Photoactivated nanoscale temperature gradient detection using X-ray absorption spectroscopy as a direct nanothermometry method, Nano Lett. 21 (2021) 769–777, https://doi.org/10.1021/acs.nanolett.0c04477.
[200] J. Zhou, B. del Rosal, D. Jaque, S. Uchiyama, D. Jin, Advances and challenges for fluorescence nanothermometry, Nat. Methods 17 (2020) 967–980, https://doi.org/10.1038/s41592-020-0957-y.
[201] R. Piñol, C.D.S. Brites, R. Bustamante, A. Martínez, N.J.O. Silva, J.L. Murillo, R. Cases, J. Carrey, C. Estepa, C. Sosa, F. Palacio, L.D. Carlos, A. Millán, Joining time-resolved thermometry and magnetic-induced heating in a single nanoparticle unveils intriguing thermal properties, ACS Nano 9 (2015) 3134–3142, https://doi.org/10.1021/acsnano.5b00059.
[202] N. da Silva Moura, K.R. Bajgiran, A.T. Melvin, K.M. Dooley, J.A. Dorman, Direct probing of Fe3O4 nanoparticle surface temperatures during magnetic heating: implications for induction catalysis, ACS Appl. Nano Mater. 4 (2021) 13778–13787, https://doi.org/10.1021/acsanm.1c03168.
[203] M. Vinícius-Araújo, N. Shrivastava, A.A. Sousa-Junior, S.A. Mendanha, R.C. De Santana, A.F. Bakuzis, $Zn_xMn_{1-X}Fe_2O_4$@SiO_2:zNd^{3+} core–shell nanoparticles for low-field magnetic hyperthermia and enhanced photothermal therapy with the potential for nanothermometry, ACS Appl. Nano Mater. 4 (2021) 2190–2210, https://doi.org/10.1021/acsanm.1c00027.
[204] M.J. Mitchell, M.M. Billingsley, R.M. Haley, M.E. Wechsler, N.A. Peppas, R. Langer, Engineering precision nanoparticles for drug delivery, Nat. Rev. Drug Discov. 20 (2021) 101–124, https://doi.org/10.1038/s41573-020-0090-8.
[205] H. Guo, S. Yi, K. Feng, Y. Xia, X. Qu, F. Wan, L. Chen, C. Zhang, In situ formation of metal organic framework onto gold nanorods/mesoporous silica with functional integration for targeted theranostics, Chem. Eng. J. 403 (2021), 126432, https://doi.org/10.1016/j.cej.2020.126432.
[206] L. García-Hevia, Í. Casafont, J. Oliveira, N. Terán, M.L. Fanarraga, J. Gallo, M. Bañobre-López, Magnetic lipid nanovehicles synergize the controlled thermal release of chemotherapeutics with magnetic ablation while enabling non-invasive monitoring by MRI for melanoma theranostics, Bioact. Mater. 8 (2022) 153–164, https://doi.org/10.1016/j.bioactmat.2021.06.009.
[207] J.S. Lee, J. Feijen, Polymersomes for drug delivery: design, formation and characterization, J. Contr. Release 161 (2012) 473–483, https://doi.org/10.1016/j.jconrel.2011.10.005.
[208] C. Sanson, O. Diou, J. Thévenot, E. Ibarboure, A. Soum, A. Brûlet, S. Miraux, E. Thiaudière, S. Tan, A. Brisson, V. Dupuis, O. Sandre, S. Lecommandoux, Doxorubicin loaded magnetic polymersomes: theranostic nanocarriers for MR imaging and magneto-chemotherapy, ACS Nano 5 (2011) 1122–1140, https://doi.org/10.1021/nn102762f.
[209] S. Bhana, G. Lin, L. Wang, H. Starring, S.R. Mishra, G. Liu, X. Huang, Near-infrared-absorbing gold nanopopcorns with iron oxide cluster core for magnetically amplified photothermal and photodynamic cancer therapy, ACS Appl. Mater. Interfaces 7 (2015) 11637–11647, https://doi.org/10.1021/acsami.5b02741.
[210] E. Guisasola, L. Asín, L. Beola, J.M. de la Fuente, A. Baeza, M. Vallet-Regí, Beyond traditional hyperthermia: in vivo cancer treatment with magnetic-responsive mesoporous silica nanocarriers, ACS Appl. Mater. Interfaces 10 (2018) 12518–12525, https://doi.org/10.1021/acsami.8b02398.
[211] S.O. Kelley, C.A. Mirkin, D.R. Walt, R.F. Ismagilov, M. Toner, E.H. Sargent, Advancing the speed, sensitivity and accuracy of biomolecular detection using multi-length-scale engineering, Nat. Nanotechnol. 9 (2014) 969–980, https://doi.org/10.1038/nnano.2014.261.
[212] F. Qiu, X. Gan, B. Jiang, R. Yuan, Y. Xiang, Electrode immobilization-free and sensitive electrochemical sensing of thrombin via magnetic nanoparticle-decorated DNA polymers, Sens. Actuators B Chem. 331 (2021), 129395, https://doi.org/10.1016/j.snb.2020.129395.
[213] J. Lee, O. Adegoke, E.Y. Park, High-performance biosensing systems based on various nanomaterials as signal transducers, Biotechnol. J. 14 (2019), 1800249, https://doi.org/10.1002/biot.201800249.
[214] T. Ozer, B.J. Geiss, C.S. Henry, Review-chemical and biological sensors for viral detection, J. Electrochem. Soc. 167 (2020), 37523, https://doi.org/10.1149/2.0232003jes.
[215] J. Lee, K. Takemura, C.N. Kato, T. Suzuki, E.Y. Park, Binary nanoparticle graphene hybrid structure-based highly sensitive biosensing platform for norovirus-like particle detection, ACS Appl. Mater. Interfaces 9 (2017) 27298–27304, https://doi.org/10.1021/acsami.7b07012.
[216] J. Lee, M. Morita, K. Takemura, E.Y. Park, A multi-functional gold/iron-oxide nanoparticle-CNT hybrid nanomaterial as virus DNA sensing platform, Biosens. Bioelectron. 102 (2018) 425–431, https://doi.org/10.1016/j.bios.2017.11.052.
[217] H. Bin Seo, M.B. Gu, Aptamer-based sandwich-type biosensors, J. Biol. Eng. 11 (2017) 11, https://doi.org/10.1186/s13036-017-0054-7.
[218] C.-H. Wang, C.-P. Chang, G.-B. Lee, Integrated microfluidic device using a single universal aptamer to detect multiple types of influenza viruses, Biosens. Bioelectron. 86 (2016) 247–254, https://doi.org/10.1016/j.bios.2016.06.071.
[219] Y. Watanabe, T. Ito, M.S. Ibrahim, Y. Arai, K. Hotta, H.V.M. Phuong, N.L.K. Hang, L.Q. Mai, K. Soda, M. Yamaoka, E.D. Poetranto, L. Wulandari, H. Hiramatsu, T. Daidoji, R. Kubota-Koketsu, N. Sriwilaijaroen, T. Nakaya, Y. Okuno, T. Takahashi, T. Suzuki, T. Ito, H. Hotta, T. Yamashiro, T. Hayashi, K. Morita, K. Ikuta, Y. Suzuki, A novel immunochromatographic system for easy-to-use detection of group 1 avian influenza viruses with acquired human-type receptor binding specificity, Biosens. Bioelectron. 65 (2015) 211–219, https://doi.org/10.1016/j.bios.2014.10.036.
[220] J. Lin, R. Wang, P. Jiao, Y. Li, Y. Li, M. Liao, Y. Yu, M. Wang, An impedance immunosensor based on low-cost microelectrodes and specific monoclonal antibodies for rapid detection of avian influenza virus H5N1 in chicken swabs, Biosens. Bioelectron. 67 (2015) 546–552, https://doi.org/10.1016/j.bios.2014.09.037.
[221] M. Sayhi, O. Ouerghi, K. Belgacem, M. Arbi, Y. Tepeli, A. Ghram, Ü. Anik, L. Österlund, D. Laouini, M.F. Diouani, Electrochemical detection of influenza virus H9N2 based on both immunomagnetic extraction and gold catalysis using an immobilization-free screen printed carbon microelectrode, Biosens. Bioelectron. 107 (2018) 170–177, https://doi.org/10.1016/j.bios.2018.02.018.
[222] A. Dona, I.S. Arvanitoyannis, Health risks of genetically modified foods, Crit. Rev. Food Sci. Nutr. 49 (2009) 164–175, https://doi.org/10.1080/10408390701855993.
[223] Z. Zhang, X. Wang, X. Yang, A sensitive choline biosensor using Fe_3O_4 magnetic nanoparticles as peroxidase mimics, Analyst 136 (2011) 4960–4965, https://doi.org/10.1039/C1AN15602K.
[224] Y. Ye, S. Mao, S. He, X. Xu, X. Cao, Z. Wei, S. Gunasekaran, Ultrasensitive electrochemical genosensor for detection of CaMV35S gene with Fe_3O_4-Au@Ag nanoprobe, Talanta 206 (2020), 120205, https://doi.org/10.1016/j.talanta.2019.120205.
[225] F. Li, Z. Yu, X. Han, R.Y. Lai, Electrochemical aptamer-based sensors for food and water analysis: a review, Anal. Chim. Acta 1051 (2019) 1–23, https://doi.org/10.1016/j.aca.2018.10.058.
[226] A. Abbaspour, F. Norouz-Sarvestani, A. Noori, N. Soltani, Aptamer-conjugated silver nanoparticles for electrochemical dual-aptamer-based sandwich detection of staphylococcus aureus, Biosens. Bioelectron. 68 (2015) 149–155, https://doi.org/10.1016/j.bios.2014.12.040.
[227] S.-J. Bu, K.-Y. Wang, H.-S. Bai, Y. Leng, C.-J. Ju, C.-Y. Wang, W.-S. Liu, J.-Y. Wan, Immunoassay for pathogenic bacteria using platinum nanoparticles and a hand-held hydrogen detector as transducer. Application to the detection of Escherichia coli O157:H7, Microchim. Acta 186 (2019) 296, https://doi.org/10.1007/s00604-019-3409-6.
[228] H. Bai, S. Bu, C. Wang, C. Ma, Z. Li, Z. Hao, J. Wan, Y. Han, Sandwich immunoassay based on antimicrobial peptide-mediated nanocomposite pair for determination of Escherichia coli O157:H7 using personal glucose meter as readout, Microchim. Acta 187 (2020) 220, https://doi.org/10.1007/s00604-020-4200-4.
[229] A. Csordas, A.E. Gerdon, J.D. Adams, J. Qian, S.S. Oh, Y. Xiao, H.T. Soh, Detection of proteins in serum by micromagnetic aptamer PCR (MAP) technology, Angew. Chem. Int. Ed. 49 (2010) 355–358, https://doi.org/10.1002/anie.200904846.
[230] J. Zheng, M. Zhang, X. Guo, J. Wang, J. Xu, Boronic acid functionalized magnetic composites with sandwich-like nanostructures as a novel matrix for

PDGF detection, Sens. Actuators B Chem. 250 (2017) 8–16, https://doi.org/10.1016/j.snb.2017.04.157.
[231] F.H. Cincotto, D.A.S. Carvalho, T.C. Canevari, H.E. Toma, O. Fatibello-Filho, F.C. Moraes, A nano-magnetic electrochemical sensor for the determination of mood disorder related substances, RSC Adv. 8 (2018) 14040–14047, https://doi.org/10.1039/C8RA01857J.
[232] D. Nunes da Silva, H. Leijoto de Oliveira, K.B. Borges, A.C. Pereira, Sensitive determination of 17β-estradiol using a magneto sensor based on magnetic molecularly imprinted polymer, Electroanalysis 33 (2021) 506–514, https://doi.org/10.1002/elan.202060223.
[233] Y. Lu, X. Liang, C. Niyungeko, J. Zhou, J. Xu, G. Tian, A review of the identification and detection of heavy metal ions in the environment by voltammetry, Talanta 178 (2018) 324–338, https://doi.org/10.1016/j.talanta.2017.08.033.
[234] P. Miao, Y. Tang, L. Wang, DNA modified Fe_3O_4@Au magnetic nanoparticles as selective probes for simultaneous detection of heavy metal ions, ACS Appl. Mater. Interfaces 9 (2017) 3940–3947, https://doi.org/10.1021/acsami.6b14247.
[235] N.C. Lindquist, P. Nagpal, K.M. McPeak, D.J. Norris, S.-H. Oh, Engineering metallic nanostructures for plasmonics and nanophotonics, Rep. Prog. Phys. 75 (2012), 36501, https://doi.org/10.1088/0034-4885/75/3/036501.
[236] J. Reguera, J. Langer, D. Jiménez De Aberasturi, Liz-Marzán, Anisotropic metal nanoparticles for surface enhanced Raman scattering, Chem. Soc. Rev. 46 (2017) 3866–3885, https://doi.org/10.1039/C7CS00158D.
[237] D. Cialla, A. März, R. Böhme, F. Theil, K. Weber, M. Schmitt, J. Popp, Surface-enhanced Raman spectroscopy (SERS): progress and trends, Anal. Bioanal. Chem. 403 (2012) 27–54, https://doi.org/10.1007/s00216-011-5631-x.
[238] S. Schlücker, Surface-Enhanced Raman Spectroscopy: concepts and chemical applications, Angew. Chem. Int. Ed. 53 (2014) 4756–4795, https://doi.org/10.1002/anie.201205748.
[239] E.C. Le Ru, E. Blackie, M. Meyer, P.G. Etchegoin, Surface Enhanced Raman Scattering enhancement factors: a comprehensive study, J. Phys. Chem. C 111 (2007) 13794–13803, https://doi.org/10.1021/jp0687908.
[240] H. Lai, F. Xu, L. Wang, A review of the preparation and application of magnetic nanoparticles for surface-enhanced Raman scattering, J. Mater. Sci. 53 (2018) 8677–8698, https://doi.org/10.1007/s10853-018-2095-9.
[241] D. Song, R. Yang, F. Long, A. Zhu, Applications of magnetic nanoparticles in surface-enhanced Raman scattering (SERS) detection of environmental pollutants, J. Environ. Sci. 80 (2019) 14–34, https://doi.org/10.1016/j.jes.2018.07.004.
[242] J.F. Li, Y.J. Zhang, S.Y. Ding, R. Panneerselvam, Z.Q. Tian, Core-shell nanoparticle-enhanced Raman spectroscopy, Chem. Rev. 117 (2017) 5002–5069, https://doi.org/10.1021/acs.chemrev.6b00596.
[243] B. Kalska-Szostko, U. Wykowska, D. Satuła, Magnetic nanoparticles of core-shell structure, Colloid Surf. A Physicochem. Eng. Asp. 481 (2015) 527–536, https://doi.org/10.1016/j.colsurfa.2015.05.040.
[244] S.M. Silva, R. Tavallaie, L. Sandiford, R.D. Tilley, J.J. Gooding, S. Moraes Silva, R. Tavallaie, L. Sandiford, R.D. Tilley, J.J. Gooding, Gold coated magnetic nanoparticles: from preparation to surface modification for analytical and biomedical applications, Chem. Commun. 52 (2016) 7528–7540, https://doi.org/10.1039/c6cc03225g.
[245] D.A. Wheeler, S.A. Adams, T. López-Luke, A. Torres-Castro, J.Z. Zhang, Magnetic Fe_3O_4-Au core-shell nanostructures for surface enhanced Raman scattering, Ann. Phys. 524 (2012) 670–679, https://doi.org/10.1002/andp.201200161.
[246] Q.-H.H. Guo, C.-J.J. Zhang, C. Wei, M.-M.M. Xu, Y.-X.X. Yuan, R.-A.A. Gu, J.-L.L. Yao, Controlling dynamic SERS hot spots on a monolayer film of Fe_3O_4@Au nanoparticles by a magnetic field, Spectrochim. Acta Part a-Molecular Biomol. Spectrosc. 152 (2016) 336–342, https://doi.org/10.1016/j.saa.2015.07.092.
[247] Y. Xie, T. Chen, Y. Guo, Y. Cheng, H. Qian, W. Yao, Rapid SERS detection of acid orange II and brilliant blue in food by using Fe_3O_4@Au core–shell substrate, Food Chem. 270 (2019) 173–180, https://doi.org/10.1016/j.foodchem.2018.07.065.
[248] Y. Pang, N. Wan, L. Shi, C. Wang, Z. Sun, R. Xiao, S. Wang, Dual-recognition surface-enhanced Raman scattering(SERS)biosensor for pathogenic bacteria detection by using vancomycin-SERS tags and aptamer-Fe_3O_4@Au, Anal. Chim. Acta 1077 (2019) 288–296, https://doi.org/10.1016/j.aca.2019.05.059.
[249] J. Du, C. Jing, Preparation of Fe_3O_4@Ag SERS substrate and its application in environmental Cr(VI) analysis, J. Colloid Interface Sci. 358 (2011) 54–61, https://doi.org/10.1016/j.jcis.2011.02.044.
[250] Y. Pang, C. Wang, J. Wang, Z. Sun, R. Xiao, S. Wang, Fe_3O_4@Ag magnetic nanoparticles for microRNA capture and duplex-specific nuclease signal amplification based SERS detection in cancer cells, Biosens. Bioelectron. 79 (2016) 574–580, https://doi.org/10.1016/j.bios.2015.12.052.
[251] J. Du, J. Cui, C. Jing, Rapid in situ identification of arsenic species using a portable Fe_3O_4@Ag SERS sensor, Chem. Commun. 50 (2014) 347–349, https://doi.org/10.1039/c3cc46920d.
[252] W. Zhao, D. Zhang, T. Zhou, J. Huang, Y. Wang, B. Li, L. Chen, J. Yang, Y. Liu, Aptamer-conjugated magnetic Fe_3O_4@Au core-shell multifunctional nanoprobe: a three-in-one aptasensor for selective capture, sensitive SERS detection and efficient near-infrared light triggered photothermal therapy of Staphylococcus aureus, Sens. Actuators B Chem. 350 (2022), 130879, https://doi.org/10.1016/j.snb.2021.130879.
[253] H. He, D.-W. Sun, H. Pu, L. Huang, Bridging Fe_3O_4@Au nanoflowers and Au@Ag nanospheres with aptamer for ultrasensitive SERS detection of aflatoxin B1, Food Chem. 324 (2020), 126832, https://doi.org/10.1016/j.foodchem.2020.126832.
[254] Z. Xu, Y. Hou, S. Sun, Magnetic core/shell Fe_3O_4/Au and Fe_3O_4/Au/Ag nanoparticles with tunable plasmonic properties, J. Am. Chem. Soc. 129 (2007) 8698–8699, https://doi.org/10.1021/ja073057v.
[255] Q.-H. Han, San-Yang, Guo, M.-M. Xu, Y.-X. Yuan, L.-M. Shen, J.-L. Yao, W. Liu, R.-A. Gu, Tunable fabrication on iron oxide/Au/Ag nanostructures for surface enhanced Raman spectroscopy and magnetic enrichment, J. Colloid Interface Sci. 378 (2012) 51–57.
[256] R. Bardhan, S. Mukherjee, N.A. Mirin, S.D. Levit, P. Nordlander, N.J. Halas, Nanosphere-in-a-nanoshell: a simple nanomatryushka, J. Phys. Chem. C 114 (2010) 7378–7383, https://doi.org/10.1021/jp9095387.
[257] Z. Yu, M.F. Grasso, X. Cui, R.N. Silva, P. Zhang, Sensitive and label-free SERS detection of single-stranded DNA assisted by silver nanoparticles and gold-coated magnetic nanoparticles, ACS Appl. Bio Mater. 3 (2020) 2626–2632, https://doi.org/10.1021/acsabm.9b01218.
[258] J. Shen, Y. Zhu, X. Yang, J. Zong, C. Li, Multifunctional Fe_3O_4@Ag/SiO_2/Au core-shell microspheres as a novel SERS-activity label via long-range plasmon coupling, Langmuir 29 (2013) 690–695, https://doi.org/10.1021/la304048v.
[259] C. Wang, S. Xu, K. Zhang, M. Li, Q. Li, R. Xiao, S. Wang, Streptomycin-modified Fe_3O_4–Au@Ag core–satellite magnetic nanoparticles as an effective antibacterial agent, J. Mater. Sci. 52 (2017) 1357–1368, https://doi.org/10.1007/s10853-016-0430-6.
[260] J. Li, S. Wang, L. Chen, W. Lu, A. Wu, J. Choo, L. Chen, FITC functionalized magnetic core-shell Fe3O4/Ag hybrid nanoparticle for selective determination of molecular biothiols, Sensor. Actuator. B Chem. 193 (2014) 857–863, https://doi.org/10.1016/j.snb.2013.12.053.
[261] J. Du, J. Xu, Z. Sun, C. Jing, Au nanoparticles grafted on Fe_3O_4 as effective SERS substrates for label-free detection of the 16 EPA priority polycyclic aromatic hydrocarbons, Anal. Chim. Acta 915 (2016) 81–89, https://doi.org/10.1016/j.aca.2016.02.009.
[262] Z. Sun, J. Du, B. Lv, C. Jing, Satellite Fe_3O_4@SiO_2-Au SERS probe for trace Hg^{2+} detection, RSC Adv. 6 (2016) 73040–73044, https://doi.org/10.1039/c6ra15044f.
[263] F. Hu, H. Lin, Z. Zhang, F. Liao, M. Shao, Y. Lifshitz, S.-T.T. Lee, Smart liquid SERS substrates based on Fe3O4/Au nanoparticles with reversibly tunable enhancement factor for practical quantitative detection, Sci. Rep. 4 (2014) srep07204, https://doi.org/10.1038/srep07204.
[264] M. Chen, W. Luo, Z. Zhang, F. Zhu, S. Liao, H. Yang, X. Chen, Sensitive surface enhanced Raman spectroscopy (SERS) detection of methotrexate by core-shell-satellite magnetic microspheres, Talanta 171 (2017) 152–158, https://doi.org/10.1016/j.talanta.2017.04.072.
[265] Y. Hu, Y. Sun, Stable magnetic hot spots for simultaneous concentration and ultrasensitive surface-enhanced Raman scattering detection of solution analytes, J. Phys. Chem. C 116 (2012) 13329–13335, https://doi.org/10.1021/jp303775m.
[266] T. Xue, S. Wang, G. Ou, Y. Li, H. Ruan, Z. Li, Y. Ma, R. Zou, J. Qiu, Z. Shen, A. Wu, Detection of circulating tumor cells based on improved SERS-active magnetic nanoparticles, Anal. Methods 11 (2019) 2918–2928, https://doi.org/10.1039/c9ay00646j.
[267] A. Michałowska, J. Krajczewski, A. Kudelski, Magnetic iron oxide cores with attached gold nanostructures coated with a layer of silica: an easily, homogeneously deposited new nanomaterial for surface-enhanced Raman scattering measurements, Spectrochim. Acta Part A Mol. Biomol. Spectrosc. 277 (2022), 121266, https://doi.org/10.1016/j.saa.2022.121266.
[268] H. Zhang, H. Lai, X. Wu, G. Li, Y. Hu, $CoFe_2O_4$@HNTs/AuNPs substrate for rapid magnetic solid-phase extraction and efficient SERS detection of complex samples all-in-one, Anal. Chem. 92 (2020) 4607–4613, https://doi.org/10.1021/acs.analchem.0c00144.
[269] C. Wang, P. Li, J. Wang, Z. Rong, Y. Pang, J. Xu, P. Dong, R. Xiao, S. Wang, Polyethylenimine-interlayered core-shell-satellite 3D magnetic microspheres as versatile SERS substrates, Nanoscale 7 (2015) 18694–18707, https://doi.org/10.1039/c5nr04977f.
[270] T.T. Nguyen, S. Lau-Truong, F. Mammeri, S. Ammar, Star-shaped $Fe_{3-x}O_4$-Au core-shell nanoparticles: from synthesis to SERS application, Nanomaterials 10 (2020) 294, https://doi.org/10.3390/nano10020294.
[271] P. Quaresma, I. Osorio, G. Doria, P.A.P.A. Carvalho, A.A. Pereira, J. Langer, J.P. Araujo, I. Pastoriza-Santos, L.M. Liz-Marzán, R. Franco, P.V. Baptista, E.E. Pereira, I. Osório, G. Dória, P.A.P.A. Carvalho, A.A. Pereira, J. Langer, J.P. Araújo, I. Pastoriza-Santos, L.M. Liz-Marzán, R. Franco, P.V. Baptista, E.E. Pereira, Star-shaped magnetite@gold nanoparticles for protein magnetic separation and SERS detection, RSC Adv. 4 (2014) 3659–3667, https://doi.org/10.1039/c3ra46762g.
[272] Y. Ye, J. Chen, Q. Ding, D. Lin, R. Dong, L. Yang, J. Liu, Sea-urchin-like Fe_3O_4@C@Ag particles: an efficient SERS substrate for detection of organic pollutants, Nanoscale 5 (2013) 5887, https://doi.org/10.1039/c3nr01273e.
[273] C. Wang, J. Wang, P. Li, Z. Rong, X. Jia, Q. Ma, R. Xiao, S. Wang, Sonochemical synthesis of highly branched flower-like Fe_3O_4@SiO_2@Ag microcomposites and their application as versatile SERS substrates, Nanoscale 8 (2016) 19816–19828, https://doi.org/10.1039/C6NR07295J.
[274] Q. Gao, A. Zhao, Z. Gan, W. Tao, D. Li, M. Zhang, H. Guo, D. Wang, H. Sun, R. Mao, E. Liu, Facile fabrication and growth mechanism of 3D flower-like

Fe_3O_4 nanostructures and their application as SERS substrates, CrystEngComm 14 (2012) 4834, https://doi.org/10.1039/c2ce25198a.
[275] E.E. Bedford, C. Méthivier, C.-M. Pradier, F. Gu, S. Boujday, Nanostructured and spiky gold shell growth on magnetic particles for SERS applications, Nanomaterials 10 (2020) 2136, https://doi.org/10.3390/nano10112136.
[276] Q. He, A. Zhao, L. Li, H. Sun, D. Wang, H. Guo, M. Sun, P. Chen, Fabrication of Fe_3O_4@SiO_2@Ag magnetic−plasmonic nanospindles as highly efficient SERS active substrates for label-free detection of pesticides, New J. Chem. 41 (2017) 1582−1590, https://doi.org/10.1039/C6NJ03335K.
[277] Z. Wang, L. Wu, F. Wang, Z. Jiang, B. Shen, Durian-like multi-functional Fe_3O_4−Au nanoparticles: synthesis, characterization and selective detection of benzidine, J. Mater. Chem. A 1 (2013) 9746, https://doi.org/10.1039/c3ta11477e.
[278] X. Zhang, C. Niu, Y. Wang, S. Zhou, J. Liu, Gel-limited synthesis of dumbbell-like Fe_3O_4-Ag composite microspheres and their SERS applications, Nanoscale 6 (2014) 12618−12625, https://doi.org/10.1039/c4nr03301a.
[279] Q. Ding, H. Zhou, H. Zhang, Y. Zhang, G. Wang, H. Zhao, 3D Fe_3O_4@Au@Ag nanoflowers assembled magnetoplasmonic chains for in situ SERS monitoring of plasmon-assisted catalytic reactions, J. Mater. Chem. A 4 (2016) 8866−8874, https://doi.org/10.1039/C6TA02264B.
[280] S. Tang, Y. Li, H. Huang, P. Li, Z. Guo, Q. Luo, Z. Wang, P.K. Chu, J. Li, X.-F. Yu, Efficient enrichment and self-assembly of hybrid nanoparticles into removable and magnetic SERS substrates for sensitive detection of environmental pollutants, ACS Appl. Mater. Interfaces 9 (2017) 7472−7480, https://doi.org/10.1021/acsami.6b16141.
[281] S. Yu, Z. Liu, H. Li, J. Zhang, X. Yuan, X. Jia, Y. Wu, Combination of a graphene SERS substrate and magnetic solid phase micro-extraction used for the rapid detection of trace illegal additives, Analyst 143 (2018) 883−890, https://doi.org/10.1039/C7AN01547J.
[282] T. Yang, X. Guo, H. Wang, S. Fu, J. Yu, Y. Wen, H. Yang, Au dotted magnetic network nanostructure and its application for on-site monitoring femtomolar level pesticide, Small 10 (2014) 1325−1331, https://doi.org/10.1002/smll.201302604.
[283] L. Zhang, Z. Bao, X. Yu, P. Dai, J. Zhu, M. Wu, G. Li, X. Liu, Z. Sun, C. Chen, Rational design of α-Fe2O3/reduced graphene oxide composites: rapid detection and effective removal of organic pollutants, ACS Appl. Mater. Interfaces 8 (2016) 6431−6438, https://doi.org/10.1021/acsami.5b11292.
[284] L. Yang, J. Hu, L. He, J. Tang, Y. Zhou, J. Li, K. Ding, One-pot synthesis of multifunctional magnetic N-doped graphene composite for SERS detection, adsorption separation and photocatalytic degradation of Rhodamine 6G, Chem. Eng. J. 327 (2017) 694−704, https://doi.org/10.1016/j.cej.2017.06.162.
[285] S. Scaramuzza, S. Polizzi, V. Amendola, Magnetic tuning of SERS hot spots in polymer-coated magnetic−plasmonic iron−silver nanoparticles, Nanoscale Adv. 1 (2019) 2681−2689, https://doi.org/10.1039/C9NA00143C.
[286] N. Jiang, T. Zhu, Y. Hu, Competitive aptasensor with gold nanoparticle dimers and magnetite nanoparticles for SERS-based determination of thrombin, Microchim. Acta 186 (2019) 747, https://doi.org/10.1007/s00604-019-3787-9.
[287] M.T. Alula, P. Lemmens, L. Bo, D. Wulferding, J. Yang, H. Spende, Preparation of silver nanoparticles coated ZnO/Fe3O4 composites using chemical reduction method for sensitive detection of uric acid via surface-enhanced Raman spectroscopy, Anal. Chim. Acta 1073 (2019) 62−71, https://doi.org/10.1016/j.aca.2019.04.061.
[288] V. Maurer, A. Zarinwall, Z. Wang, S. Wundrack, N. Wundrack, D. Ag Seleci, V. Helm, D. Otenko, C. Frank, F. Schaper, R. Stosch, G. Garnweitner, All-in-one superparamagnetic and SERS-active niosomes for dual-targeted in vitro detection of breast cancer cells, Sens. Diagnostic 1 (2022) 469−484, https://doi.org/10.1039/D2SD00020B.
[289] S. Yu, Z. Liu, W. Wang, L. Jin, W. Xu, Y. Wu, Disperse magnetic solid phase microextraction and surface enhanced Raman scattering (Dis-MSPME-SERS) for the rapid detection of trace illegally chemicals, Talanta 178 (2018) 498−506, https://doi.org/10.1016/j.talanta.2017.09.054.
[290] Z.H. Li, J.H. Bai, X. Zhang, J.M. Lv, C.S. Fan, Y.M. Zhao, Z.L. Wu, H.J. Xu, Facile synthesis of Au nanoparticle-coated Fe_3O_4 magnetic composite nanospheres and their application in SERS detection of malachite green, Spectrochim. Acta Part A Mol. Biomol. Spectrosc. 241 (2020), 118532, https://doi.org/10.1016/j.saa.2020.118532.
[291] S. Carrasco, E. Benito-Peña, F. Navarro-Villoslada, J. Langer, M.N. Sanz-Ortiz, J. Reguera, L.M. Liz-Marzán, M.C. Moreno-Bondi, Multibranched gold−mesoporous silica nanoparticles coated with a molecularly imprinted polymer for label-free antibiotic surface-enhanced Raman scattering analysis, Chem. Mater. 28 (2016) 7947−7954, https://doi.org/10.1021/acs.chemmater.6b03613.
[292] X. Ma, H. Liu, S. Wen, Q. Xie, L. Li, J. Jin, X. Wang, B. Zhao, W. Song, Ultrasensitive SERS detection, rapid selective adsorption and degradation of cationic dyes on multifunctional magnetic metal-organic framework-based composite, Nanotechnology 31 (2020), 315501, https://doi.org/10.1088/1361-6528/ab8a8f.
[293] J. Neng, J. Tan, K. Jia, P. Sun, A fast and cost-effective detection of melamine by Surface Enhanced Raman Spectroscopy using a novel hydrogen bonding-assisted supramolecular matrix and gold-coated magnetic nanoparticles, Appl. Sci. 7 (2017) 475, https://doi.org/10.3390/app7050475.
[294] J. He, G. Li, Y. Hu, Aptamer recognition induced target-bridged strategy for proteins detection based on magnetic chitosan and silver/chitosan nanoparticles using Surface-Enhanced Raman Spectroscopy, Anal. Chem. 87 (2015) 11039−11047, https://doi.org/10.1021/acs.analchem.5b03049.
[295] X. Ma, Y. Liu, N. Zhou, N. Duan, S. Wu, Z. Wang, SERS aptasensor detection of: Salmonella typhimurium using a magnetic gold nanoparticle and gold nanoparticle based sandwich structure, Anal. Methods 8 (2016) 8099−8105, https://doi.org/10.1039/c6ay02623k.
[296] L.W. Yap, H. Chen, Y. Gao, K. Petkovic, Y. Liang, K.J. Si, H. Wang, Z. Tang, Y. Zhu, W. Cheng, Bifunctional plasmonic-magnetic particles for an enhanced microfluidic SERS immunoassay, Nanoscale 9 (2017) 7822−7829, https://doi.org/10.1039/c7nr01511a.
[297] Y. Huang, A.N. Fulton, A.A. Keller, Simultaneous removal of PAHs and metal contaminants from water using magnetic nanoparticle adsorbents, Sci. Total Environ. 571 (2016) 1029−1036, https://doi.org/10.1016/j.scitotenv.2016.07.093.
[298] Y. Shan, Y. Yang, Y. Cao, Z. Huang, Facile solvothermal synthesis of Ag/Fe_3O_4 nanocomposites and their SERS applications in on-line monitoring of pesticide contaminated water, RSC Adv. 5 (2015) 102610−102618, https://doi.org/10.1039/C5RA17606A.
[299] H. Li, Q. Chen, M. Mehedi Hassan, X. Chen, Q. Ouyang, Z. Guo, J. Zhao, A magnetite/PMAA nanospheres-targeting SERS aptasensor for tetracycline sensing using mercapto molecules embedded core/shell nanoparticles for signal amplification, Biosens. Bioelectron. 92 (2017) 192−199, https://doi.org/10.1016/j.bios.2017.02.009.
[300] K. Yang, Y. Hu, N. Dong, A novel biosensor based on competitive SERS immunoassay and magnetic separation for accurate and sensitive detection of chloramphenicol, Biosens. Bioelectron. 80 (2016) 373−377, https://doi.org/10.1016/j.bios.2016.01.064.
[301] C. Yuen, Magnetic field enriched surface enhanced resonance Raman spectroscopy for early malaria diagnosis, J. Biomed. Opt. 17 (2012), 017005, https://doi.org/10.1117/1.jbo.17.1.017005.
[302] B.-H. Jun, M.S. Noh, J. Kim, G. Kim, H. Kang, M.-S. Kim, Y.-T. Seo, J. Baek, J.-H. Kim, J. Park, S. Kim, Y.-K. Kim, T. Hyeon, M.-H. Cho, D.H. Jeong, Y.-S. Lee, Multifunctional silver-embedded magnetic nanoparticles as SERS nanoprobes and their applications, Small 6 (2010) 119−125, https://doi.org/10.1002/smll.200901459.
[303] T. Yang, X. Guo, Y. Wu, H. Wang, S. Fu, Y. Wen, H. Yang, Facile and label-free detection of lung cancer biomarker in urine by magnetically assisted surface-enhanced Raman scattering, ACS Appl. Mater. Interfaces 6 (2014) 20985−20993, https://doi.org/10.1021/am5057536.
[304] L. Wu, X. Xiao, K. Chen, W. Yin, Q. Li, P. Wang, Z. Lu, J. Ma, H. Han, Ultrasensitive SERS detection of Bacillus thuringiensis special gene based on Au@Ag NRs and magnetic beads, Biosens. Bioelectron. 92 (2017) 321−327, https://doi.org/10.1016/j.bios.2016.11.005.
[305] X. Kong, Q. Yu, Z. Lv, X. Du, Tandem assays of protein and glucose with functionalized core/shell particles based on magnetic separation and Surface-Enhanced Raman Scattering, Small 9 (2013) 3259−3264, https://doi.org/10.1002/smll.201203248.
[306] K. Yang, Y. Hu, N. Dong, G. Zhu, T. Zhu, N. Jiang, A novel SERS-based magnetic aptasensor for prostate specific antigen assay with high sensitivity, Biosens. Bioelectron. 94 (2017) 286−291, https://doi.org/10.1016/j.bios.2017.02.048.
[307] L. Zhang, J. Xu, L. Mi, H. Gong, S. Jiang, Q. Yu, Multifunctional magnetic-plasmonic nanoparticles for fast concentration and sensitive detection of bacteria using SERS, Biosens. Bioelectron. 31 (2012) 130−136, https://doi.org/10.1016/j.bios.2011.10.006.
[308] R. Prucek, A. Panáček, Ž. Gajdová, R. Večeřová, L. Kvítek, J. Gallo, M. Kolář, Specific detection of Staphylococcus aureus infection and marker for Alzheimer disease by surface enhanced Raman spectroscopy using silver and gold nanoparticle-coated magnetic polystyrene beads, Sci. Rep. 11 (2021) 6240, https://doi.org/10.1038/s41598-021-84793-7.
[309] Q. An, P. Zhang, J.M. Li, W.F. Ma, J. Guo, J. Hu, C.C. Wang, Silver-coated magnetite-carbon core-shell microspheres as substrate-enhanced SERS probes for detection of trace persistent organic pollutants, Nanoscale 4 (2012) 5210−5216, https://doi.org/10.1039/c2nr31061a.
[310] Z.Y. Bao, X. Liu, Y. Chen, Y. Wu, H.L.W. Chan, J. Dai, D.Y. Lei, Quantitative SERS detection of low-concentration aromatic polychlorinated biphenyl-77 and 2,4,6-trinitrotoluene, J. Hazard Mater. 280 (2014) 706−712, https://doi.org/10.1016/j.jhazmat.2014.08.058.
[311] W. Cai, X. Tang, B. Sun, L. Yang, Highly sensitive in situ monitoring of catalytic reactions by surface enhancement Raman spectroscopy on multifunctional Fe_3O_4/C/Au NPs, Nanoscale 6 (2014) 7954−7958, https://doi.org/10.1039/c4nr01147c.
[312] S. Qin, W. Cai, X. Tang, L. Yang, Sensitively monitoring photodegradation process of organic dye molecules by surface-enhanced Raman spectroscopy based on Fe_3O_4@SiO_2@TiO_2@Ag particle, Analyst 139 (2014) 5509−5515, https://doi.org/10.1039/c4an01084a.
[313] Z. Li, S. Ji, Y. Liu, X. Cao, S. Tian, Y. Chen, Z. Niu, Y. Li, Well-defined materials for heterogeneous catalysis: from nanoparticles to isolated single-atom sites, Chem. Rev. 120 (2020) 623−682, https://doi.org/10.1021/acs.chemrev.9b00311.
[314] Erlantz Lizundia, Marta Jimenez, Christian Altorfer, Markus Niederberger, Walter Caseri, Electroless plating of platinum nanoparticles onto mesoporous cellulose films for catalytically active free-standing materials, Cellulose 26 (2019) 5513−5527.
[315] A. Akbari, M. Amini, A. Tarassoli, B. Eftekhari-Sis, N. Ghasemian, E. Jabbari, Transition metal oxide nanoparticles as efficient catalysts in oxidation

reactions, Nano-Struct. Nano-Objects 14 (2018) 19–48, https://doi.org/10.1016/j.nanoso.2018.01.006.
[316] V.B. Saptal, B.M. Bhanage, Current advances in heterogeneous catalysts for the synthesis of cyclic carbonates from carbon dioxide, Curr. Opin. Green Sustain. Chem. 3 (2017) 1–10, https://doi.org/10.1016/j.cogsc.2016.10.006.
[317] S. Sultana, S. Bordoloi, S. Konwer, G. Borah, P.K. Gogoi, Reduced graphene oxide/iron oxide hybrid composite material as an efficient magnetically separable heterogeneous catalyst for transfer hydrogenation of ketones, Appl. Organomet. Chem. 34 (2020), e5582, https://doi.org/10.1002/aoc.5582.
[318] X. Duan, J. Liu, J. Hao, L. Wu, B. He, Y. Qiu, J. Zhang, Z. He, J. Xi, S. Wang, Magnetically recyclable nanocatalyst with synergetic catalytic effect and its application for 4-nitrophenol reduction and Suzuki coupling reactions, Carbon 130 (2018) 806–813, https://doi.org/10.1016/j.carbon.2018.01.038.
[319] M.R. Nabid, Y. Bide, E. Aghaghafari, S.J.T. Rezaei, PdNPs@P2VP-Fe_3O_4 organic–inorganic hybrid microgels as a nanoreactor for selective aerobic oxidation of alcohols, Catal. Lett. 144 (2014) 355–363, https://doi.org/10.1007/s10562-013-1107-2.
[320] B. Karimi, S. Abedi, J.H. Clark, V. Budarin, Highly efficient aerobic oxidation of alcohols using a recoverable catalyst: the role of mesoporous channels of SBA-15 in stabilizing palladium nanoparticles, Angew. Chem. Int. Ed. 45 (2006) 4776–4779, https://doi.org/10.1002/anie.200504359.
[321] T. Baran, M. Nasrollahzadeh, Facile synthesis of palladium nanoparticles immobilized on magnetic biodegradable microcapsules used as effective and recyclable catalyst in Suzuki-Miyaura reaction and p-nitrophenol reduction, Carbohydr. Polym. 222 (2019), 115029, https://doi.org/10.1016/j.carbpol.2019.115029.
[322] H. Woo, J.C. Park, S. Park, K.H. Park, Rose-like Pd–Fe_3O_4 hybrid nanocomposite-supported Au nanocatalysts for tandem synthesis of 2-phenylindoles, Nanoscale 7 (2015) 8356–8360, https://doi.org/10.1039/C5NR01441G.
[323] B. Suresh Kumar, A.J. Amali, K. Pitchumani, Fabrication of Pd nanoparticles embedded C@Fe_3O_4 core–shell hybrid nanospheres: an efficient catalyst for cyanation in aryl halides, ACS Appl. Mater. Interfaces 7 (2015) 22907–22917, https://doi.org/10.1021/acsami.5b08875.
[324] L. Qu, Y. Liu, J.-B. Baek, L. Dai, Nitrogen-doped graphene as efficient metal-free electrocatalyst for oxygen reduction in fuel cells, ACS Nano 4 (2010) 1321–1326, https://doi.org/10.1021/nn901850u.
[325] E. Doustkhah, S. Rostamnia, Covalently bonded sulfonic acid magnetic graphene oxide: Fe_3O_4@GO-Pr-SO_3H as a powerful hybrid catalyst for synthesis of indazolophthalazinetriones, J. Colloid Interface Sci. 478 (2016) 280–287, https://doi.org/10.1016/j.jcis.2016.06.020.
[326] S. Wu, Q. He, C. Zhou, X. Qi, X. Huang, Z. Yin, Y. Yang, H. Zhang, Synthesis of Fe_3O_4 and Pt nanoparticles on reduced graphene oxide and their use as a recyclable catalyst, Nanoscale 4 (2012) 2478–2483, https://doi.org/10.1039/C2NR11992G.
[327] M.R. Nabid, Y. Bide, M. Niknezhad, Fe_3O_4–SiO_2–P4VP pH-sensitive microgel for immobilization of nickel nanoparticles: an efficient heterogeneous catalyst for nitrile reduction in water, ChemCatChem 6 (2014) 538–546, https://doi.org/10.1002/cctc.201300984.
[328] R. Tayebee, M.M. Amini, H. Rostamian, A. Aliakbari, Preparation and characterization of a novel Wells–Dawson heteropolyacid-based magnetic inorganic–organic nanohybrid catalyst $H_6P_2W_{18}O_{62}$/pyridino-Fe_3O_4 for the efficient synthesis of 1-amidoalkyl-2-naphthols under solvent-free conditions, Dalt. Trans. 43 (2014) 1550–1563, https://doi.org/10.1039/C3DT51594J.
[329] A. Farrokhi, K. Ghodrati, I. Yavari, Fe_3O_4/SiO_2/$(CH_2)_3N$+Me_3Br_3–core–shell nanoparticles: a novel catalyst for the solvent-free synthesis of five- and six-membered heterocycles, Catal. Commun. 63 (2015) 41–46, https://doi.org/10.1016/j.catcom.2014.09.046.
[330] K. Mishra, N. Basavegowda, Y.R. Lee, AuFeAg hybrid nanoparticles as an efficient recyclable catalyst for the synthesis of α,β- and β,β-dichloroenones, Appl. Catal. Gen. 506 (2015) 180–187, https://doi.org/10.1016/j.apcata.2015.09.014.
[331] C.J. Collins, G.B. Fisher, A. Reem, C.T. Goralski, B. Singaram, Selective reductions of aldehydes, ketones, esters, and epoxides in the presence of a nitrile using Lithium N,N-dialkylaminoborohydrides, Tetrahedron Lett. 38 (1997) 529–532, https://doi.org/10.1016/S0040-4039(96)02410-0.
[332] R.K. Sharma, R. Gaur, M. Yadav, A. Goswami, R. Zbořil, M.B. Gawande, An efficient copper-based magnetic nanocatalyst for the fixation of carbon dioxide at atmospheric pressure, Sci. Rep. 8 (2018) 1901, https://doi.org/10.1038/s41598-018-19551-3.
[333] W. Xie, F. Wan, Basic ionic liquid functionalized magnetically responsive Fe_3O_4@HKUST-1 composites used for biodiesel production, Fuel 220 (2018) 248–256, https://doi.org/10.1016/j.fuel.2018.02.014.
[334] R. Dalpozzo, Magnetic nanoparticle supports for asymmetric catalysts, Green Chem. 17 (2015) 3671–3686, https://doi.org/10.1039/C5GC00386E.
[335] R. Mrówczyński, A. Nan, J. Liebscher, Magnetic nanoparticle-supported organocatalysts – an efficient way of recycling and reuse, RSC Adv. 4 (2014) 5927–5952, https://doi.org/10.1039/C3RA46984K.
[336] W. Xie, X. Zang, Covalent immobilization of lipase onto aminopropyl-functionalized hydroxyapatite-encapsulated-γ-Fe_2O_3 nanoparticles: a magnetic biocatalyst for interesterification of soybean oil, Food Chem. 227 (2017) 397–403, https://doi.org/10.1016/j.foodchem.2017.01.082.
[337] F.M. Windsor, M.G. Pereira, C.R. Tyler, S.J. Ormerod, River organisms as indicators of the distribution and sources of persistent organic pollutants in contrasting catchments, Environ. Pollut. 255 (2019), 113144, https://doi.org/10.1016/j.envpol.2019.113144.
[338] Y. Tang, M. Yin, W. Yang, H. Li, Y. Zhong, L. Mo, Y. Liang, X. Ma, X. Sun, Emerging pollutants in water environment: occurrence, monitoring, fate, and risk assessment, Water Environ. Res. 91 (2019) 984–991, https://doi.org/10.1002/wer.1163.
[339] M. Huerta-Fontela, M.T. Galceran, F. Ventura, Occurrence and removal of pharmaceuticals and hormones through drinking water treatment, Water Res. 45 (2011) 1432–1442, https://doi.org/10.1016/j.watres.2010.10.036.
[340] L. Song, C. Huang, W. Zhang, M. Ma, Z. Chen, N. Gu, Y. Zhang, Graphene oxide-based Fe_2O_3 hybrid enzyme mimetic with enhanced peroxidase and catalase-like activities, Colloid Surf. A Physicochem. Eng. Asp. 506 (2016) 747–755, https://doi.org/10.1016/j.colsurfa.2016.07.037.
[341] D.P. Cormode, L. Gao, H. Koo, Emerging biomedical applications of enzyme-like catalytic nanomaterials, Trends Biotechnol. 36 (2018) 15–29, https://doi.org/10.1016/j.tibtech.2017.09.006.
[342] L. Bai, W. Jiang, M. Sang, M. Liu, S. Xuan, S. Wang, K.C.-F. Leung, X. Gong, Magnetic microspheres with polydopamine encapsulated ultra-small noble metal nanocrystals as mimetic enzymes for the colorimetric detection of H_2O_2 and glucose, J. Mater. Chem. B. 7 (2019) 4568–4580, https://doi.org/10.1039/C9TB00755E.
[343] D. Kwon, S. Lee, M.M. Ahn, I.S. Kang, K.-H. Park, S. Jeon, Colorimetric detection of pathogenic bacteria using platinum-coated magnetic nanoparticle clusters and magnetophoretic chromatography, Anal. Chim. Acta 883 (2015) 61–66, https://doi.org/10.1016/j.aca.2015.04.044.
[344] Z. Yang, Y. Zhu, M. Chi, C. Wang, Y. Wei, X. Lu, Fabrication of cobalt ferrite/cobalt sulfide hybrid nanotubes with enhanced peroxidase-like activity for colorimetric detection of dopamine, J. Colloid Interface Sci. 511 (2018) 383–391, https://doi.org/10.1016/j.jcis.2017.09.097.
[345] X. Ma, S. Wen, X. Xue, Y. Guo, J. Jin, W. Song, B. Zhao, Controllable synthesis of SERS-active magnetic metal–organic framework-based nanocatalysts and their application in photoinduced enhanced catalytic oxidation, ACS Appl. Mater. Interfaces 10 (2018) 25726–25736, https://doi.org/10.1021/acsami.8b03457.
[346] J.W. Lee, H.J. Jeon, H.-J. Shin, J.K. Kang, Superparamagnetic Fe_3O_4 nanoparticles–carbon nitride nanotube hybrids for highly efficient peroxidase mimetic catalysts, Chem. Commun. 48 (2012) 422–424, https://doi.org/10.1039/C1CC15725F.
[347] R. Tabit, O. Amadine, Y. Essamlali, K. Dânoun, A. Rhihil, M. Zahouily, Magnetic $CoFe_2O_4$ nanoparticles supported on graphene oxide ($CoFe_2O_4$/GO) with high catalytic activity for peroxymonosulfate activation and degradation of rhodamine B, RSC Adv. 8 (2018) 1351–1360, https://doi.org/10.1039/C7RA09949E.
[348] Y. Tian, Y. Liu, F. Pang, F. Wang, X. Zhang, Green synthesis of nanostructed Ni-reduced graphene oxide hybrids and their application for catalytic reduction of 4-nitrophenol, Colloid Surf. A Physicochem. Eng. Asp. 464 (2015) 96–103, https://doi.org/10.1016/j.colsurfa.2014.10.027.
[349] W. Gu, X. Deng, X. Jia, J. Li, E. Wang, Functionalized graphene/Fe_3O_4 supported AuPt alloy as a magnetic, stable and recyclable catalyst for a catalytic reduction reaction, J. Mater. Chem. A 3 (2015) 8793–8799, https://doi.org/10.1039/C5TA01099C.
[350] L. Liu, R. Chen, W. Liu, J. Wu, D. Gao, Catalytic reduction of 4-nitrophenol over Ni-Pd nanodimers supported on nitrogen-doped reduced graphene oxide, J. Hazard Mater. 320 (2016) 96–104, https://doi.org/10.1016/j.jhazmat.2016.08.019.
[351] J. Tang, J. Wang, Fenton-like degradation of sulfamethoxazole using Fe-based magnetic nanoparticles embedded into mesoporous carbon hybrid as an efficient catalyst, Chem. Eng. J. 351 (2018) 1085–1094, https://doi.org/10.1016/j.cej.2018.06.169.
[352] R.S. Ribeiro, A.M.T. Silva, P.B. Tavares, J.L. Figueiredo, J.L. Faria, H.T. Gomes, Hybrid magnetic graphitic nanocomposites for catalytic wet peroxide oxidation applications, Catal. Today 280 (2017) 184–191, https://doi.org/10.1016/j.cattod.2016.04.040.
[353] X. Yu, G. Cheng, S.-Y. Zheng, Synthesis of self-assembled multifunctional nanocomposite catalysts with highly stabilized reactivity and magnetic recyclability, Sci. Rep. 6 (2016), 25459, https://doi.org/10.1038/srep25459.
[354] X. Tian, W. Wang, N. Tian, C. Zhou, C. Yang, S. Komarneni, Cr(VI) reduction and immobilization by novel carbonaceous modified magnetic Fe_3O_4/halloysite nanohybrid, J. Hazard Mater. 309 (2016) 151–156, https://doi.org/10.1016/j.jhazmat.2016.01.081.
[355] T. Tsoufis, F. Katsaros, B.J. Kooi, E. Bletsa, S. Papageorgiou, Y. Deligiannakis, I. Panagiotopoulos, Halloysite nanotube-magnetic iron oxide nanoparticle hybrids for the rapid catalytic decomposition of pentachlorophenol, Chem. Eng. J. 313 (2017) 466–474, https://doi.org/10.1016/j.cej.2016.12.056.
[356] M. Sillanpää, M.C. Ncibi, A. Matilainen, Advanced oxidation processes for the removal of natural organic matter from drinking water sources: a comprehensive review, J. Environ. Manag. 208 (2018) 56–76, https://doi.org/10.1016/j.jenvman.2017.12.009.
[357] C.H. Neoh, Z.Z. Noor, N.S.A. Mutamim, C.K. Lim, Green technology in wastewater treatment technologies: integration of membrane bioreactor with various wastewater treatment systems, Chem. Eng. J. 283 (2016) 582–594, https://doi.org/10.1016/j.cej.2015.07.060.

[358] M.N. Chong, B. Jin, C.W.K. Chow, C. Saint, Recent developments in photocatalytic water treatment technology: a review, Water Res. 44 (2010) 2997–3027, https://doi.org/10.1016/j.watres.2010.02.039.
[359] R. Zouzelka, Y. Kusumawati, M. Remzova, J. Rathousky, T. Pauporté, Photocatalytic activity of porous multiwalled carbon nanotube-TiO_2 composite layers for pollutant degradation, J. Hazard Mater. 317 (2016) 52–59, https://doi.org/10.1016/j.jhazmat.2016.05.056.
[360] A. Bonnefond, M. Ibarra, E. Gonzalez, M. Barrado, A. Chuvilin, J. Maria Asua, J. Ramon Leiza, Photocatalytic and magnetic titanium dioxide/polystyrene/magnetite composite hybrid polymer particles, J. Polym. Sci. Part A Polym. Chem. 54 (2016) 3350–3356, https://doi.org/10.1002/pola.28224.
[361] Y. Chen, D. Zeng, M.B. Cortie, A. Dowd, H. Guo, J. Wang, D.-L. Peng, Seed-induced growth of flower-like Au–Ni–ZnO metal–semiconductor hybrid nanocrystals for photocatalytic applications, Small 11 (2015) 1460–1469, https://doi.org/10.1002/smll.201401853.
[362] L. Ciccotti, L.A.S. do Vale, T.L.R. Hewer, R.S. Freire, Fe_3O_4@TiO_2 preparation and catalytic activity in heterogeneous photocatalytic and ozonation processes, Catal. Sci. Technol. 5 (2015) 1143–1152, https://doi.org/10.1039/C4CY01242A.
[363] Johan Emelian Moan, Visible Light and UV Radiation, Part 1: Fundamentals – Non-ionizing Radiation, 2004.
[364] W.J. Chung, D.D. Nguyen, X.T. Bui, S.W. An, J.R. Banu, S.M. Lee, S.S. Kim, D.H. Moon, B.H. Jeon, S.W. Chang, A magnetically separable and recyclable Ag-supported magnetic TiO_2 composite catalyst: fabrication, characterization, and photocatalytic activity, J. Environ. Manag. 213 (2018) 541–548, https://doi.org/10.1016/j.jenvman.2018.02.064.
[365] S. Alberti, V. Caratto, D. Peddis, C. Belviso, M. Ferretti, Synthesis and characterization of a new photocatalyst based on TiO_2 nanoparticles supported on a magnetic zeolite obtained from iron and steel industrial waste, J. Alloys Compd. 797 (2019) 820–825, https://doi.org/10.1016/j.jallcom.2019.05.098.
[366] T. Parandhaman, N. Pentela, B. Ramalingam, D. Samanta, S.K. Das, Metal nanoparticle loaded magnetic-chitosan microsphere: water dispersible and easily separable hybrid metal nano-biomaterial for catalytic applications, ACS Sustain. Chem. Eng. 5 (2017) 489–501, https://doi.org/10.1021/acssuschemeng.6b01862.
[367] D. Xia, I.M.C. Lo, Synthesis of magnetically separable Bi_2O_4/Fe_3O_4 hybrid nanocomposites with enhanced photocatalytic removal of ibuprofen under visible light irradiation, Water Res. 100 (2016) 393–404, https://doi.org/10.1016/j.watres.2016.05.026.
[368] Y. Yao, Y. Cai, F. Lu, J. Qin, F. Wei, C. Xu, S. Wang, Magnetic $ZnFe_2O_4$–C_3N_4 hybrid for photocatalytic degradation of aqueous organic pollutants by visible light, Ind. Eng. Chem. Res. 53 (2014) 17294–17302, https://doi.org/10.1021/ie503437z.
[369] N. Klamerth, S. Malato, A. Agüera, A. Fernández-Alba, G. Mailhot, Treatment of municipal wastewatert treatment plant effluents with modified photo-Fenton as a tertiary treatment for the degradation of micro pollutants and disinfection, Environ. Sci. Technol. 46 (2012) 2885–2892, https://doi.org/10.1021/es204112d.
[370] Y. Yao, J. Qin, Y. Cai, F. Wei, F. Lu, S. Wang, Facile synthesis of magnetic $ZnFe_2O_4$–reduced graphene oxide hybrid and its photo-Fenton-like behavior under visible iradiation, Environ. Sci. Pollut. Res. 21 (2014) 7296–7306, https://doi.org/10.1007/s11356-014-2645-x.
[371] Y. Yao, Y. Cai, F. Lu, F. Wei, X. Wang, S. Wang, Magnetic recoverable $MnFe_2O_4$ and $MnFe_2O_4$-graphene hybrid as heterogeneous catalysts of peroxymonosulfate activation for efficient degradation of aqueous organic pollutants, J. Hazard Mater. 270 (2014) 61–70, https://doi.org/10.1016/j.jhazmat.2014.01.027.
[372] H.-Y. He, J. Lu, Highly photocatalytic activities of magnetically separable reduced graphene oxide-CoFe2O4 hybrid nanostructures in dye photodegradation, Separ. Purif. Technol. 172 (2017) 374–381, https://doi.org/10.1016/j.seppur.2016.08.040.
[373] E. Lizundia, M. Rincón-Iglesias, S. Lanceros-Méndez, Combining cobalt ferrite and graphite with cellulose nanocrystals for magnetically active and electrically conducting mesoporous nanohybrids, Carbohydr. Polym. 236 (2020), 116001, https://doi.org/10.1016/j.carbpol.2020.116001.
[374] J. Jeevanandam, A. Barhoum, Y.S. Chan, A. Dufresne, M.K. Danquah, Review on nanoparticles and nanostructured materials: history, sources, toxicity and regulations, Beilstein J. Nanotechnol. 9 (2018) 1050–1074.
[375] C. Liao, Y. Li, C.S. Tjong, Bactericidal and cytotoxic properties of silver nanoparticles, Int. J. Mol. Sci. 20 (2019) 449, https://doi.org/10.3390/ijms20020449.
[376] S.C.N. Tang, I.M.C. Lo, Magnetic nanoparticles: essential factors for sustainable environmental applications, Water Res. 47 (2013) 2613–2632, https://doi.org/10.1016/j.watres.2013.02.039.
[377] 2050 Long-Term Strategy. European Commission. Available at: https://ec.europa.eu/clima/policies/strategies/2050_en (accessed on September 2022).
[378] I. Rey, C. Vallejo, G. Santiago, M. Iturrondobeitia, E. Lizundia, Environmental impacts of graphite recycling from spent lithium-ion batteries based on life cycle assessment, ACS Sustain. Chem. Eng. 9 (2021) 14488–14501, https://doi.org/10.1021/acssuschemeng.1c04938.
[379] C. Alejandre, O. Akizu-Gardoki, E. Lizundia, Optimum operational lifespan of household appliances considering manufacturing and use stage improvements via life cycle assessment, Sustain. Prod. Consum. 32 (2022) 52–65, https://doi.org/10.1016/j.spc.2022.04.007.
[380] R.L. de Lapuente Díaz de Otazu, O. Akizu-Gardoki, B. de Ulibarri, M. Iturriondobeitia, R. Minguez, E. Lizundia, Ecodesign coupled with Life Cycle Assessment to reduce the environmental impacts of an industrial enzymatic cleaner, Sustain. Prod. Consum. 29 (2021) 718–729, https://doi.org/10.1016/j.spc.2021.11.016.
[381] S. Feijoo, S. González-García, Y. Moldes-Diz, C. Vazquez-Vazquez, G. Feijoo, M.T. Moreira, Comparative life cycle assessment of different synthesis routes of magnetic nanoparticles, J. Clean. Prod. 143 (2017) 528–538, https://doi.org/10.1016/j.jclepro.2016.12.079.
[382] J.S. Arteaga-Díaz, I.S. Meramo-Hurtado, J. León-Pulido, A. Zuorro, D.A. González-Delgado, Environmental assessment of large scale production of magnetite (Fe_3O_4) nanoparticles via coprecipitation, Appl. Sci. 9 (2019) 1682, https://doi.org/10.3390/app9081682.
[383] W. Marimón-Bolívar, E.E. González, Green synthesis with enhanced magnetization and life cycle assessment of Fe_3O_4 nanoparticles, Environ. Nanotechnol. Monit. Manag. 9 (2018) 58–66, https://doi.org/10.1016/j.enmm.2017.12.003.
[384] C. Baresel, V. Schaller, C. Jonasson, C. Johansson, R. Bordes, V. Chauhan, A. Sugunan, J. Sommertune, S. Welling, Functionalized magnetic particles for water treatment, Heliyon 5 (2019), e02325, https://doi.org/10.1016/j.heliyon.2019.e02325.
[385] P. Weyell, H.-D. Kurland, T. Hülser, J. Grabow, F.A. Müller, D. Kralisch, Risk and life cycle assessment of nanoparticles for medical applications prepared using safe- and benign-by-design gas-phase syntheses, Green Chem. 22 (2020) 814–827, https://doi.org/10.1039/C9GC02436K.
[386] S. Feijoo, J. González-Rodríguez, L. Fernández, C. Vázquez-Vázquez, G. Feijoo, T.M. Moreira, Fenton and photo-Fenton nanocatalysts revisited from the perspective of life cycle assessment, Catalysts 10 (2019) 23, https://doi.org/10.3390/catal10010023.
[387] G. Celik, R.M. Kennedy, R.A. Hackler, M. Ferrandon, A. Tennakoon, S. Patnaik, A.M. LaPointe, S.C. Ammal, A. Heyden, F.A. Perras, M. Pruski, S.L. Scott, K.R. Poeppelmeier, A.D. Sadow, M. Delferro, Upcycling single-use polyethylene into high-quality liquid products, ACS Cent. Sci. 5 (2019) 1795–1803, https://doi.org/10.1021/acscentsci.9b00722.
[388] A. Lauria, E. Lizundia, Luminescent carbon dots obtained from polymeric waste, J. Clean. Prod. (2020), 121288, https://doi.org/10.1016/j.jclepro.2020.121288.
[389] R.G. Saratale, I. Karuppusamy, G.D. Saratale, A. Pugazhendhi, G. Kumar, Y. Park, G.S. Ghodake, R.N. Bharagava, J.R. Banu, H.S. Shin, A comprehensive review on green nanomaterials using biological systems: recent perception and their future applications, Colloids Surf. B Biointerfaces 170 (2018) 20–35, https://doi.org/10.1016/j.colsurfb.2018.05.045.
[390] N. Joshi, J. Filip, V.S. Coker, J. Sadhukhan, I. Safarik, H. Bagshaw, J.R. Lloyd, Microbial reduction of natural Fe(III) minerals; toward the sustainable production of functional magnetic nanoparticles, Front. Environ. Sci. 6 (2018) 127, https://doi.org/10.3389/fenvs.2018.00127.
[391] B. Fabiano, A.P. Reverberi, P.S. Varbanov, Safety opportunities for the synthesis of metal nanoparticles and short-cut approach to workplace risk evaluation, J. Clean. Prod. 209 (2019) 297–308, https://doi.org/10.1016/j.jclepro.2018.10.161.
[392] L. Pokrajac, A. Abbas, W. Chrzanowski, G.M. Dias, B.J. Eggleton, S. Maguire, E. Maine, T. Malloy, J. Nathwani, L. Nazar, A. Sips, J. Sone, A. van den Berg, P.S. Weiss, S. Mitra, Nanotechnology for a sustainable future: addressing global challenges with the international Network4Sustainable nanotechnology, ACS Nano 15 (2021) 18608–18623, https://doi.org/10.1021/acsnano.1c10919.
[393] S. Ge, M. Agbakpe, W. Zhang, L. Kuang, Z. Wu, X. Wang, Recovering magnetic Fe_3O_4–ZnO nanocomposites from algal biomass based on hydrophobicity shift under UV irradiation, ACS Appl. Mater. Interfaces 7 (2015) 11677–11682, https://doi.org/10.1021/acsami.5b03472.
[394] R. Katakojwala, S.V. Mohan, Microcrystalline cellulose production from sugarcane bagasse: sustainable process development and life cycle assessment, J. Clean. Prod. 249 (2020), 119342, https://doi.org/10.1016/j.jclepro.2019.119342.
[395] C.D. Powell, A.J. Atkinson, Y. Ma, M. Marcos-Hernandez, D. Villagran, P. Westerhoff, M.S. Wong, Magnetic nanoparticle recovery device (MagNERD) enables application of iron oxide nanoparticles for water treatment, J. Nanoparticle Res. 22 (2020) 48, https://doi.org/10.1007/s11051-020-4770-4.
[396] A. Fontana, A. Barni, D. Leone, M. Spirito, A. Tringale, M. Ferraris, J. Reis, G. Goncalves, Circular economy strategies for equipment lifetime extension: a systematic review, Sustainability 13 (2021) 1117, https://doi.org/10.3390/su13031117.

[397] L. Nana, L. Ruiyi, W. Qinsheng, Y. Yongqiang, S. Xiulan, W. Guangli, L. Zaijun, Colorimetric detection of chlorpyrifos in peach based on cobalt-graphene nanohybrid with excellent oxidase-like activity and reusability, J. Hazard Mater. 415 (2021), 125752, https://doi.org/10.1016/j.jhazmat.2021.125752.
[398] S.B. Santosh, Emerging sustainable nanomaterials and their applications in catalysis and corrosion control, Curr. Nanosci. 17 (2021), https://doi.org/10.2174/1573413716999200917121311.
[399] G. Sang, C. Wang, Y. Zhao, G. He, Q. Zhang, M. Yang, S. Zhao, P. Xu, X. Xi, J. Yang, Ni@CNTs/Al_2O_3 ceramic composites with interfacial solder strengthen the segregated network for high toughness and excellent electromagnetic interference shielding, ACS Appl. Mater. Interfaces 14 (2022) 4443−4455, https://doi.org/10.1021/acsami.1c21630.
[400] P. Anastas, N. Eghbali, Green chemistry: principles and practice, Chem. Soc. Rev. 39 (2010) 301−312, https://doi.org/10.1039/B918763B.
[401] G. Moraga, S. Huysveld, S. De Meester, J. Dewulf, Resource efficiency indicators to assess circular economy strategies: a case study on four materials in laptops, Resour. Conserv. Recycl. 178 (2022), 106099, https://doi.org/10.1016/j.resconrec.2021.106099.